12-2014

ROBUST DESIGN OF SHIELD TUNNELS - CONSIDERING THE LONGITUDINAL VARIATION OF INPUT PARAMETERS

Wenping Gong
Clemson University, tumugwp2007@gmail.com

ROBUST DESIGN OF SHIELD TUNNELS – CONSIDERING THE LONGITUDINAL VARIATION OF INPUT PARAMETERS

A Dissertation
Presented to
the Graduate School of
Clemson University

In Partial Fulfillment
of the Requirements for the Degree
Doctor of Philosophy
Civil Engineering

---

by
Wenping Gong
December 2014

Accepted by:
Dr. C. Hsein Juang, Committee Chair
Dr. Sez Atamturktur, Co-Chair
Dr. Yongxi Huang
Dr. Qiushi Chen

ABSTRACT

This dissertation, aimed at developing an improved design methodology for shield tunnels that explicitly considers design robustness against longitudinal variation of input parameters (such as soil parameters). To this end, a new solution model for shield tunnel performance analysis was first developed. In this new model, the random field concept was employed to model the longitudinal variation of input parameters. The input parameters (in the longitudinal domain) that had been generated with Monte Carlo simulation (MCS) were used as inputs for the tunnel longitudinal behavior analysis. Here, the finite element method (FEM) based upon Winkler elastic foundation theory was employed. The analyzed tunnel longitudinal responses as well as the input parameters that had been generated with MCS were then used to study the performance (i.e., structure safety and serviceability) of tunnel segment rings. For the latter analysis, the force method was used. Finally, the robust design concept was integrated into the design of shield tunnels to guard against variation of tunnel performance caused by longitudinal variation of input parameters. Within the framework of robust design, a multi-objective optimization was performed aiming to optimize the design with respect to design robustness against longitudinal variation of input parameters and cost efficiency, while satisfying safety and serviceability requirements. Through illustrative examples, the effectiveness and significance of improved shield tunnel design methodology was demonstrated.

DEDICATION

I dedicate this dissertation to my parents for their love and support all these years.

ACKNOWLEDGMENTS

I would first like to express my sincere gratitude to my advisors, Dr. C. Hsein Juang and Dr. Sez Atamturktur, for their invaluable advices, supports and encouragements. Without their guidance and persistent advices, this dissertation would not have been possible. I would also like to thank my committee members, Dr. Yongxi Huang and Dr. Qiushi Chen for their advices and support during the course of this dissertation study. I would also like to express my sincere appreciation to Dr. James R. Martin, Dr. Ronald Andrus, Dr. Nadarajah Ravichandran, Dr. Bryant G. Nielson, Dr. Melissa Sternhagen, Dr. Zhe Luo, and Dr. Marcin Ziolkowski for their assistance and support during my PhD study at Clemson. I would also like to express my sincere appreciation to Dr. Hongwei Huang, Dr. Dongmei Zhang, Dr. Jie Zhang, and Dr. Yadong Xue for their advices during my study at Tongji.

I am grateful to my fellow co-workers and graduate students at Clemson, Zhifeng Liu, Lei Wang, Sara Khoshnevisan, Andrew Brownlow, Menfeng Shen, Kaifu Liu, Chunxia Huang, Shenghua Qiu, Junhua Xiao,Chaofeng Wang, Xiaoyu Hu, Ariful Haque, Mahi Mahinthakumar N, Parish Shad, Xinyu Lu, Li Wang, and Yuheng Du for engaging discussion and friendship. I would like to thank my parents. They always understand and support me with a lot of patience. They are the power of my study.

This study has been supported in part by the National Science Foundation through Grant CMMI-1200117 and the Glenn Department of Civil Engineering, Clemson University. The results and opinions expressed in this dissertation do not necessarily reflect the views and policies of the National Science Foundation. Finally, I would like to

thank the Shrikhande family and the Glenn Department of Civil Engineering for awarding me the Aniket Shrikhande Memorial Annual Graduate Fellowship.

TABLE OF CONTENTS

Page

Table of Contents (Continued)

Page

LIST OF TABLES

LIST OF FIGURES

List of Figures (Continued)

Figure Page

List of Figures (Continued)

Figure Page

List of Figures (Continued)

Figure Page

List of Figures (Continued)

Figure Page

CHAPTER ONE

INTRODUCTION

Motivation and Background

Since the first shield tunnel was constructed in London 170 years ago, shield tunneling has gained increasing popularity for its flexibility, cost efficiency and minimal impact on ground traffic and surface structures (Lee et al. 2001). Today, shield tunneling method has become one of the most popular methods used in construction of urban tunnels, particularly for tunnels in soft soils. While significant progress has been achieved in shield-driven machines and tunneling technologies, the design of the segment lining of these shield tunnels, which are constructed with shield-driven machines, is still based upon the analysis of only a few cross sections with the assumption of a plane strain condition (Wood 1975; ITA 2000; Bobet 2001; Lee et al. 2001; Lee and Ge 2001; Koyama 2003).

In general, the longitudinal length of a shield tunnel may be in thousands of meters while the diameter may be less than 10 m; as such, the design of a shield tunnel should be a 3-D problem instead of a 2-D plane strain problem. Additionally, the longitudinal variation of input parameters (e.g., soil parameters, ground water table and overburden) may be of higher consequence than expected. The longitudinal variation of input parameters can be attributed to factors such as variation of tunnel alignment, spatial variation of soil parameters, and nearby tunneling activities. Note that the determination of typical tunnel cross sections could be a significant challenge in a situation where

variations of input parameters are not negligible. Indeed, it has long been acknowledged that the longitudinal variation of input parameters should be considered in the analysis and design of shield tunnels (ATRB 2000; ITA 2000; Koyama 2003); nevertheless, a rational solution for shield tunnel performance analysis that can consider the longitudinal variation of input parameters could not yet be found.

It is noted that the longitudinal behavior of a shield tunnel (caused by the longitudinal variation of input parameters) and its influence on the circumferential performance of the segment lining (referred to herein as the structure safety and serviceability of tunnel segment ring) may be investigated with numerical models implemented in softwares such as ABAQUS, ANSYS, and PLAXIS. However, the analysis and design of a shield tunnel based upon such numerical analysis is often computationally prohibitive in practice. A more feasible approach to analyze longitudinal behavior is to model the tunnel as a continuous elastic beam (Shiwa et al. 1986; Talmon and Bezuijen 2013). In this context, the effect of the longitudinal joints (referred to herein as the joints between segment rings) on the flexural stiffness of tunnel longitudinal structure is simulated with a reduction factor of tunnel longitudinal flexural stiffness (Liao et al. 2008); and the soil-structure interaction between the tunnel structure and ground directly below the tunnel may be simulated with Winkler model (Winkler 1867), Pasternak model (Pasternak 1954), or Kerr model (Kerr 1965), while the overburden of the tunnel is represented with a pressure load and/or concentrated loads. The analytical solution of tunnel longitudinal behavior is readily derived based upon these assumptions. Furthermore, the effect of tunnel longitudinal behavior on the circumferential

performance of the segment lining can be analyzed by a simultaneous consideration of the shearing effect (Liao et al. 2008) and the flattening effect (Huang et al. 2012). It is expected that the longitudinal variation of input parameters could complicate the performance analysis of shield tunnels regardless of whether the numerical methods or analytical solutions are adopted).

In the conventional deterministic design of tunnel segment lining, a conservative estimate of input parameters, which are required for the performance analysis of tunnel cross sections, is often taken to compensate for the inevitable longitudinal variation. To further ensure safety, the computed factor of safety for a feasible design is required to be greater than a target factor of safety, a value derived from past experience. Thus, the "true" safety level of the resulting design of shield tunnels is generally unknown, as the uncertainties of input parameters are not explicitly considered. To overcome the shortcomings of the deterministic design approach, probabilistic approaches that consider uncertainties explicitly have been sought (Mollon 2009; Li and Low 2010; Lü and Low 2011; Špačková 2013). Within which, the input parameters associated with longitudinal variation are dealt with as random variables and the outcome of the analysis of tunnel cross sections of concern is generally expressed as a reliability index or a probability of failure. However, in the practice of geotechnical engineering, site-specific data is often limited, thus an accurate statistical characterization of these uncertain variables is indeed a challenging prerequisite. The results of a probabilistic analysis might be greatly undermined if the adopted joint distribution of input parameters could not be reliably determined. Recently, robust geotechnical design (RGD) methodology has been

developed for analysis and design of geotechnical systems with uncertain input parameters (Juang et al. 2013 & 2014; Wang et al. 2013; Gong et al. 2014b & 2014c).

In the context of robust design, a design is considered robust if the performance of the system is robust against, or insensitive to, the variation of uncertain input parameters. Within the RGD framework, design robustness is sought along with safety and cost efficiency. Cost is primarily a function of design parameters, including those that are "easy-to-control" by the designer, such as the geometry and dimensions. Safety and robustness are, however, a function of the design parameters as well as the "hard-to-control" parameters, such as uncertain soil parameters. Here, these hard-to-control input parameters are termed "noise factors." The primary goal of RGD is to derive an optimal design (represented by a set of design parameters), in which the system response is robust against, or insensitive to, the variation of noise factors while the requirements of safety and cost efficiency are satisfied. The RGD provides a new perspective for designing geotechnical systems under an uncertain environment.

In this dissertation, a new solution model for shield tunnel performance analysis is proposed which incorporates the longitudinal variation of input parameters in the analysis and design of shield tunnels. The longitudinal variation of input parameters is modeled with the random field concept. The effect of the longitudinal variation of input parameters on the performance of a shield tunnel (referred to herein as the structural safety and serviceability of all tunnel segment rings) is studied with a simplified finite element method (FEM) procedure as well as a force method-based analytical solution model. Furthermore, the robust design concept is integrated into the design of shield

tunnels to guard against longitudinal variation of input parameters. In the following chapters, the improved design methodology of shield tunnels is formulated in detail, and the effectiveness of this method is demonstrated with illustrative examples.

Objectives and Dissertation Organization

The objectives of this research are to (1) develop a simplified FEM procedure to analyze the longitudinal behavior of shield tunnels considering the longitudinal variation of input parameters, (2) derive a force method-based analytical solution of shield tunnel performance that can explicitly consider the effects of tunnel longitudinal behavior, and (3) formulate an improved design methodology of shield tunnels that can explicitly consider design robustness against longitudinal variation of input parameters.

This dissertation consists of five chapters. In Chapter II, a simplified FEM procedure to analyze tunnel longitudinal behavior that arises from the longitudinal variation of input parameters is developed. Here, the tunnel longitudinal structure is simulated with a continuous elastic beam and the soil-structure interaction between the tunnel structure and the ground is modeled with the Winkler elastic ground and load effects, and the longitudinal variation of input parameters is modeled with the random field concept. In Chapter III, a force method-based analytical solution of shield tunnel performance is derived. The effect of tunnel longitudinal behavior, which is analyzed using the developed FEM procedure in Chapter II, on the structure safety and serviceability of tunnel segment ring is explicitly considered through the shearing and flattening effect. In Chapter IV, a robust design methodology of one tunnel segment ring

is presented. Here, uncertain input parameters are modeled with a fuzzy sets concept, and the robust design of the tunnel cross section is set up as a multi-objective optimization problem that maximizes design robustness and cost efficiency, while conventional performance component is formulated as a compulsory design constraint. In Chapter V, the robust design concept is applied to a design of the tunnel longitudinal structure that consists of hundreds of segment rings. The FME procedure (developed in Chapter II) and the analytical solution (developed in Chapter III) are employed as the solution model of shield tunnel performance analysis, and the design robustness measure (formulated in Chapter IV) is utilized for the tunnel longitudinal structure analysis. Finally, in Chapter VI the main conclusions of this dissertation are presented.

CHAPTER TWO

SIMPLIFIED PROCEDURE FOR FINITE ELEMENT ANALYSIS OF THE LONGITUDINAL PERFORMANCE OF SHIELD TUNNELS CONSIDERING SPATIAL VARIABILITY IN LONGITUDINAL DIRECTION[*]

Introduction

Since the first shield tunnel was completed in London 170 years ago, shield tunneling has gained greater popularity for its flexibility, cost electiveness and minimum impact on ground traffic and surface structures (Lee et al. 2001). While the design methodology of shield tunnels evolves from empirical models to the mechanics-based models, the current practice of the design of the segmental lining is still based upon the analysis of critical tunnel cross sections, assuming a plane strain condition (Wood 1975; Bobet 2001; Lee et al. 2001; Koyama 2003). Furthermore, the selection of critical sections is quite subjective; it may be selected as the section with the deepest overburden, the shallowest overburden, or the lowest groundwater table; it may be selected as the section with large surcharge, eccentric loads, or unlevelled surface; or it may be selected at location where there is an adjacent tunnel at present or in the future (ITA 2000). However, for a shield tunnel that is hundreds or thousands of meters in length, the longitudinal variation of design parameters, which can be caused by the tunnel alignment,

---

[*] A similar form of this chapter has been submitted to a journal at the time of writing: Huang, H., Gong, W., Khoshnevisan, S., Juang, C.H., Zhang, D., and Wang, L. (2014). "Simplified procedure for finite element analysis of the longitudinal performance of shield tunnels considering spatial soil variability in longitudinal direction." Computer and Geotechnics (under review).

spatial variation of soil properties, and nearby underground construction, is quite likely and should be considered in the design (ATRB 2000; ITA 2000; Koyama 2003). In particular, a more rational design of the shield tunnel should consider the longitudinal performance of the tunnel (referred to herein as the tunnel differential settlement, longitudinal rotation, longitudinal shear force and longitudinal bending moment) caused by the longitudinal variation of design parameters.

The longitudinal performance of a shield tunnel and its influence on the circumferential behavior (referred to herein as the structure safety and serviceability) of tunnel segment lining may be investigated using numerical models implemented in software such as ABAQUS, ANSYS, and PLAXIS. However, the design of a shield tunnel based upon such numerical models is often computationally prohibitive in practice. A more feasible approach to analyze the tunnel longitudinal performance is to model the longitudinal structure of shield tunnels as a continuous elastic beam (Shiwa et al. 1986; Talmon and Bezuijen 2013). Then, the effect of longitudinal joints (referred to herein as the joints between segmental rings) on the flexural stiffness of tunnel longitudinal structure is modeled through a reduction factor of tunnel longitudinal flexural stiffness (Liao et al. 2008; Huang et al. 2012); and the soil-structure interaction between the tunnel longitudinal structure and the ground under the tunnel is simulated with Winkler model (Winkler 1867), Pasternak model (Pasternak 1954), or Kerr model (Kerr 1965), while the overburden of the tunnel is represented with a pressure load and/or concentrated loads. Based on these assumptions, the analytical solution of tunnel longitudinal performance can readily be derived. Further, the effect of tunnel longitudinal

performance on the circumferential behavior of the segment lining may be analyzed by considering simultaneously the shearing effect (Liao et al. 2008) and the flattening effect (Huang et al. 2012).

Because of the inevitable length of shield tunnels, the effect of the spatial variation of soil properties on the tunnel longitudinal performance is often significant and must be explicitly considered. The spatial variation (in the longitudinal domain) of soil properties tends to complicate the numerical analysis and analytical solution of tunnel longitudinal performance. Therefore, the main goal of this paper is to derive a simplified procedure for FEM analysis of tunnel longitudinal performance that considers the longitudinal variation of tunnel design parameters such as the soil properties of the ground under the tunnel. Note that the spatial variation of the ground under the tunnel may refer to either the spatial variation of different types of ground under the tunnel or the spatial variation of soil properties within the same ground under the tunnel (Fenton 1999). In this paper, our focus is placed on the latter, although the former is also analyzed to validate the FEM model that is derived in this paper.

This paper is organized as follows. First, a simplified procedure for FEM analysis of the tunnel longitudinal performance is developed. Second, the developed FEM procedure is verified with both analytical solutions and model tests. Third, the random field concept is introduced to simulate the spatial variation (in the longitudinal domain) of soil properties of the ground under the tunnel. Finally, a hypothetical illustrative example is presented to demonstrate how the tunnel longitudinal performance is affected by the spatial variation of soil properties of the ground under the tunnel.

Formulations of the Simplified FEM Procedure

In this section, a simplified procedure for FEM analysis of the tunnel longitudinal performance that considers the longitudinal variation of tunnel design parameters is derived. In which, the tunnel longitudinal structure is modeled with a continuous beam (Shiwa et al. 1986; Talmon and Bezuijen 2013) and the effect of tunnel longitudinal joints is simulated with a reduction factor of tunnel longitudinal flexural stiffness (Liao et al. 2008); the soil-structure interaction between the tunnel beam and the ground under the tunnel is modeled with Winkler elastic ground model (Winkler 1867), and the overburden of the tunnel is represented with the pressure load and/or concentrated loads. These are the conditions for formulating the FEM procedure herein, although other models (e.g., the more comprehensive beam-joint model instead of the continuous beam model) may be adopted. It should be noted that while the subject of beam on elastic (or elastoplastic) foundation, or the beam-soil spring model, is not new (Hiroshi and Takeshi 1987; Klar et al. 2007; Yankelevsky 1988; Zhang and Huang 2014), the FEM solution presented in this paper is formulated specifically to consider the longitudinal variation of tunnel design parameters, the effect of which has never been studied.

Local stiffness matrix $[\boldsymbol{K}]^e$ and local load vector $[\boldsymbol{F}]^e$

For an elastic beam element on the Winkler elastic ground, the stiffness matrix of the element, denoted as $[\mathbf{K}]^{\mathbf{e}}$, can be determined with the stiffness matrices of both the elastic beam and the ground under the beam. The load vector of the element, denoted as $[\mathbf{F}]^{\mathbf{e}}$, consists of both the pressure load and the concentrated loads applied on the element.

To derive the element stiffness matrix $[\mathbf{K}]^{\mathbf{e}}$ and load vector $[\mathbf{F}]^{\mathbf{e}}$ that can consider the longitudinal variation of soil properties of the ground under the tunnel and in the overburden of the tunnel in the FEM model of the tunnel longitudinal performance, the following assumptions are made: (1) both the pressure load (q) and the subgrade reaction coefficient (k) within an element, depicted in Figure 2.1(a) & 2.1(b), respectively, can be approximated with the nodal values at both ends of the element using linear interpolation; and (2) tunnel settlement (w; referred to herein as the vertical deformation of tunnel structure) within an element can be modeled with the deformation pattern of a two-node Hermite element (Lu et al. 2004). These assumptions are quite valid when the size of the element mesh in the FEM solution is relatively small.

Based upon the first assumption, the pressure load (q) and the subgrade reaction coefficient (k) within the element can be expressed as follows, respectively:

$$q(\xi) = q_1 + (q_2 - q_1)\xi \tag{2.1a}$$

$$k(\xi) = k_1 + (k_2 - k_1)\xi \tag{2.1b}$$

where q_1 and q_2 = the pressure loads at the left end (referred to Node 1 in Figure 2.1) and the right end (referred to Node 2 in Figure 2.1) of the element, respectively; k_1 and k_2 = the subgrade reaction coefficients at the left end and the right end of the element, respectively; and, ξ = a shape factor ranging from 0 to 1.0, which is used herein to represent the relative position within the element and estimated as:

$$\xi = \frac{x - x_1}{l} \quad (l = x_2 - x_1,\ x_1 \le x \le x_2) \tag{2.1c}$$

where l = the longitudinal length of the tunnel element of concern; x_1 and x_2 = the longitudinal coordinates of the left end and the right end of the element, respectively.

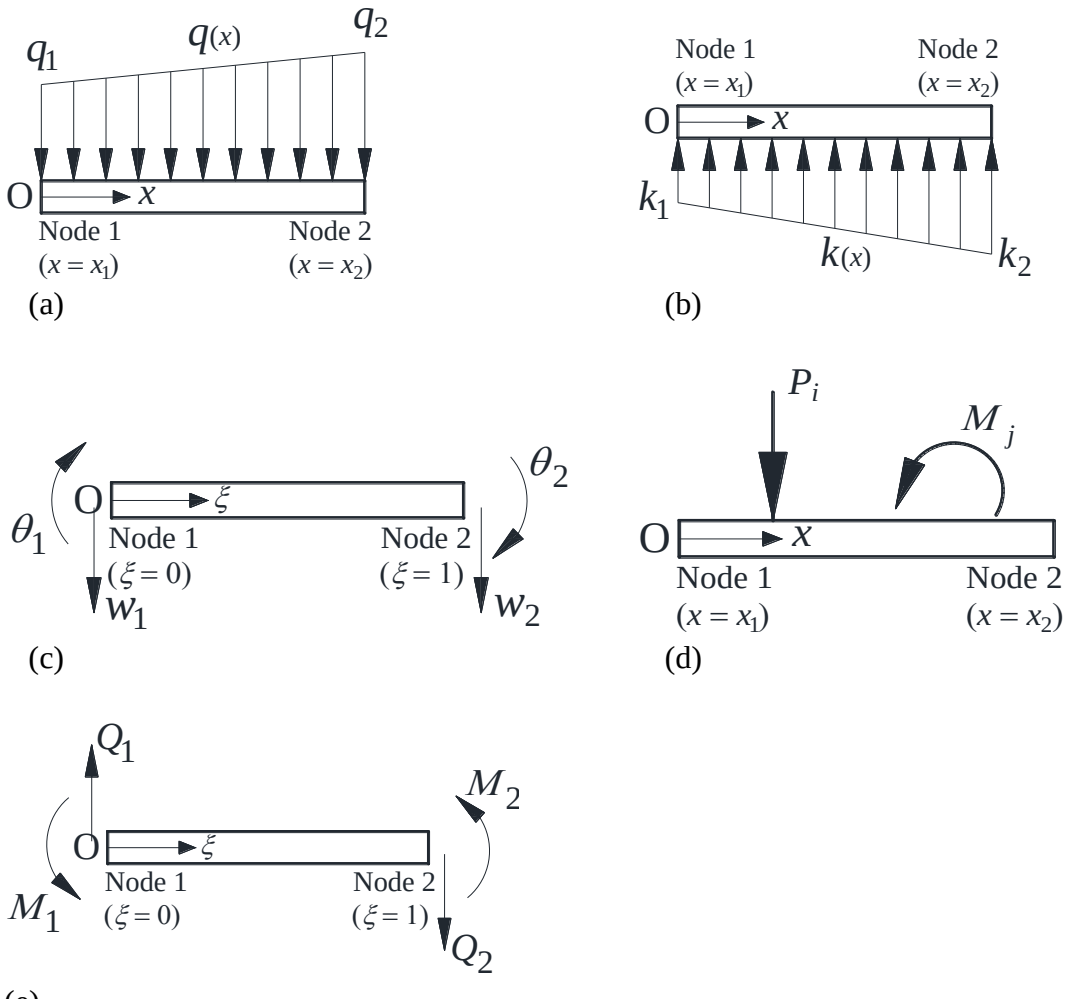

Figure 2.1: Formulation of tunnel element for longitudinal performance analysis: (a) Pressure load $q(x)$; (b) Subgrade reaction coefficient $k(x)$; (c) Nodal displacement $[\boldsymbol{a}]^{\mathbf{e}}$; (d) Concentrated loads; (e) Load vector $[\mathbf{F}]^{\mathbf{e}}$

Based upon the second assumption, the settlement (w) within the element can be computed as follows:

$$w(\xi)=\sum_{i=1}^{2}H_i^{(0)}(\xi)w_i+\sum_{i=1}^{2}H_i^{(1)}(\xi)\theta_i=\sum_{i=1}^{4}N_i(\xi)a_i=[\boldsymbol{N}][\boldsymbol{a}]^{\mathbf{e}} \tag{2.2}$$

where w_1 and w_2 = the settlements at the left end and the right end of the element, respectively; θ_1 and θ_2 = the longitudinal rotations at the left end and the right end of the element, respectively; and, [$\boldsymbol{N}$] and [$\boldsymbol{a}$]$^{\mathbf{e}}$ = the interpolation vector and the nodal deformation vector that are adopted within the two-node Hermite element, respectively. The terms [$\boldsymbol{N}$] and [$\boldsymbol{a}$]$^{\mathbf{e}}$ are set up as (Lu et al. 2004):

$$\begin{aligned}[\boldsymbol{N}]&=[H_1^{(0)}(\xi)\quad H_1^{(1)}(\xi)\quad H_2^{(0)}(\xi)\quad H_2^{(1)}(\xi)]\\&=[1-3\xi^2+2\xi^3\quad (\xi-2\xi^2+\xi^3)l\quad 3\xi^2-2\xi^3\quad (\xi^3-\xi^2)l]\end{aligned} \tag{2.3a}$$

$$[\boldsymbol{a}]^{\mathbf{e}}=[\omega_1\quad \theta_1\quad \omega_2\quad \theta_2]^{\mathrm{T}},\ \text{in which}\ \theta_i=\left(\frac{dw}{dx}\right)_{x=x_i}\quad (i=1\ \text{and}\ 2) \tag{2.3b}$$

As depicted in Figure 2.1(c), the following sign conventions are adopted for the nodal deformation vector [$\boldsymbol{a}$]$^{\mathbf{e}}$: the settlement (w) is taken as positive when it moves downward and the longitudinal rotation (θ) is taken as positive when it yields a clockwise rotation. In general, the tunnel longitudinal structure may also be subject to the concentrated loads such as vertical load (P) and moment (M), as illustrated in Figure 2.1(d). The vertical load (P) is regarded as positive when it yields a downward movement and the moment (M) is treated as positive when it yields a counterclockwise rotation.

Next, the energy concept is employed to derive the element equilibrium equation. The potential energy of the tunnel element shown in Figure 2.1, denoted as Π_p, can be computed as follows:

$$\begin{aligned}\Pi_p &= \int_{x_1}^{x_2} \frac{1}{2} E(x) I(x) \left(\frac{d^2 w}{dx^2} \right)^2 dx + \int_{x_1}^{x_2} \frac{1}{2} k(x) D w^2 dx - \int_{x_1}^{x_2} q(x) D w dx - \sum_i P_i w_i + \sum_j M_j \left(\frac{dw}{dx} \right)_j \\ &= \int_{x_1}^{x_2} \frac{1}{2} E(x) I(x) \left(\frac{d^2 [\boldsymbol{N}][\boldsymbol{a}]^{\mathbf{e}}}{dx^2} \right)^2 dx + \int_{x_1}^{x_2} \frac{1}{2} k(x) D \left([\boldsymbol{N}][\boldsymbol{a}]^{\mathbf{e}} \right)^2 dx - \int_{x_1}^{x_2} q(x) D \left([\boldsymbol{N}][\boldsymbol{a}]^{\mathbf{e}} \right) dx \\ &\quad - \sum_i P_i \left[\boldsymbol{N}(x_i) \right] [\boldsymbol{a}]^{\mathbf{e}} + \sum_j M_j \frac{d \left[\boldsymbol{N}(x_j) \right] [\boldsymbol{a}]^{\mathbf{e}}}{dx}\end{aligned} \tag{2.4}$$

where $E(x)$ and $I(x)$ = the elastic modulus of the segmental lining and the inertia moment of tunnel longitudinal structure at the longitudinal coordinate of x, respectively; and, D = the outer diameter of the segmental lining.

Note that the deformation vector of the tunnel element, $[\boldsymbol{a}]^{\mathbf{e}}$, that satisfies the element equilibrium equation can be determined by minimizing the potential energy of the element, Π_p, and the minimum value of Π_p is achieved by solving following equation:

$$\frac{\partial \Pi_p}{\partial [\boldsymbol{a}]^{\mathbf{e}}} = 0 \tag{2.5}$$

Substituting Eq. (2.4) into Eq. (2.5):

$$\frac{\partial \Pi_{\mathrm{p}}}{\partial [\boldsymbol{a}]^{\mathbf{e}}} = \int_0^1 \frac{E(\xi) I(\xi)}{l^3} \left(\frac{d^2[\boldsymbol{N}]}{d\xi^2} \right)^{\mathrm{T}} \left(\frac{d^2[\boldsymbol{N}]}{d\xi^2} \right) [\boldsymbol{a}]^{\mathbf{e}} \, d\xi + \int_0^1 k(\xi) Dl [\boldsymbol{N}]^{T} [\boldsymbol{N}] [\boldsymbol{a}]^{\mathbf{e}} \, d\xi - \int_0^1 q(\xi) Dl [\boldsymbol{N}]^{\mathrm{T}} \, d\xi$$
$$- \sum_i P_i \left[N(\xi_i) \right]^{\mathrm{T}} + \sum_j \frac{M_j}{l} \frac{d\left[N(\xi_j) \right]^{\mathrm{T}}}{d\xi}$$
$$= 0 \tag{2.6a}$$

Further, Eq. (2.6a) can be simplified as:

$$[\mathbf{K}]^{\mathbf{e}} [\boldsymbol{a}]^{\mathbf{e}} = [\mathbf{F}]^{\mathbf{e}} \tag{2.6b}$$

where,

$$[\mathbf{K}]^{\mathbf{e}} = [\mathbf{KB}]^{\mathbf{e}} + [\mathbf{KG}]^{\mathbf{e}} = \int_0^1 \frac{E(\xi) I(\xi)}{l^3} \left(\frac{d^2[\boldsymbol{N}]}{d\xi^2} \right)^{\mathrm{T}} \left(\frac{d^2[\boldsymbol{N}]}{d\xi^2} \right) d\xi + \int_0^1 k(\xi) Dl [\boldsymbol{N}]^{\mathrm{T}} [\boldsymbol{N}] d\xi \tag{2.7a}$$

$$[\mathbf{F}]^{\mathbf{e}} = \int_0^1 q(\xi) Dl [\boldsymbol{N}]^{\mathrm{T}} \, d\xi + \sum_i P_i \left[N(\xi_i) \right]^{\mathrm{T}} - \sum_j \frac{M_j}{l} \frac{d\left[N(\xi_j) \right]^{\mathrm{T}}}{d\xi} \tag{2.7b}$$

As can be seen, $[\mathbf{KB}]^{\mathbf{e}}$ and $[\mathbf{KG}]^{\mathbf{e}}$ are the stiffness matrices of the element that arise from the elastic beam, $\int_0^1 \frac{E(\xi) I(\xi)}{l^3} \left(\frac{d^2[\boldsymbol{N}]}{d\xi^2} \right)^{\mathrm{T}} \left(\frac{d^2[\boldsymbol{N}]}{d\xi^2} \right) d\xi$, and the ground, $\int_0^1 k(\xi) Dl [\boldsymbol{N}]^{\mathrm{T}} [\boldsymbol{N}] d\xi$, respectively.

As mentioned previously, the tunnel longitudinal structure is approximated in this paper as a continuous beam, in which the flexural stiffness of the tunnel longitudinal

structure, in terms of $E(x)I(x)$ or $E(\xi)I(\xi)$, is a constant that does not vary in the longitudinal domain; and the effect of longitudinal joints on tunnel longitudinal flexural stiffness is modeled through a reduction factor, denoted as ζ (Liao et al. 2008; Huang et al. 2012). Thus, the stiffness matrix of the element that is attributed to the elastic beam, $[\mathbf{KB}]^{\mathbf{e}}$, and to the Winkler elastic ground, $[\mathbf{KG}]^{\mathbf{e}}$ can be integrated as follows, respectively:

$$\left[\mathbf{KB}\right]^{\mathbf{e}} = \frac{\zeta EI}{l^3}\begin{bmatrix} 12 & 6l & -12 & 6l \\ 6l & 4l^2 & -6l & 2l^2 \\ -12 & -6l & 12 & -6l \\ 6l & 2l^2 & -6l & 4l^2 \end{bmatrix} \tag{2.8a}$$

$$\left[\mathbf{KG}\right]^{\mathbf{e}} = Dl\begin{bmatrix} \frac{13}{35}k_1+\frac{3}{35}(k_2-k_1) & \frac{11}{210}k_1l+\frac{1}{60}(k_2-k_1)l & \frac{9}{70}k_1+\frac{9}{140}(k_2-k_1) & -\frac{13}{420}k_1l-\frac{1}{70}(k_2-k_1)l \\ \frac{11}{210}k_1l+\frac{1}{60}(k_2-k_1)l & \frac{1}{105}k_1l^2+\frac{1}{280}(k_2-k_1)l^2 & \frac{13}{420}k_1l+\frac{1}{60}(k_2-k_1)l & -\frac{1}{140}k_1l^2-\frac{1}{280}(k_2-k_1)l^2 \\ \frac{9}{70}k_1+\frac{9}{140}(k_2-k_1) & \frac{13}{420}k_1l+\frac{1}{60}(k_2-k_1)l & \frac{13}{35}k_1+\frac{2}{7}(k_2-k_1) & -\frac{11}{210}k_1l-\frac{1}{28}(k_2-k_1)l \\ -\frac{13}{420}k_1l-\frac{1}{70}(k_2-k_1)l & -\frac{1}{140}k_1l^2-\frac{1}{280}(k_2-k_1)l^2 & -\frac{11}{210}k_1l-\frac{1}{28}(k_2-k_1)l & \frac{1}{105}k_1l^2+\frac{1}{168}(k_2-k_1)l^2 \end{bmatrix} \tag{2.8b}$$

where ζEI is the equivalent flexural stiffness of tunnel longitudinal structure, which can be computed as $\zeta EI = \frac{\pi}{64}\zeta E\left[D^4-\left(D-2t\right)^4\right]$; and, t is the thickness of segmental lining. Here, the derivation of the reduction factor of tunnel longitudinal flexural stiffness (ζ) can be found in the work of Liao et al. (2008), and the subgrade reaction coefficient of the Winkler elastic ground (k) may be estimated from either the plate-load test data (Lin et al. 1998) or the elastic modulus and Poisson's ratio of the soil determined with

laboratory tests (Terzaghi 1955; Horvath 1983; Daloglu and Vallabhan 2000; Sadrekarimi and Akbarzad 2009; Zhang and Huang 2014).

The load vector $[\mathbf{F}]^{\mathbf{e}}$ of the element, defined in Eq. (2.6b), can be integrated as:

$$[\mathbf{F}]^{\mathbf{e}} = \begin{bmatrix} Q_1 \\ M_1 \\ Q_2 \\ M_2 \end{bmatrix} = Dl \begin{bmatrix} \frac{1}{2}q_1 + \frac{3}{20}(q_2 - q_1) \\ \frac{1}{12}q_1 l + \frac{1}{30}(q_2 - q_1) l \\ \frac{1}{2}q_1 + \frac{7}{12}(q_2 - q_1) \\ -\frac{1}{12}q_1 l - \frac{1}{20}(q_2 - q_1) l \end{bmatrix} + \sum_i P_i \left[N(\xi_i) \right]^{\mathrm{T}} - \sum_j \frac{M_j}{l} \frac{d\left[N(\xi_j) \right]^{\mathrm{T}}}{d\xi} \tag{2.9}$$

where Q_1 and Q_2 are the equivalent longitudinal shear forces at the left end and the right end of the element, respectively; M_1 and M_2 are the equivalent longitudinal bending moment at the left end and the right end of the element, respectively. As illustrated in Figure 2.1(e), the following sign conventions are adopted for the nodal force vector $[\mathbf{F}]^{\mathbf{e}}$: the shear force ($Q$) is positive when it yields a clockwise rotation and the bending moment (M) is positive when it yields a counterclockwise rotation.

*Global stiffness matrix [**K**] and load vector [**F**] of tunnel longitudinal structure*

Based on the developed local stiffness matrix $[\mathbf{K}]^{\mathbf{e}}$ and local load vector $[\mathbf{F}]^{\mathbf{e}}$ of the tunnel element (see Eq. 2.8 & 2.9, respectively), the global stiffness matrix, denoted as [**K**], and global load vector, denoted as [**F**], of the whole tunnel longitudinal structure can be assembled accordingly. The procedures to assemble the global stiffness matrix [**K**] and global load vector [**F**] are summarized as follows:

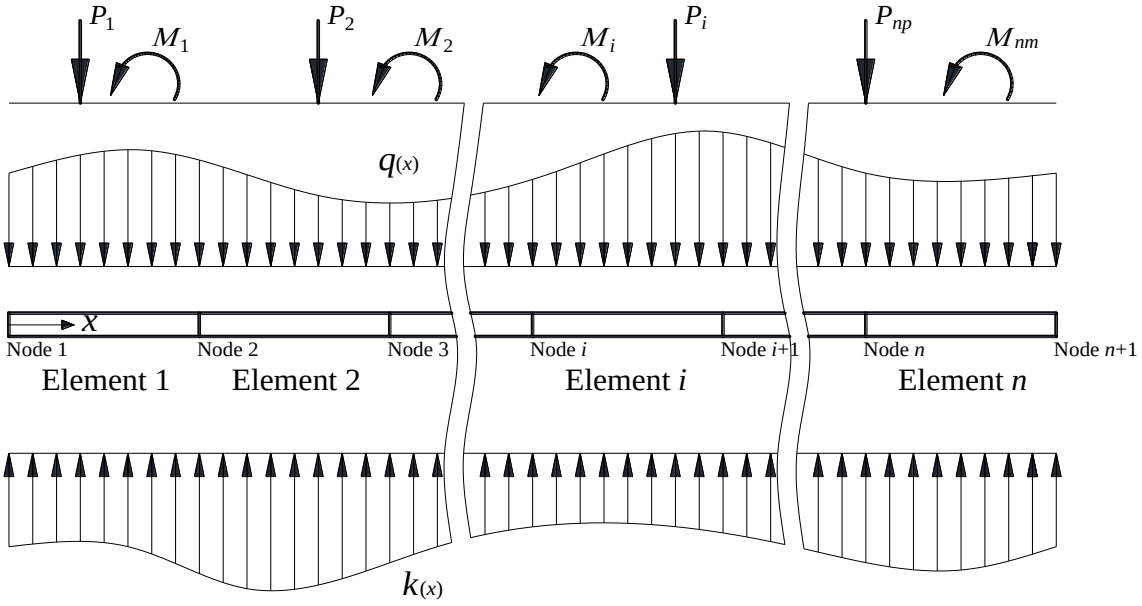

Figure 2.2: Schematic diagram of tunnel longitudinal performance problem

1) For a given tunnel longitudinal performance problem shown in Figure 2.2, the whole tunnel longitudinal structure is first discretized into n elements of the same size; and thus, the longitudinal coordinates of the resulting (n+1) nodes are readily identified.

2) Initialize the global stiffness matrix [**K**] and global load vector [**F**] as [**K**] = 0 and [**F**] = 0, respectively. The dimension of [**K**] is 2(n+1) by 2(n+1) and that of [**F**] is 2(n+1) by 1, since there are two degrees of freedom (DOF; herein including the vertical deformation w and longitudinal rotation θ), for each and every node in the developed FEM solution. Note that the term $K_{i,j}$ within [**K**] can be interpreted as the nodal force required at j^{th} DOF to generate a unit displacement at i^{th} DOF. The term $F_{i,1}$ within [**F**] is the equivalent load at i^{th} DOF, which is caused by the pressure load (q) and concentrated loads (i.e., vertical load P and moment M) on the tunnel.

3) For the discretized element *i* of the tunnel longitudinal structure, develop the local element stiffness matrix $[\mathbf{K}]^{(i)}$ and local element load vector $[\mathbf{F}]^{(i)}$ following the formulations in Eq. (2.8) & (2.9), respectively.

4) Update the global stiffness matrix [**K**] and global load vector [**F**] with the element stiffness matrix of $[\mathbf{K}]^{(i)}$ and element load vector $[\mathbf{F}]^{(i)}$ obtained in Step 3, respectively. Here, the term $K_{2(i-1)+im,2(i-1)+in}$ within [**K**] is updated with $K_{im,in}^{(i)}$ within $[\mathbf{K}]^{(i)}$ as $K_{2(i-1)+im,2(i-1)+in} = K_{2(i-1)+im,2(i-1)+in} + K_{im,in}^{(i)}$ (*im* and *in* = 1, 2, 3, and 4). Similarly, the term $F_{2(i-1)+im,1}$ within [**F**] is updated with $F_{im,1}^{(i)}$ within $[\mathbf{F}]^{(i)}$ as $F_{2(i-1)+im,1} = F_{2(i-1)+im,1} + F_{im,1}^{(i)}$.

5) Repeat the procedures in Step 3 and Step 4 for each and every discretized element of the whole tunnel longitudinal structure. Thus, the global stiffness matrix [**K**] and global load vector [**F**] are assembled.

Boundary conditions

The global equilibrium equation of the whole tunnel longitudinal structure, in the context of FEM solution of tunnel longitudinal performance, can be set up as follows:

$$[\mathbf{K}][\Delta] = [\mathbf{F}] \tag{2.10}$$

where [**K**] and [**F**] = the global stiffness matrix and global load vector, respectively, which can be determined for a specific tunnel longitudinal performance problem using the procedures described above; and, [Δ] = the global deformation vector that is to be

solved. The global deformation vector [$\boldsymbol{\Delta}$] is a 2(n+1) by 1 vector and can be expressed as follows:

$$[\boldsymbol{\Delta}] = [\omega_1 \quad \theta_1 \quad \cdots \quad \omega_i \quad \theta_i \quad \cdots \quad \omega_{n+1} \quad \theta_{n+1}]^{\mathrm{T}} \tag{2.11}$$

where $\theta_i = \left(\frac{dw}{dx}\right)_i \ (i = 1, 2, \cdots, n+1)$.

While the global deformation vector [$\boldsymbol{\Delta}$] of the tunnel longitudinal structure can readily be solved with the global equilibrium equation in Eq. (2.10), the boundary conditions must be determined and incorporated into this solution. In general, two kinds of boundary conditions may be encountered for each and every degree of freedom (DOF) in the FEM solution: free-boundary condition and fixed-boundary condition. As noted in Eq. (2.10), all the degrees of freedom within the global deformation vector [$\boldsymbol{\Delta}$] are implicitly considered with the free-boundary condition; and hence, the fixed-boundary condition should be studied with special attention.

Although many approaches are available to deal with the fixed-boundary condition in an FEM solution (Dhatt et al. 2012), the following procedure is found effective. Here, the global stiffness matrix [**K**] and global load vector [**F**] in Eq. (2.10) are further updated to account for the fixed-boundary condition: if the j^{th} DOF of tunnel longitudinal structure is subject to a fixed-boundary condition (e.g., a given displacement), the terms within [**K**] should be updated as $\mathrm{K}_{j,jm} = 0$, $\mathrm{K}_{jm,j} = 0$, and $\mathrm{K}_{j,j} = 1$ (jm = 1, 2, …, and 2n+2), while the term $\mathrm{F}_{j,1}$ within [**F**] is updated as $\mathrm{F}_{j,1}$ = the given displacement at j^{th} DOF.

Post-processing of FEM solution

Furthermore, the internal forces of the tunnel longitudinal structure, including both the longitudinal bending moment *(M_L)* and the longitudinal shear force (Q_L), along the longitudinal position can be computed with the knowledge of the global deformation vector [**Δ**] and local stiffness matrix of the element $[\mathbf{KB}]^{\mathbf{e}}$. Note that the following sign conventions are adopted for the internal forces of the tunnel longitudinal structure: the longitudinal bending moment *(M_L)* is treated as positive when the tunnel invert is subject to longitudinal tension and the longitudinal shear force (Q_L) is taken as positive when it yields a clockwise rotation. The procedure to compute the longitudinal shear force and longitudinal bending moment at node i and node (i+1) shown in Figure 2.2 can be summarized as follows:

1) Construct the local stiffness matrix of element i that arises from the elastic beam $[\mathbf{KB}]^{(i)}$ (see Eq. 2.8a).

2) Extract the nodal deformation of element i, $[\boldsymbol{a}]^{(i)}$, from the solved global deformation vector [**Δ**] as follows:

$$[\boldsymbol{a}]^{(i)} = [w_i \quad \theta_i \quad w_{i+1} \quad \theta_{i+1}]^{\mathrm{T}} = [\,\Delta_{2(i-1)+1} \quad \Delta_{2(i-1)+2} \quad \Delta_{2(i-1)+3} \quad \Delta_{2(i-1)+4}\,]^{\mathrm{T}}$$

3) Compute the internal forces at node i and node (i+1), in terms of Q_{Li}, M_{Li}, $Q_{L(i+1)}$, and $M_{L(i+1)}$, as follows:

$$[-Q_{Li} \quad M_{Li} \quad Q_{L(i+1)} \quad -M_{L(i+1)}]^{\mathrm{T}} = [\mathbf{KB}]^{(i)} \times [\boldsymbol{a}]^{(i)}$$

Validation of the Developed FEM Solution

The developed FEM solution of the tunnel longitudinal performance should ideally be validated with field data; however, to our knowledge there exists no such database that provides the tunnel longitudinal performance data with details of the longitudinal variation of design parameters. In this paper, the developed FEM solution is verified with both analytical solutions and model tests results, in which the longitudinal variation of the ground under the tunnel is explicitly considered. For simplicity and demonstration purposes, only two scenarios of the longitudinal variation of the ground are investigated, as shown in Figure 2.3.

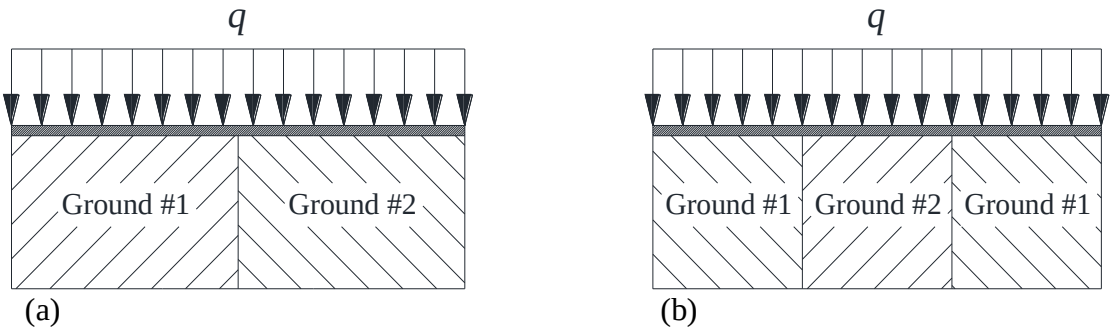

Figure 2.3: Design scenarios of the longitudinal variation of the ground under the tunnel: (a) Scenario 1; (b) Scenario 2

Validation with analytical solutions

For a continuous elastic beam on the Winkler elastic ground, the vertical deformation or settlement (w) of the beam can be obtained by solving the following differential equation:

$$\frac{d^4w}{dx^4}+4\lambda(x)^4w(x)=\frac{q(x)D}{\zeta E(x)I(x)} \tag{2.12}$$

where $\lambda(x) = \sqrt[4]{\frac{k(x)D}{4\zeta E(x)I(x)}}$. For simplicity, the pressure $q(x)$ and the subgrade reaction coefficient $k(x)$ can be approximated as constants within a small longitudinal length; and thus, solving Eq. (2.12) in terms of w results in:

$$w(x) = \frac{q}{k} + \mathrm{e}^{\lambda x}\left[C_1\cos(\lambda x) + C_2\sin(\lambda x)\right] + \mathrm{e}^{-\lambda x}\left[C_3\cos(\lambda x) + C_4\sin(\lambda x)\right] \quad (2.13)$$

where C_1, C_2, C_3 and C_4 are constants depending on the boundary conditions of the given problem.

Scenario 1 (Figure 2.3a)

The subgrade reaction coefficient $k(x)$ in the case of Scenario 1 can be expressed as:

$$k(x) = \begin{cases} k_l & (x < 0) \\ k_r & (x \geq 0) \end{cases} \quad (2.14)$$

where k_l and k_r = the subgrade reaction coefficients at the left side and the right side of the longitudinal coordinate of x = 0, respectively. Here, tunnel settlement (w) can be presented as:

$$w(x) = \begin{cases} \frac{q}{k_l} + \mathrm{e}^{\lambda_l x}\left[C_{11}\cos(\lambda_l x) + C_{12}\sin(\lambda_l x)\right] + \mathrm{e}^{-\lambda_l x}\left[C_{13}\cos(\lambda_l x) + C_{14}\sin(\lambda_l x)\right] & (x < 0) \\ \frac{q}{k_r} + \mathrm{e}^{\lambda_r x}\left[C_{21}\cos(\lambda_r x) + C_{22}\sin(\lambda_r x)\right] + \mathrm{e}^{-\lambda_r x}\left[C_{23}\cos(\lambda_r x) + C_{24}\sin(\lambda_r x)\right] & (x \geq 0) \end{cases} \quad (2.15)$$

where $\lambda_l = \sqrt[4]{\frac{k_l D}{4\zeta EI}}$, $\lambda_r = \sqrt[4]{\frac{k_r D}{4\zeta EI}}$; and, C_{11}, C_{12}, C_{13}, C_{14}, C_{21}, C_{22}, C_{23}, and C_{24} are constants that can be solved with following boundary equations:

$$\lim_{x\to 0^-} w(x) = \lim_{x\to 0^+} w(x) \tag{2.16a}$$

$$\lim_{x\to 0^-} \theta(x) = \lim_{x\to 0^+} \theta(x) \tag{2.16b}$$

$$\lim_{x\to 0^-} M_L(x) = \lim_{x\to 0^+} M_L(x) \tag{2.16c}$$

$$\lim_{x\to 0^-} Q_L(x) = \lim_{x\to 0^+} Q_L(x) \tag{2.16d}$$

$$\lim_{x\to \infty} M_L(x) = -\lim_{x\to \infty} \zeta EI \frac{d^2 w}{dx^2} = 0 \tag{2.16e}$$

$$\lim_{x\to \infty} Q_L(x) = -\lim_{x\to \infty} \zeta EI \frac{d^3 w}{dx^3} = 0 \tag{2.16f}$$

$$\lim_{x\to -\infty} M_L(x) = -\lim_{x\to -\infty} \zeta EI \frac{d^2 w}{dx^2} = 0 \tag{2.16g}$$

$$\lim_{x\to -\infty} Q_L(x) = -\lim_{x\to -\infty} \zeta EI \frac{d^3 w}{dx^3} = 0 \tag{2.16h}$$

Based upon the above formulations, the closed form solution of the tunnel longitudinal performance in the case of Scenario 1 can be derived; in which, the derived

values of C_{11}, C_{12}, C_{13}, C_{14}, C_{21}, C_{22}, C_{23}, and C_{24} in Eq. (2.15) are: $C_{11} = -\left(\frac{q}{k_l}-\frac{q}{k_r}\right)\Big/\left[\left(\frac{\lambda_l}{\lambda_r}\right)^2+1\right]$, $C_{12} = \left(\frac{q}{k_l}-\frac{q}{k_r}\right)\left(1-\frac{\lambda_l}{\lambda_r}\right)\Big/\left[\left(\frac{\lambda_l}{\lambda_r}\right)^2+1\right]\left(\frac{\lambda_l}{\lambda_r}+1\right)$, $C_{13} = 0$, $C_{14} = 0$, $C_{21} = 0$, $C_{22} = 0$, $C_{23} = \left(\frac{q}{k_l}-\frac{q}{k_r}\right)\left(\frac{\lambda_l}{\lambda_r}\right)^2\Big/\left[\left(\frac{\lambda_l}{\lambda_r}\right)^2+1\right]$, and $C_{24} = \left(\frac{q}{k_l}-\frac{q}{k_r}\right)\left(\frac{\lambda_l}{\lambda_r}\right)^2\left(\frac{\lambda_l}{\lambda_r}-1\right)\Big/\left[\left(\frac{\lambda_l}{\lambda_r}\right)^3+\left(\frac{\lambda_l}{\lambda_r}\right)^2+\left(\frac{\lambda_l}{\lambda_r}\right)^1+1\right]$.

For this validation analysis, the parameters that define the elastic beam and the Winkler ground are listed in Table 2.1 and Table 2.2, respectively. The comparison between the FEM solution and the analytical solution is performed and the results are plotted in Figure 2.4. For FEM solution, the size of the discretized element is set up as 0.25 m and the FEM mesh of the tunnel longitudinal structure is shown in Figure 2.2. The developed FEM solution yields the identical results as those from the analytical solution for the tunnel settlement (see Figure 2.4a), longitudinal rotation (see Figure 2.4b), longitudinal bending moment (see Figure 2.4c), and longitudinal shear force (see Figure 2.4d).

Table 2.1: Design parameters adopted for assessing tunnel longitudinal performance

Parameter	Value
Elastic modulus of segmental lining (E, kN/m^2) [a]	35.0×10^6
Tunnel outer diameter (D, m) [a]	6.2
Thickness of segmental lining (t, m) [a]	0.35
Tunnel flexural stiffness reduction factor (ζ) [b]	1/7
Pressure load acting on tunnel (q, kN/m^2) [c]	300

[a] Data adopted in Shanghai practice.

[b] Data from literature (Liao et al. 2008).
[c] Data from local experience.

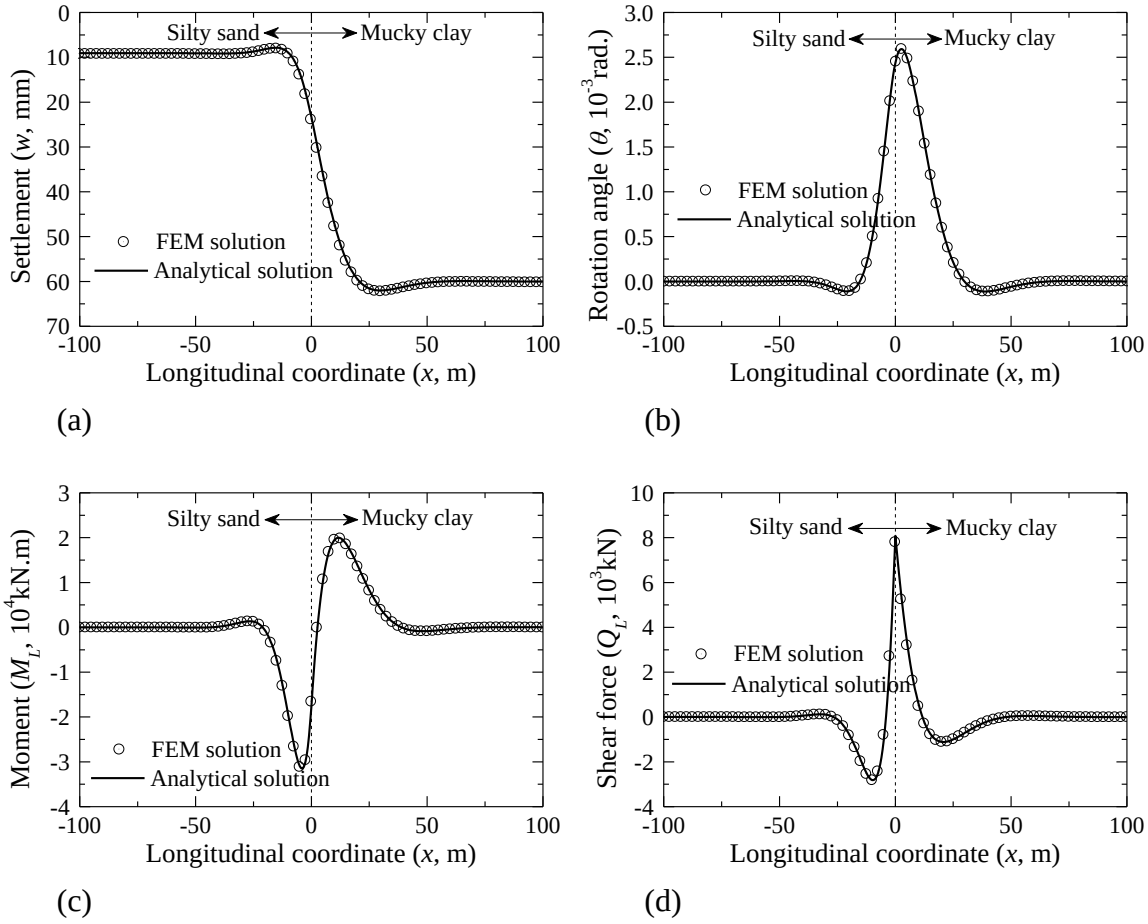

Figure 2.4: FEM solution versus analytical solution for Scenario 1: (a) Tunnel settlement; (b) Tunnel longitudinal rotation; (c) Tunnel longitudinal bending moment; (d) Tunnel longitudinal shear

Table 2.2: Subgrade reaction coefficients of the ground under the tunnel

Design scenario	Parameter	Value
Scenario 1 (see Figure 2.3a)	Subgrade reaction coefficient of ground #1 (or silty sand) (k_l, kN/m^3) [a]	33,000
	Subgrade reaction coefficient of ground #2 (or mucky clay) (k_r, kN/m^3) [a]	5,000
Scenario 2 (see Figure 2.3b)	Subgrade reaction coefficient of ground #1 (or silty sand) (k_l, kN/m^3) [a]	33,000
	Subgrade reaction coefficient of ground #2 (or	5,000

	mucky clay) (k_m, kN/m^3) [a]	
	Subgrade reaction coefficient of ground #1 (or silty sand) (k_r, kN/m^3) [a]	33,000
	Longitudinal length of ground #2 (or mucky clay) (L_m, m) [b]	20

[a] Data from the site investigation of Shanghai metro line 13.
[b] Data from assumption.

Scenario 2 (Figure 2.3b)

The subgrade reaction coefficient $k(x)$ in the case of Scenario 2 can be expressed as:

$$k(x)=\begin{cases}k_l & (x<0)\\ k_m & (0\le x<L_m)\\ k_r & (x\ge l)\end{cases} \tag{2.17}$$

where k_l and k_r = the subgrade reaction coefficients at the left side and the right side of the intermediate ground, respectively; and, k_m and L_m = the subgrade reaction coefficient and the longitudinal length of the intermediate ground, respectively. Here, tunnel settlement (w) is presented as:

$$w(x)=\begin{cases}\dfrac{q}{k_l}+\mathrm{e}^{\lambda_l x}\left[C_{11}\cos(\lambda_l x)+C_{12}\sin(\lambda_l x)\right]+\mathrm{e}^{-\lambda_l x}\left[C_{13}\cos(\lambda_l x)+C_{14}\sin(\lambda_l x)\right] & (x<0)\\ \dfrac{q}{k_m}+\mathrm{e}^{\lambda_m x}\left[C_{21}\cos(\lambda_m x)+C_{22}\sin(\lambda_m x)\right]+\mathrm{e}^{-\lambda_m x}\left[C_{23}\cos(\lambda_m x)+C_{24}\sin(\lambda_m x)\right] & (0\le x<L_m)\\ \dfrac{q}{k_r}+\mathrm{e}^{\lambda_r x}\left[C_{31}\cos(\lambda_r x)+C_{32}\sin(\lambda_r x)\right]+\mathrm{e}^{-\lambda_r x}\left[C_{33}\cos(\lambda_r x)+C_{34}\sin(\lambda_r x)\right] & (x\ge L_m)\end{cases} \tag{2.18}$$

where $\lambda_l = \sqrt[4]{\frac{k_l D}{4\zeta EI}}$, $\lambda_m = \sqrt[4]{\frac{k_m D}{4\zeta EI}}$, $\lambda_r = \sqrt[4]{\frac{k_r D}{4\zeta EI}}$; and, C_{11}, C_{12}, C_{13}, C_{14}, C_{21}, C_{22}, C_{23}, C_{24}, C_{31}, C_{32}, C_{33}, and C_{34} are constants that can be solved with following boundary equations:

$$\lim_{x\to 0^-} w(x) = \lim_{x\to 0^+} w(x) \tag{2.19a}$$

$$\lim_{x\to 0^-} \theta(x) = \lim_{x\to 0^+} \theta(x) \tag{2.19b}$$

$$\lim_{x\to 0^-} M_L(x) = \lim_{x\to 0^+} M_L(x) \tag{2.19c}$$

$$\lim_{x\to 0^-} Q_L(x) = \lim_{x\to 0^+} Q_L(x) \tag{2.19d}$$

$$\lim_{x\to L_m^-} w(x) = \lim_{x\to L_m^+} w(x) \tag{2.19e}$$

$$\lim_{x\to L_m^-} \theta(x) = \lim_{x\to L_m^+} \theta(x) \tag{2.19f}$$

$$\lim_{x\to L_m^-} M_L(x) = \lim_{x\to L_m^+} M_L(x) \tag{2.19g}$$

$$\lim_{x\to L_m^-} Q_L(x) = \lim_{x\to L_m^+} Q_L(x) \tag{2.19h}$$

$$\lim_{x\to \infty} M_L(x) = -\lim_{x\to \infty} \zeta EI \frac{d^2 w}{dx^2} = 0 \tag{2.19i}$$

$$\lim_{x\to\infty} Q_L(x) = -\lim_{x\to\infty} \zeta EI \frac{d^3 w}{dx^3} = 0 \tag{2.19j}$$

$$\lim_{x\to-\infty} M_L(x) = -\lim_{x\to-\infty} \zeta EI \frac{d^2 w}{dx^2} = 0 \tag{2.19k}$$

$$\lim_{x\to-\infty} Q_L(x) = -\lim_{x\to-\infty} \zeta EI \frac{d^3 w}{dx^3} = 0 \tag{2.19l}$$

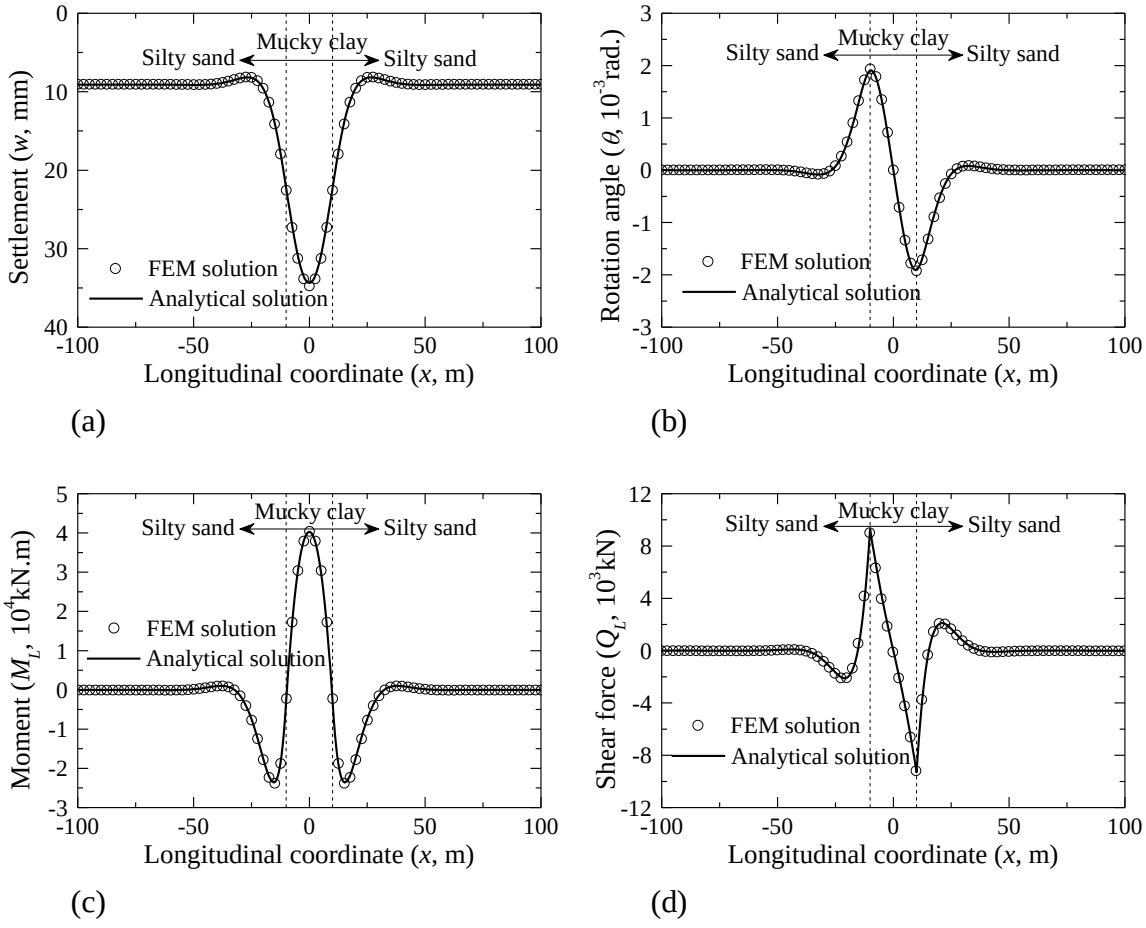

Figure 2.5: FEM solution versus analytical solution for Scenario 2: (a) Tunnel settlement; (b) Tunnel longitudinal rotation: (c) Tunnel longitudinal bending moment; (d) Tunnel longitudinal shear force

Next, the closed form solution of the tunnel longitudinal performance in the case of Scenario 2 is derived. However, the constants C_{11}, C_{12}, C_{13}, C_{14}, C_{21}, C_{22}, C_{23}, C_{24}, C_{31}, C_{32}, C_{33}, and C_{34} are not listed here to save space (over hundreds of lines). Then the comparison between the FEM solution and the analytical solution is performed and the results are shown in Figure 2.5. For FEM solution, the size of the discretized element is set up as 0.25 m and the FEM mesh of the tunnel longitudinal structure is shown in Figure 2.2. Similar to the results for Scenario 1 (see Figure 2.4), the developed FEM solution yields the identical results as those from the analytical solution for the tunnel settlement (see Figure 2.5a), longitudinal rotation (see Figure 2.5b), longitudinal bending moment (see Figure 2.5c), and longitudinal shear force (see Figure 2.5d).

Validation with model tests

The developed FEM solution of the tunnel longitudinal performance is further validated with model tests. In the model tests, the segmental lining is simulated with a high density polyethylene (HDPE) pipe, the elastic modulus of which is 1.373 GPa. The outer diameter of the model tunnel is 160 mm and the thickness of the segmental lining is 9 mm. The width of each segmental ring is 25.8 mm. The segmental rings are connected with six pieces of 17 mm × 7.5 mm × 2 mm plastic chips, the elastic modulus of which is 480 MPa. The longitudinal joints of the model tunnel are located at 0.00°, 45.56°, 112.78°, 180.00°, 247.22°, and 314.44° measured from the tunnel crown and along the tunnel circumferential direction. A total number of 58 segmental rings, with the longitudinal length of 1.4964 m (nearly 10 times of the tunnel diameter), are investigated

in the model tests. The longitudinal flexural stiffness of the model tunnel is measured at 3.038×10^2 N.m^2, which is obtained by testing the simply supported beam.

Figure 2.6: Setup for model tests of 1-D tunnel longitudinal structure

As shown in Figure 2.6, a steel reaction frame is customized for the model test. Here, the pressure loading is applied to the model tunnel crown longitudinally by 5 small jacks while the steel springs are used to simulate the soil-structure interaction between the tunnel longitudinal structure and the ground under the tunnel. The maximum pressure of 11.94 kPa is applied through 5 loading steps. During the tests, the settlement of the model tunnel is measured with the displacement meters. Note that the stiffness of springs can be arbitrarily adjusted to simulate the longitudinal variation of the ground under the tunnel.

Scenario 1 (Figure 2.3a)

To simulate the subgrade reaction coefficients of silty sand and mucky clay, similar principles are employed to determine the stiffness of steel springs and the obtained stiffness of these springs are 419.70 kN/m and 63.55 kN/m, respectively. In the model test with Scenario 1 (see Figure 2.3a), the left side of the ground under the model tunnel longitudinal structure is simulated with the hard spring, while the right side is simulated with the soft spring. Figure 2.7(a) depicts the measured settlement of the model tunnel under the last loading step. Also plotted Figure 2.7(a) is the computed tunnel settlement using the developed FEM procedure. As can be seen, the results obtained from two different approaches agree well with each other.

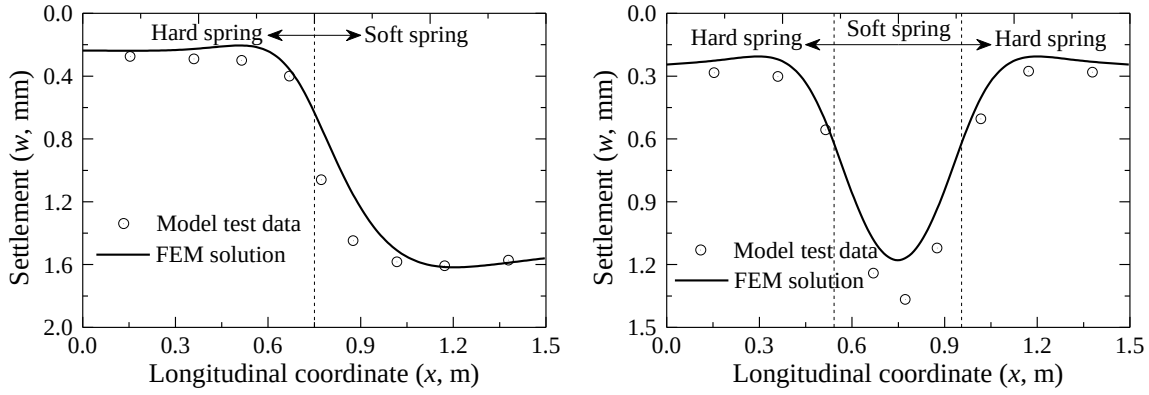

(a) (b)

Figure 2.7: FEM solution versus model tests: (a) Scenario 1; (b) Scenario 2

Scenario 2 (Figure 2.3b)

In the model test with Scenario 2, the ground under the intermediate 16 segmental rings is simulated with the soft spring (to model the mucky clay), while the ground under the left 42 segmental rings is simulated with the hard springs (to model the silty sand). Similar to Figure 2.7(a), Figure 2.7(b) shows the measured settlement of the model tunnel

under the last loading step along with the computed tunnel settlement using the developed FEM procedure. Again, the results obtained from two different approaches agree well with each other. As can be seen, the shield tunnel in the model test is simulated by discrete segmental rings connected by plastic chips, whereas the shield tunnel in the developed FEM solution is modeled by a continuous beam. The good agreement between the results obtained from model tests and those from FEM solution supports the assumption made in this paper, that is, the shield tunnel can be represented with a continuous beam for the analysis of the tunnel longitudinal performance.

In summary, the developed FEM procedure for the tunnel longitudinal performance has been verified with both analytical solutions and model tests. The results also indicate that the shield tunnel can be represented with a continuous beam for the analysis of the tunnel longitudinal performance and the developed FEM model is a satisfactory solution.

Random Field Modeling of the Spatial Variation of Soil Properties

One significant application of the developed FEM procedure is to analyze the tunnel longitudinal performance considering the longitudinal variation (i.e., spatial variation in the longitudinal domain) of soil properties of the ground under the tunnel. Note that the spatial variation of soil properties of the ground under the tunnel may be due to the following situations: (1) existence of different types of ground under the tunnel in the longitudinal direction (e.g., Figure 2.3), and (2) spatial variation of soil properties

within the same ground under the tunnel (Fenton 1999). The first situation was studied in the previous section, and the second situation is examined in this section.

Local averaging within the element domain

In the developed FEM solution of tunnel longitudinal performance, the subgrade reaction coefficient (k) within a tunnel element is represented with the values at two nodes of the element. Note that the performance of the element is indeed dependent upon the averaged subgrade reaction coefficient over the element domain, rather than the subgrade reaction coefficient at the element nodes. Thus, the averaged subgrade reaction coefficient might be taken as the input in the developed simplified FEM model. In such a circumstance, the spatial averaging effect should be considered in the random field modeling of the spatial variation (in the longitudinal domain) of soil properties of the ground under the tunnel (El-Ramly et al. 2002; Fenton and Griffiths 2002 & 2005; Cho 2007; Luo et al. 2011; Luo et al. 2012).

In general, the mean of the averaged subgrade reaction coefficient over the element domain (μ_l) is expected to be equal to the mean of the point subgrade reaction at element nodes (μ). The variance of the averaged subgrade reaction coefficient, however, is less than the variance of the point property when the local averaging effect is taken into account. For simplicity, the variance of the averaged subgrade reaction coefficient within the element domain is computed as follows (Li and Lumb 1987; Cho 2007):

$$\sigma_l^2 = \gamma(l)\sigma^2 \tag{2.20}$$

where σ_l^2 = the variance of the averaged subgrade reaction coefficient within the element domain; σ^2 = the variance of the point subgrade reaction coefficient (k); l = the length of the tunnel element of concern; and, $\gamma(l)$ = a variance reduction factor bounded by 0 and 1.0 and computed as (Cho 2007; Luo et al. 2012):

$$\gamma(l) = \frac{1}{2}\left(\frac{r}{l}\right)^2\left[\frac{2l}{r} - 1 + \exp\left(-\frac{2l}{r}\right)\right] \tag{2.21}$$

where r = the scale of fluctuation of the subgrade reaction coefficient along the tunnel longitudinal direction, within which the subgrade reaction coefficient shows a strong correlation.

The local averaging effect on the correlations among the averaged subgrade reaction coefficients is next considered. Here, the correlation between the averaged subgrade reaction coefficients within different elements (represented by the subgrade reaction coefficients at different element nodes), in terms of k_{x_i} and k_{x_j}, is computed by averaging the correlation between the subgrade reaction coefficients at all points within the element lengths (Cho 2007):

$$\rho(k_{x_i}, k_{x_j}) = \frac{1}{l_i l_j}\int_{x_i-\frac{l_i}{2}}^{x_i+\frac{l_i}{2}}\int_{x_j-\frac{l_j}{2}}^{x_j+\frac{l_j}{2}} \rho(x_2 - x_1)\, d_{x_2} d_{x_1} \tag{2.22}$$

where l_i and l_j = the longitudinal lengths of the element i and the element j, respectively; and, $\rho(x)$ = the autocorrelation function among the point subgrade reaction coefficients. Oftentimes, it is difficult to obtain a closed form solution of Eq. (2.22). Alternatively, a

numerical integration scheme such as the three-point Gauss numerical integration may be employed. In this study, the anisotropic exponential autocorrelation function is used to represent the autocorrelation among the point subgrade reaction coefficients (Cho 2007; Wu et al. 2012):

$$\rho(x) = \exp(-\frac{2|x|}{r}) \tag{2.23}$$

where $|x|$ = the relative longitudinal distance of any two points of concern.

Generating the random field of subgrade reaction coefficients

For illustration purpose, the subgrade reaction coefficient (k) within the same ground is modeled herein with a stationary lognormal random field. While the normal random field might also be used, the lognormal random field is preferred for the non-negative feature of the subgrade reaction coefficient. Thus, the subgrade reaction coefficient at a specific longitudinal coordinate of x_i can be generated as (Luo et al. 2012; Gong et al. 2014a):

$$k(x_i) = \exp\left[\mu_{\mathrm{n}} + \sigma_{\mathrm{n}} \cdot G_{\mathrm{n}}(x_i)\right] \tag{2.24}$$

where μ_{n} and σ_{n} = the mean and standard deviation of $\log(k)$, respectively, which can be computed from the mean (μ_l) and standard deviation (σ_l) of the averaged subgrade reaction coefficient through the following transformations:

$$\sigma_{\mathrm{n}} = \sqrt{\ln\left[1+(\sigma_l/\mu_l)^2\right]} \tag{2.25a}$$

$$\mu_{\mathrm{n}} = \ln \mu_l - \frac{1}{2}\sigma_{\mathrm{n}}^2 \tag{2.25b}$$

The term G_{n} in Eq. (2.24) represents a set of standard normal random variables with the autocorrelation function of $\rho(k_{x_i}, k_{x_j})$ that is formulated in Eq. (2.22). This set of standard normal random variables can be easily generated using Monte Carlo simulation (MCS). Plotted in Figure 2.8 is an example of the generated subgrade reaction coefficients, which are readily used as inputs to the FEM model developed in this paper. For illustration purpose, the longitudinal length of the shield tunnel (L) and the element size (l) are assumed at 200 m and 0.25 m, respectively, and the statistical parameters of the random field of the subgrade reaction coefficient are assumed and listed in Table 2.3.

Table 2.3: Statistical parameters assumed for the random field of subgrade reaction coefficient

Parameter	Value
Mean of point subgrade reaction coefficient (μ, kN/m^3)	33,000
Coefficient of variation (COV) of point subgrade reaction coefficient (δ)	0.5
Scale of fluctuation of log(k) (r, m)	50

Hypothetical Example

A hypothetical illustrative example is presented in this section to demonstrate the analysis of the tunnel longitudinal performance using the developed FEM procedure, in which the spatial variation (in the longitudinal domain) of the subgrade reaction coefficient (k) of the ground under the tunnel is explicitly considered.

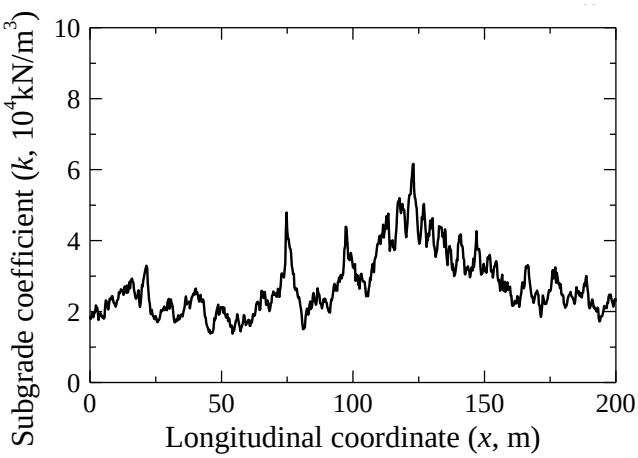

Figure 2.8: An example of the subgrade reaction coefficients generated from MCS

Tunnel longitudinal performance with known subgrade reaction coefficients

First, the longitudinal performance of a shield tunnel on the silty sand with known subgrade reaction coefficient as shown in Figure 2.8 is analyzed with the developed FEM procedure. For this problem, the design parameters of the shield tunnel are listed in Table 2.1, and the longitudinal length of the shield tunnel (L) and the element size (l) are taken as 200 m and 0.25 m, respectively. The FEM mesh of the tunnel longitudinal structure is shown in Figure 2.2. The results of the FEM analysis are shown in Figure 2.9.

As shown in Figure 2.9(a), significant differential settlement of the shield tunnel is observed due to the spatial variation of the subgrade reaction coefficient (k) of the ground under the tunnel (see Figure 2.8). The pattern of the longitudinal variation of tunnel settlement (w) is similar to that of the subgrade reaction coefficient (k) of the ground under the tunnel. The longitudinal position with a larger subgrade reaction coefficient always exhibits a smaller settlement. Similarly, Figure 2.9(b), 2.9(c) and

2.9(d), depict the longitudinal variation of tunnel longitudinal rotation (θ), longitudinal bending moment (M_L), and longitudinal shear force (Q_L) respectively.

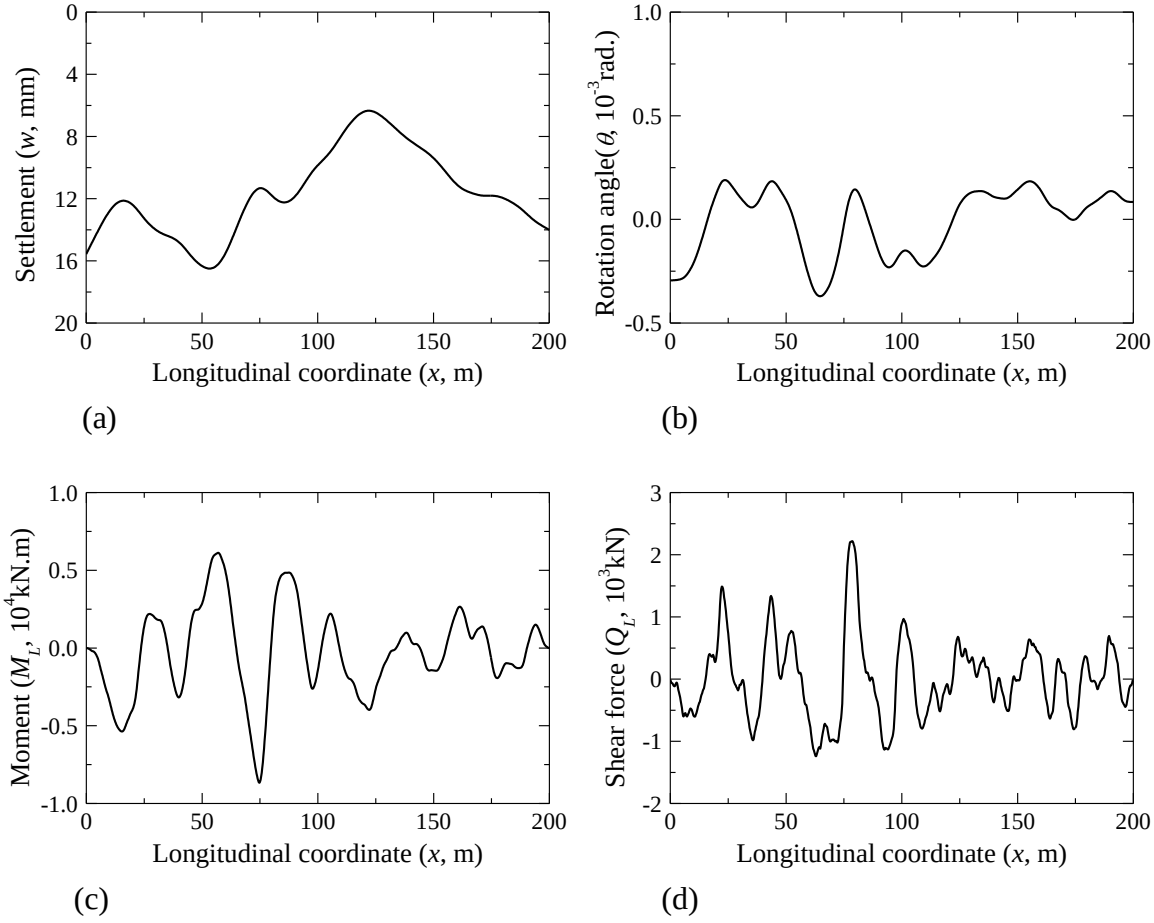

Figure 2.9: Tunnel longitudinal performance predicted using the proposed FEM procedure: (a) Tunnel settlement; (b) Tunnel longitudinal rotation; (c) Tunnel longitudinal bending moment; (d) Tunnel longitudinal shear force

Compared to the scenarios of tunnel longitudinal performance variation in Figure 2.4 and Figure 2.5, the longitudinal variation of tunnel longitudinal performance that is attributed to the spatial variation of soil properties shown in Figure 2.9 is more complex and cannot be expressed with a closed form solution. As formulated previously, the required number of boundary condition equations is already high (i.e., 8 or 12 depending

on different scenarios in Figure 2.3). To further incorporate the spatial variation (in the longitudinal domain) of soil properties, the number of boundary condition equations will be increased by many times, and an analytical solution of the tunnel longitudinal performance could not be achievable. The simplified FEM solution developed in this paper offers a feasible solution in this case.

Longitudinal variation of tunnel settlement

Since the longitudinal rotation, longitudinal bending moment, and longitudinal shear force can readily be computed from the tunnel settlement, the latter is used herein to represent the tunnel longitudinal performance. As such, the longitudinal variation of tunnel longitudinal performance can be studied in this paper by examining the longitudinal variation of tunnel settlement.

As illustrated in Figure 2.9(a), the settlement of the shield tunnel (w) is a field that can be determined with the knowledge of the random field of the subgrade reaction coefficient (k) of the ground under the tunnel. For ease of illustration, the mean, denoted as μ_w, and the coefficient of variation (COV), denoted as δ_w, of the tunnel settlement are used to represent the overall tunnel settlement and the extent of differential settlement, respectively. The mean (μ_w) and COV (δ_w) of the tunnel settlement plotted in Figure 2.9(a) are calculated as 11.65 mm and 0.23, respectively.

As formulated previously, the subgrade reaction coefficients of the ground under the tunnel in the FEM analysis are generated with MCS; naturally, different subgrade reaction coefficient profiles can be generated from different MCS runs, which may result in different tunnel settlement curves. For example, the tunnel settlement curve shown in

Figure 2.9(a) is obtained for the situation where the input subgrade reaction coefficients are shown in Figure 2.8. To derive a converged solution of tunnel settlement statistics, including both the mean (μ_w) and COV (δ_w) of tunnel settlement, 20,000 MCS runs are carried out herein to simulate the spatial variation of the subgrade reaction coefficients of the ground under the tunnel.

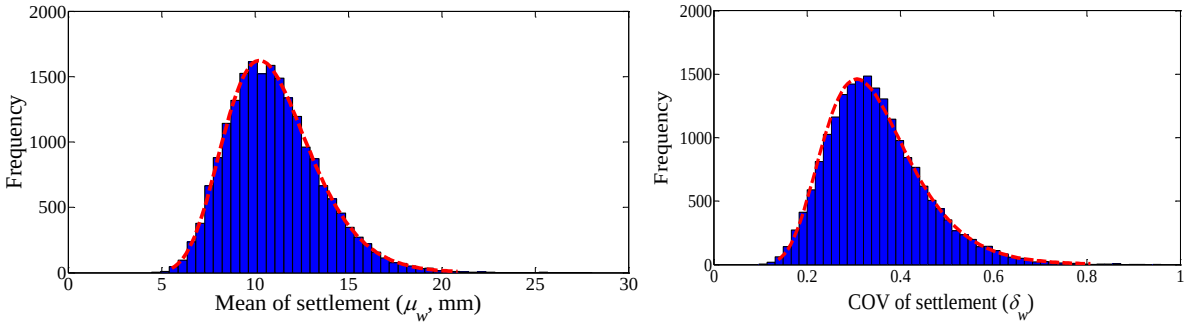

(a) (b)

Figure 2.10: Distribution of tunnel settlement statistics (20,000 MCS runs): (a) Mean of tunnel settlement; (b) COV of tunnel settlement

Figure 2.10(a) and 2.10(b) show the distributions of the mean (μ_w) and COV (δ_w) of the tunnel settlement, respectively, with the results of the 20,000 MCS runs. Also plotted in Figure 2.10 are the fitted lognormal distributions. The results show that the tunnel settlement statistics (i.e., μ_w and δ_w) approximately follow the lognormal distribution. The mean and standard deviation of tunnel settlement statistics are computed with the results of the 20,000 MCS runs. In this example, the mean of μ_w and δ_w are 11.02 mm and 0.35, respectively; and the standard deviation of μ_w and δ_w are 2.47 mm and 0.10, respectively.

Figure 2.11(a) depicts the relationship between the computed mean and standard deviation of μ_w with the number of MCS runs, and Figure 2.11(b) shows the relationship between the computed mean and standard deviation of δ_w with the number of MCS runs. Figure 2.11 shows that converged solutions of tunnel settlement statistics can be achieved with 5,000 MCS runs. Thus, 5,000 MCS runs are employed in the subsequent parametric study.

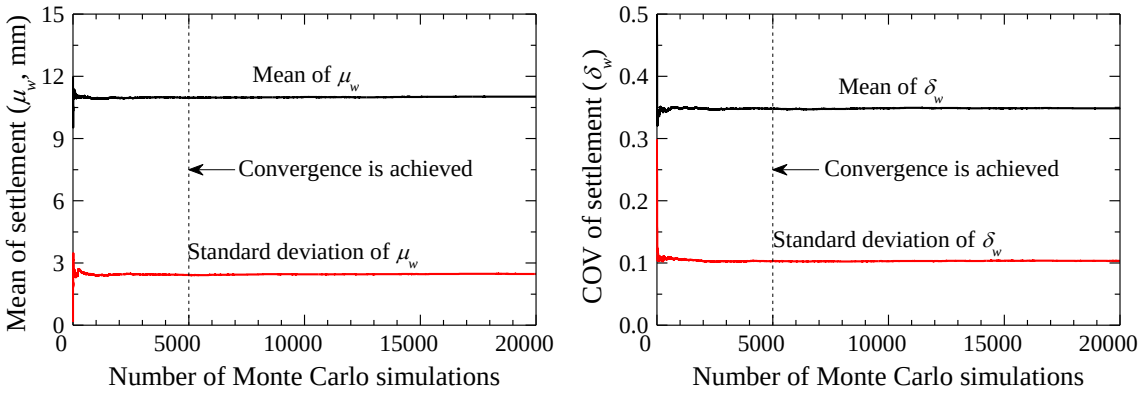

Figure 2.11: The convergence of tunnel settlement statistics: (a) Mean of tunnel settlement; (b) COV of tunnel settlement

Parametric study – how the tunnel settlements are affected by the spatial variation of soil properties and tunnel longitudinal flexural stiffness

Parametric study is carried out in this section to investigate how the tunnel settlement statistics (i.e., μ_w and δ_w), taken herein as the mean of tunnel settlement statistics within 5,000 MCS runs, are affected by the spatial variation of the subgrade reaction coefficient of the ground under the tunnel and the tunnel longitudinal flexural stiffness. For this parametric study, different combinations of the statistical parameters

(i.e., μ, δ, and r) of the random field of the subgrade reaction coefficient are employed to represent different spatial variations of soil properties, and different reduction factors of the tunnel longitudinal flexural stiffness (ζ) are used to represent different designs of the tunnel longitudinal flexural stiffness. The results of the parametric study are shown in Figure 2.12 and Figure 2.13.

Plotted in Figure 2.12 are the relationships between the tunnel settlement statistics and the statistical parameters of the random field of the subgrade reaction coefficient of the ground under the tunnel. As expected, the overall tunnel settlement tends to decrease with the improvement of the underlying ground stiffness, which is indicated by the increase of the mean of the subgrade reaction coefficient μ (see Figure 2.12a); whereas, the extent of tunnel differential settlement, reflected by the COV of tunnel settlement, is hardly influenced by the mean of the subgrade reaction coefficient (see Figure 2.12b). The overall tunnel settlement is slightly affected by the COV (δ) and the scale of fluctuation (r) of the subgrade reaction coefficient (see Figure 2.12c & 2.12e, respectively); whereas, the extent of tunnel differential settlement is significantly affected by the COV (δ) and the scale of fluctuation (r) of the subgrade reaction coefficient (see Figure 2.12d & 2.12f, respectively). As shown in Figure 2.12(d), the COV of tunnel settlement increases with the COV (δ) of the subgrade reaction coefficient. However, the relationship between the COV of tunnel settlement and the scale of fluctuation (r) of the subgrade reaction coefficient, as depicted in Figure 2.12(f), is not monotonic.

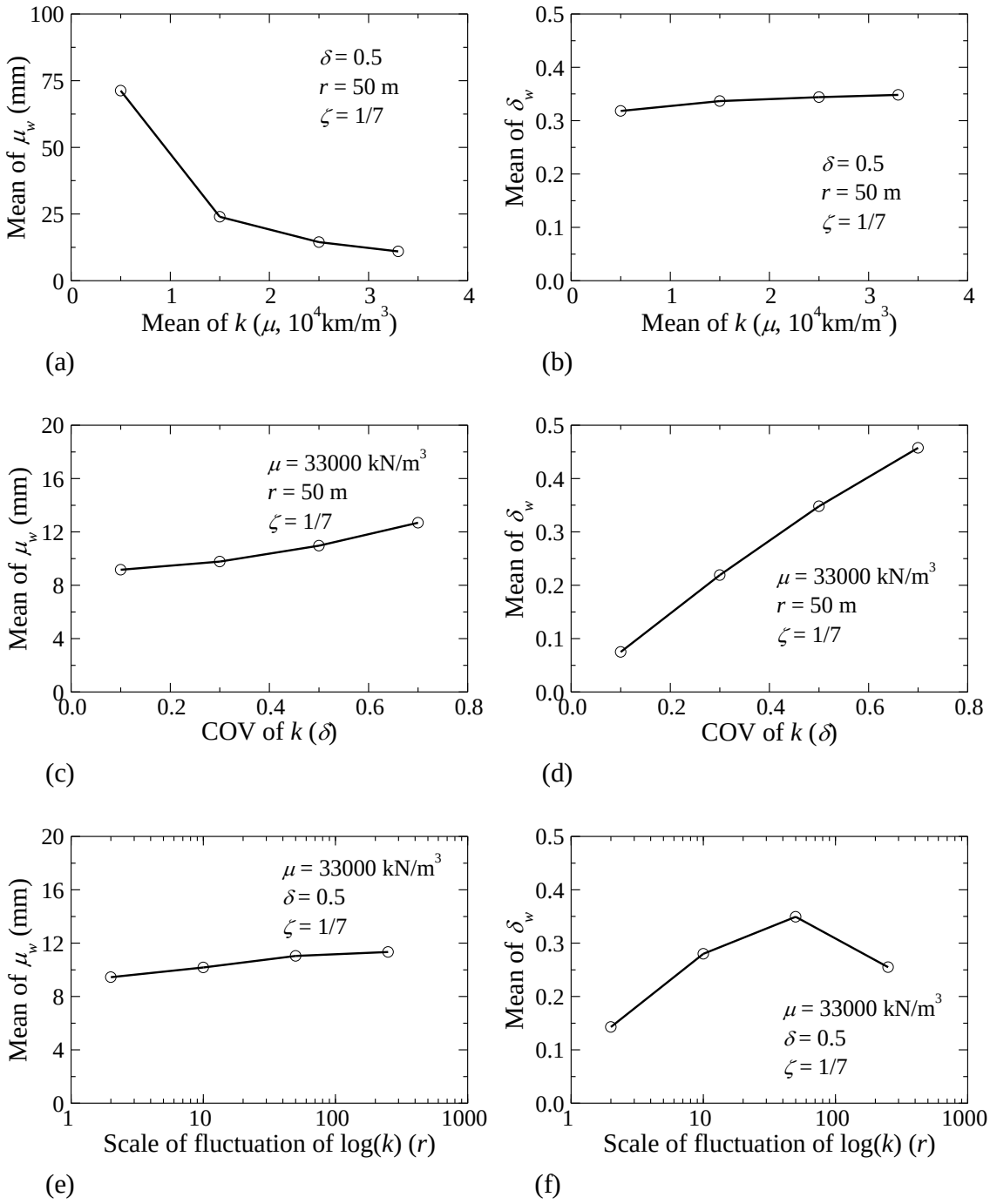

Figure 2.12: Mean of tunnel settlement statistics versus the spatial variation parameters: (a) Mean of μ_w versus μ; (b) Mean of δ_w versus μ; (c) Mean of μ_w versus δ; (d) Mean of δ_w versus δ; (e) Mean of μ_w versus r; (f) Mean of δ_w versus r

As noted in Figure 2.12(f), when the value of r is not large (i.e., less than 50 m), the increase of r can lead to the increase of the extent of tunnel differential settlement; otherwise, the increase of r can lead to the inverse effect on the extent of tunnel differential settlement. This non-monotonic relationship may be interpreted with the following observations. First, as seen in Eq. (2.21), a lower scale of fluctuation of the subgrade reaction coefficient implies a lower value of the variance reduction function $\gamma(l)$; thus, the averaging effect is more evident, which leads to a lower COV of tunnel settlement. Second, a larger scale of fluctuation of the subgrade reaction coefficient indicates a stronger correlation among the subgrade reaction coefficients of the ground under the tunnel, which also leads to a lower COV of tunnel settlement.

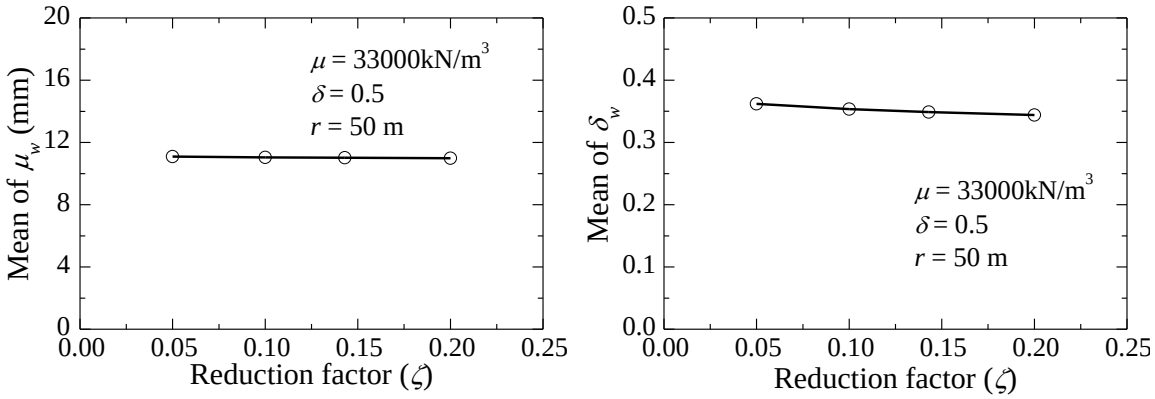

Figure 2.13: Mean of tunnel settlement statistics versus the reduction factor of tunnel longitudinal flexural stiffness: (a) Mean of μ_w versus ζ; (b) Mean of δ_w versus ζ

Similarly, the relationships between the tunnel settlement statistics and the tunnel longitudinal flexural stiffness (indicated by the reduction factor of tunnel longitudinal flexural stiffness ζ) are analyzed. The results shown in Figure 2.13 indicate that the

tunnel settlement statistics are slightly affected by the tunnel longitudinal flexural stiffness.

Summary

This chapter develops a simplified FEM procedure for the analysis of tunnel longitudinal performance that can explicitly consider the longitudinal variation of tunnel design parameters, such as the spatial variation (in the longitudinal domain) of soil properties of the ground under the tunnel. The developed FEM procedure or model for the tunnel longitudinal performance is verified by both analytical solutions and model tests. Further, the random field concept is employed to model the spatial variation (in the longitudinal domain) of soil properties, in terms of the subgrade reaction coefficient, of the ground under the tunnel. Finally, a parametric study is conducted to investigate how the longitudinal variation in the predicted tunnel settlement (referred to herein as tunnel settlement statistics) may be affected by different factors such as the spatial variability of soil properties and tunnel longitudinal flexural stiffness.

CHAPTER THREE
IMPROVED ANALYTICAL MODEL FOR CIRCUMFERENTIAL BEHAVIOR OF JOINTED SHIELD TUNNELS CONSIDERING THE LONGITUDINAL DIFFERENTIAL SETTLEMENT[*]

Introduction

The progress in advancing shield-driven machines and construction technologies has made shield tunneling one of the most popular methods used in the construction of urban tunnels, particularly for tunnels in soft soils. The segmental lining of these shield tunnels constructed with shield-driven machines is often designed with the assumption of a plane strain condition, a prerequisite that is valid when no variation of the design parameters (e.g., soil parameters, ground water level, and embedded depth, surcharge load) exists along the longitudinal direction (Wood 1975; ITA 2000; Lee et al. 2001; Koyama 2003). However, such a prerequisite may not always be satisfied; many factors such as the longitudinal variation of tunnel alignment, the spatial variability of soil properties, the differential consolidation of the ground, and the nearby underground construction (e.g., tunneling) can cause the longitudinal variation of tunnel design parameters. One significant consequence, caused by the longitudinal variation of design

---

[*] A similar form of this chapter has been accepted at the time of writing: Gong, W., Juang, C. H., Huang, H., Zhang, J., and Luo, Z. (2014). "Improved analytical model for circumferential behavior of jointed shield tunnels considering the longitudinal differential settlement." Tunnelling and Underground Space Technology, 45, 153-165.

parameters, is the differential settlement of shield tunnels (referred to herein as the vertical displacement of the tunnel structure), which is a serious event in soft soils. The Metro Line 1 in Shanghai, China is one such example, with the accumulated longitudinal settlement occurring over the past 15 years plotted in Figure 3.1, reached a maximum of 300 mm, and severe differential settlements were noted. In such a circumstance, the effect of tunnel longitudinal differential settlement on the circumferential behavior of segmental lining cannot be neglected.

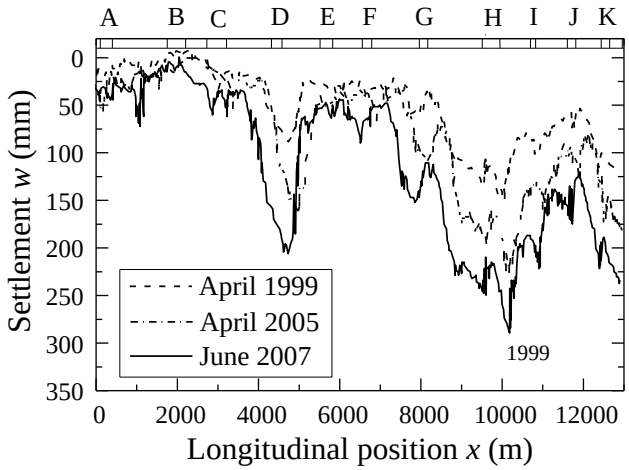

Figure 3.1: Accumulated longitudinal settlement of the Shanghai Metro Line 1 (Note: A – Caobao Road; B – Shanghai Indoor Stadium; C – Xujiahui; D – Hengshan Road; E – Changshu Road; F – South Shanxi Road; G – South Huangpi Road; H – People's Square; I – Xinzha Road; J – Hanzhong Road; K – Shanghai Railway Station)

Though it is widely acknowledged that the effect of tunnel longitudinal differential settlement on the circumferential behavior of segmental lining must be considered in the analysis and design of shield tunnels (ATRB 2000; ITA 2000), very few studies have been undertaken to elucidate this effect. Among these studies, Liao et al. (2005) developed a 1-D analytical model to analyze the effect of the longitudinal shear

force increment, arisen from the longitudinal differential settlement, on the tunnel cross section through the longitudinal shear transfer (LST) mechanism. This 1-D shearing effect model was subsequently extended to account for the 3-D behavior of shield tunnels by modeling the segmental lining with cylindrical shells (Liao et al. 2008). Later on, the effect of the longitudinal bending moment on the tunnel cross section, known as the flattening effect, was studied by Huang et al. (2012). While the shearing effect and the flattening effect were analyzed separately in the previous studies, these two effects should be modeled simultaneously to investigate how the circumferential behavior of segmental lining is affected by the longitudinal differential settlement of the tunnel. However, a tunnel analytical model to account for the effect of tunnel longitudinal differential settlement on the circumferential behavior of segment lining, including both the structure safety and serviceability, has not been developed. Furthermore, a framework for evaluating the longitudinal variation of the circumferential behavior of segment lining based upon the observed tunnel longitudinal differential settlement is needed.

Therefore, the objective of this paper is to develop an improved analytical model of jointed shield tunnels, which considers explicitly the effect of tunnel longitudinal differential settlement on the circumferential behavior of segmental lining. This paper is organized as follows. First, we describe an improved tunnel analytical model with explicit consideration of the longitudinal differential settlement, primarily through the shearing effect model and the flattening effect model. We next present an example to illustrate how the circumferential behavior of segmental lining varies along the longitudinal direction with a tunnel longitudinal settlement curve. Finally, we conduct

parametric analysis to investigate how the circumferential behavior of segmental lining is affected by different factors, including the effect of tunnel longitudinal differential settlement.

Improved Analytical Model for the Segmental Lining

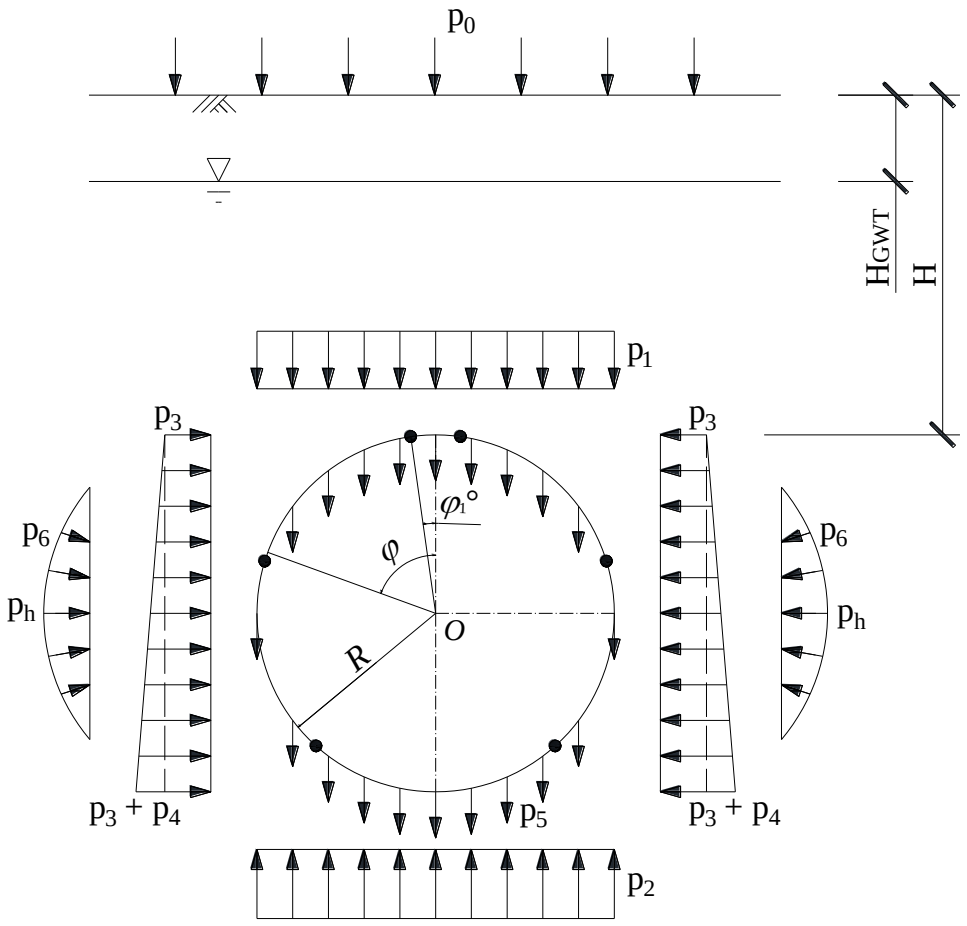

Figure 3.2: The circumferential loads on the cross section of jointed shield tunnels

In the current practice, the segmental lining of jointed shield tunnels is often designed based upon the results of analysis of a few typical tunnel cross sections assuming a plane strain condition (ITA 2000). For a typical tunnel cross section, as

plotted in Figure 3.2 and subjected to the circumferential loads, the internal forces and convergence deformation of segmental lining can readily be computed with the existing analysis methods such as that proposed by Lee et al. (2001). In this paper, the authors describe their simultaneous incorporation of the shearing effect (Liao et al. 2005) and the flattening effect (Huang et al. 2012) into the existing analytical model, for purpose of improving the model for the designing of jointed shield tunnels.

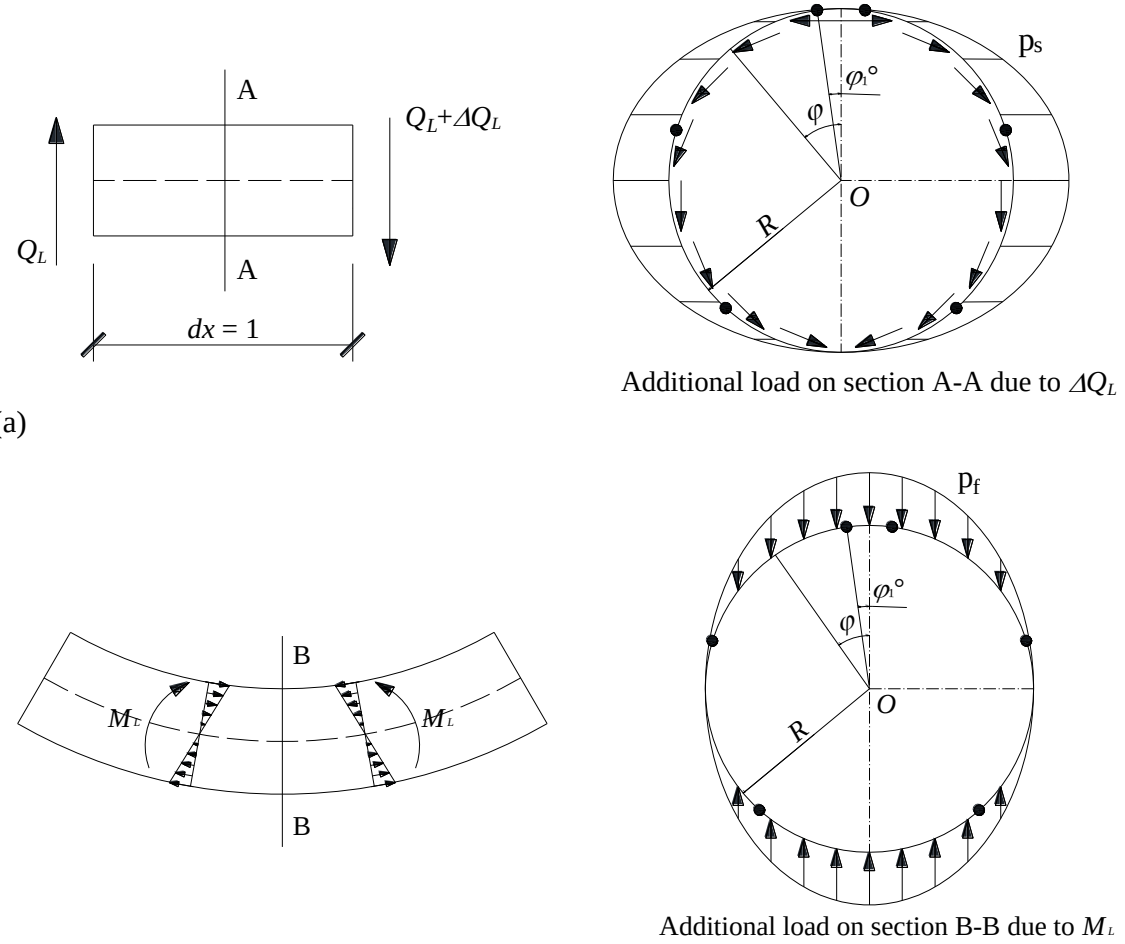

Figure 3.3: Additional loads on the tunnel cross section caused by tunnel longitudinal differential settlement: (a) Shearing effect; (b) Flattening effect

Shearing effect model and flattening effect model

In the subsequent analysis of tunnel *longitudinal* performance, the following sign conventions are adopted: the settlement is assumed as positive when it moves downward; the longitudinal bending moment is treated as positive when the tunnel invert would be subjected to the longitudinal tension; and the longitudinal shear force is regarded as positive when it exhibits a clockwise rotation. As mentioned above, the effect of tunnel longitudinal differential settlement on the circumferential behavior of segmental lining can be modeled by considering the shearing effect and the flattening effect, both of which are represented with the additional loads on the tunnel cross section, as shown in Figure 3.3. According to Liao et al. (2005), the additional load on the tunnel cross section from the shearing effect (p_s) is expressed as (see Figure 3.3a):

$$p_s = \frac{R^2 t \sin\varphi}{I_L} \Delta Q_L \tag{3.1}$$

where R is the radius of the segmental lining, taken as the average of the outer radius (R_o) and inner radius (R_i); t is the thickness of segmental lining; φ is the circumferential angle measured from the tunnel crown; ΔQ_L is the longitudinal shear force increment per unit length caused by the longitudinal differential settlement; and I_L is the inertia moment of the tunnel cross section in the longitudinal performance analysis, defined as:

$$I_L = \frac{\pi}{4}[(R+\frac{t}{2})^4 - (R-\frac{t}{2})^4] \tag{3.2}$$

The additional load on the tunnel cross section from the flattening effect (p_f) is expressed as (see Figure 3.3b; Huang et al. 2012):

$$p_f = \frac{M_L}{I_L} \kappa R t \cos\varphi \tag{3.3}$$

where M_L is the longitudinal moment of the shield tunnel caused by the longitudinal differential settlement, and κ is the curvature of the tunnel longitudinal settlement.

For simplicity, the longitudinal structure of the jointed shield tunnel is usually approximated as a slender elastic beam in the context of tunnel longitudinal performance analysis (Shiwa et al. 1986; Talmon and Bezuijen 2013), while the soil-structure interaction is modeled with Winkler (1867), Pasternak (1954), or Kerr (1965) model. In context of the elastic beam, M_L in Eq. (3.3) and ΔQ_L in Eq. (3.1) are computed respectively with the observed tunnel longitudinal settlement (w) as follows:

$$M_L = (\zeta E I_L)\,\kappa \tag{3.4}$$

$$\frac{dQ_L}{dx} = \frac{d^2 M_L}{dx^2} \approx (\zeta E I_L) \frac{d^4 w}{dx^4} \tag{3.5}$$

where ζ is the reduction factor of tunnel longitudinal flexural stiffness, which is often used to scale the effect of the longitudinal joints on the tunnel longitudinal flexural stiffness (Liao et al. 2008); E is the elastic modulus of segmental lining; κ is the curvature of the monitored tunnel longitudinal settlement (w); and x is the longitudinal

coordinate. Note that the term ΔQ_L in Eq. (3.1) is easily computed from Eq. (3.5) as: $\Delta Q_L = \frac{dQ_L}{dx} \times dx\big|_{dx=1} = \frac{dQ_L}{dx}$.

Force-method equations of jointed shield tunnel

The segmental lining of a jointed shield tunnel is generally a redundant structure that is subjected to both the circumferential loads that defined in Lee and Ge (2001) (see Figure 3.2) and the additional loads caused by tunnel longitudinal differential settlement (see Figure 3.3). Here, the force method is employed to determine the internal forces and convergence deformation of the segmental lining. The following sign conventions are adopted in the subsequent derivation of the *circumferential* behavior of the segmental lining: the bending moment is taken as positive when the lining's inside surface is subjected to tension; the axial force is taken as positive when the segmental lining is subjected to compression; and the shear force is treated as positive when it yields a clockwise rotation.

As illustrated in Figure 3.4(a), the force method equations of the half tunnel structure can be established by considering zero rotation and zero horizontal displacement at the tunnel crown and the tunnel invert, as follows (Lee et al. 2001):

$$\delta_{11}x_1 + \delta_{12}x_2 + \Delta_{1p} = 0 \tag{3.6a}$$

$$\delta_{21}x_1 + \delta_{22}x_2 + \Delta_{2p} = 0 \tag{3.6b}$$

where x_1 and x_2 are the bending moment and axial force (per unit length) acting at the tunnel crown, respectively, which are redundant forces; δ_{ij} is the displacement developed at the location of redundant force x_i and along the direction of x_i due to the action of unit force $x_j = 1$ (i = 1, 2 and j = 1, 2); and, Δ_{ip} is the displacement developed at the location of redundant force x_i and along the direction of x_i due to the circumferential loads plotted in Figure 3.2 and the additional loads caused by tunnel longitudinal differential settlement (see Figure 3.3)

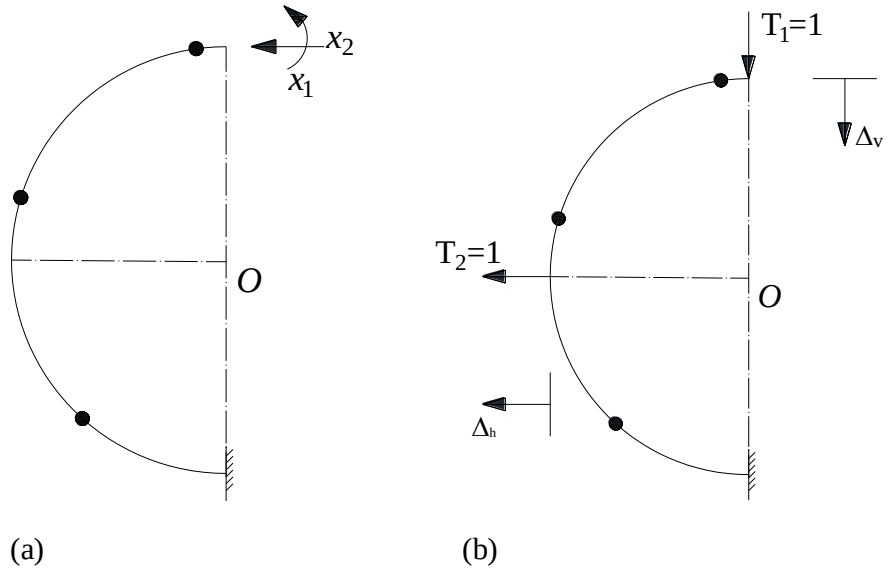

Figure 3.4: Force method derivation of the half tunnel structure: (a) Redundant forces of the half tunnel structure; (b) Virtual forces for calculating the convergence deformation

Solving Eq. (3.6) in terms of x_1 and x_2 results in:

$$x_1 = \frac{\delta_{12}\Delta_{2p} - \delta_{22}\Delta_{1p}}{\delta_{11}\delta_{22} - \delta_{12}\delta_{21}} \tag{3.7a}$$

$$x_2 = \frac{\delta_{21}\Delta_{1p} - \delta_{11}\Delta_{2p}}{\delta_{11}\delta_{22} - \delta_{12}\delta_{21}} \tag{3.7b}$$

Since the effects of the axial force and the shear force on the displacement calculation are relatively small, only the bending moment is considered herein (Lee et al. 2001). Based upon the force method equations of Lee et al. (2001), δ_{11}, δ_{12} (δ_{21}), and δ_{22} are presented as:

$$\delta_{11} = \frac{R\pi}{EI} + \sum_{i=1}^{n} \frac{1}{K_\theta^{(i)}} \tag{3.8a}$$

$$\delta_{12}(\delta_{21}) = \frac{R^2\pi}{EI} + R\sum_{i=1}^{n} \frac{1}{K_\theta^{(i)}}\left(1 - \cos\varphi_i\right) \tag{3.8b}$$

$$\delta_{22} = \frac{3R^3\pi}{2EI} + R^2\sum_{i=1}^{n} \frac{1}{K_\theta^{(i)}}\left(1 - \cos\varphi_i\right) \tag{3.8c}$$

where $K_\theta^{(i)}$ is the flexural stiffness of i^{th} circumferential joint; φ_i is the circumferential angle of i^{th} circumferential joint measured from the tunnel crown; n is the number of joints of the half tunnel structure; and I is the inertia moment of segmental lining in the circumferential behavior analysis, which is calculated as: $I = t^3 / 12$ (per unit length). The terms Δ_{1p} and Δ_{2p} in Eq. (3.6) & (3.7) can be computed as follows, respectively:

$$\Delta_{1p} = \sum_{j=1}^{6} \Delta_{1pj} + \Delta_{1ps} + \Delta_{1pf} \tag{3.9a}$$

$$\Delta_{2p} = \sum_{j=1}^{6} \Delta_{2pj} + \Delta_{2ps} + \Delta_{2pf} \tag{3.9b}$$

where the displacements due to the circumferential loads plotted in Figure 3.2, in terms of Δ_{1pj} and Δ_{2pj} (j = 1, 2, 3, 4, 5, 6), are readily available from Lee et al. (2001); and the displacements due to the additional loads caused by tunnel longitudinal differential settlement (see Figure 3.3), in terms of Δ_{1ps}, Δ_{1pf}, Δ_{2ps}, and Δ_{2pf}, are derived in this paper with virtual work theory, the results are presented as follows:

$$\Delta_{1ps} = \frac{\pi}{2}\frac{\Delta Q_L R^4 t}{EI_L I} + \frac{\Delta Q_L R^4 t}{I_L}\sum_{i=1}^{n}\frac{(1-\cos\varphi_i - \frac{\varphi_i}{2}\sin\varphi_i)}{K_\theta^{(i)}} \tag{3.10a}$$

$$\Delta_{1pf} = -\frac{\pi}{4}\frac{M_L \kappa R^3 t}{EI_L I} - \frac{1}{2}\frac{M_L \kappa R^3 t}{I_L}\sum_{i=1}^{n}\frac{\sin^2\varphi_i}{K_\theta^{(i)}} \tag{3.10b}$$

$$\Delta_{2ps} = \frac{7\pi}{8}\frac{\Delta Q_L R^5 t}{EI_L I} + \frac{\Delta Q_L R^5 t}{I_L}\sum_{i=1}^{n}\frac{(1-\cos\varphi_i - \frac{\varphi_i}{2}\sin\varphi_i)(1-\cos\varphi_i)}{K_\theta^{(i)}} \tag{3.10c}$$

$$\Delta_{2pf} = -\frac{\pi}{4}\frac{M_L \kappa R^4 t}{EI_L I} - \frac{1}{2}\frac{M_L \kappa R^4 t}{I_L}\sum_{i=1}^{n}\frac{\sin^2\varphi_i(1-\cos\varphi_i)}{K_\theta^{(i)}} \tag{3.10d}$$

Based upon the computed coefficients of δ_{11}, δ_{12} (δ_{21}), δ_{22}, Δ_{1p}, and Δ_{2p}, the redundant forces x_1 and x_2 can be solved with Eq. (3.7). The corresponding internal forces, including the bending moment M, and shear force Q, and axial force N, of the segmental lining (per unit length) can then be computed with the following equations:

$$M = \overline{M_1}x_1 + \overline{M_2}x_2 + \sum_{j=1}^{6} M_{pj} + M_s + M_f \tag{3.11a}$$

$$Q = \overline{Q_1}x_1 + \overline{Q_2}x_2 + \sum_{j=1}^{6} Q_{pj} + Q_s + Q_f \tag{3.11b}$$

$$N = \overline{N_1}x_1 + \overline{N_2}x_2 + \sum_{j=1}^{6} N_{pj} + N_s + N_f \tag{3.11c}$$

where $\overline{M_i}$, $\overline{Q_i}$, and $\overline{N_i}$ (i =1, 2) are the bending moment, shear force, and axial force of the segmental lining due to the virtual unit force of x_i = 1 acting at the tunnel crown (see Figure 3.4a), respectively; M_{pj}, Q_{pj} and N_{pj} (j =1, 2, 3, 4, 5, 6) are the bending moment, shear force, and axial force of the segmental lining due to the circumferential loads plotted in Figure 3.2, respectively; M_s, Q_s, and N_s are the bending moment, shear force, and axial force of segmental lining due to the additional load on the tunnel cross section caused by the shearing effect, respectively; and, M_f, Q_f, and N_f are the bending moment, shear force, and axial force of the segmental lining due to the additional load on the tunnel cross section caused by the flattening effect, respectively. Note that $\overline{M_i}$, $\overline{N_i}$, $\overline{Q_i}$, M_{pj}, N_{pj} and Q_{pj} (i =1, 2 and j =1, 2, 3, 4, 5, 6) are readily available with the solution of Lee et al. (2001), while M_s, N_s, Q_s, M_f, N_f, and Q_f are derived in this paper as follows:

$$M_s = \frac{\Delta Q_L R^4 t}{I_L}\left(1 - \cos\varphi - \frac{\varphi}{2}\sin\varphi\right) \tag{3.12a}$$

$$N_{\mathrm{s}} = \frac{\Delta Q_L R^3 t}{I_L} \frac{\varphi}{2} \sin\varphi \tag{3.12b}$$

$$Q_{\mathrm{s}} = -\frac{\Delta Q_L R^3 t}{I_L} \left(\frac{\sin\varphi}{2} - \frac{\varphi}{2}\cos\varphi\right) \tag{3.12c}$$

$$M_{\mathrm{f}} = -\frac{1}{2} \frac{M_L \kappa R^3 t \sin^2\varphi}{I_L} \tag{3.13a}$$

$$N_{\mathrm{f}} = \frac{M_L \kappa R^2 t \sin^2\varphi}{I_L} \tag{3.13b}$$

$$Q_{\mathrm{f}} = \frac{M_L \kappa R^2 t \sin\varphi\cos\varphi}{I_L} \tag{3.13c}$$

Furthermore, the convergence deformation of the segmental lining, such as the vertical deformation at the tunnel crown (Δ_{v}) and the horizontal deformation at the tunnel springline (Δ_{h}), can be calculated with virtual work theory (see Figure 3.4b) as follows:

$$\Delta_{\mathrm{v}} = \Delta_{\mathrm{v1}} + \Delta_{\mathrm{v2}} + \sum_{j=1}^{6} \Delta_{\mathrm{vp}j} + \Delta_{\mathrm{vs}} + \Delta_{\mathrm{vf}} \tag{3.14a}$$

$$\Delta_{\mathrm{h}} = \Delta_{\mathrm{h1}} + \Delta_{\mathrm{h2}} + \sum_{j=1}^{6} \Delta_{\mathrm{hp}j} + \Delta_{\mathrm{hs}} + \Delta_{\mathrm{hf}} \tag{3.14b}$$

where $\Delta_{\mathrm{v}i}$ and $\Delta_{\mathrm{h}i}$ (i = 1, 2) are the vertical displacement at the tunnel crown and the horizontal displacement at the tunnel springline, respectively, due to the redundant force

x_i acting at the tunnel crown; Δ_{vpj} and Δ_{hpj} (j =1, 2, 3, 4, 5, 6) are the vertical displacement at the tunnel crown and the horizontal displacement at the tunnel springline, respectively, due to the circumferential loads plotted in Figure 3.2; Δ_{vs} and Δ_{hs} are the vertical displacement at the tunnel crown and the horizontal displacement at the tunnel springline, respectively, due to the additional load on the tunnel cross section caused by the shearing effect; Δ_{vf} and Δ_{hf} are the vertical displacement at the tunnel crown and the horizontal displacement at the tunnel springline, respectively, due to the additional load on the tunnel cross section caused by the flattening effect. Note that Δ_{vi}, Δ_{hi}, Δ_{vpj}, and Δ_{hpj} (i =1, 2 and j =1, 2, 3, 4, 5, 6) are readily available with the solution of Lee et al. (2001), while Δ_{vs}, Δ_{hs}, Δ_{vf}, and Δ_{hf} are derived in this paper and presented as follows:

$$\Delta_{vs} = -\frac{16-\pi^2}{8}\frac{\Delta Q_L R^5 t}{EI_L I} - \frac{\Delta Q_L R^5 t}{I_L}\sum_{i=1}^{n}\frac{(1-\cos\varphi_i - \frac{\varphi_i}{2}\sin\varphi_i)\sin\varphi_i}{K_\theta^{(i)}} \tag{3.15a}$$

$$\Delta_{hs} = \frac{16+\pi}{16}\frac{\Delta Q_L R^5 t}{EI_L I} - \frac{\Delta Q_L R^5 t}{I_L}\sum_{i=n_1+n_2+1}^{n}\frac{(1-\cos\varphi_i - \frac{\varphi_i}{2}\sin\varphi_i)\cos\varphi_i}{K_\theta^{(i)}} \tag{3.15b}$$

$$\Delta_{vf} = \frac{2}{3}\frac{M_L \kappa R^4 t}{EI_L I} + \frac{1}{2}\frac{M_L \kappa R^4 t}{I_L}\sum_{i=1}^{n}\frac{\sin^3\varphi_i}{K_\theta^{(i)}} \tag{3.16a}$$

$$\Delta_{hf} = -\frac{1}{6}\frac{M_L \kappa R^4 t}{EI_L I} + \frac{1}{2}\frac{M_L \kappa R^4 t}{I_L}\sum_{i=n_1+n_2+1}^{n}\frac{\sin^2\varphi_i\cos\varphi_i}{K_\theta^{(i)}} \tag{3.16b}$$

where n_1 and n_2 are the number of circumferential joints within the region of $0 \leq \varphi < 45°$ and $45° \leq \varphi < 90°$, respectively.

Compared to the existing analytical models, the *proposed* analytical model of jointed shield tunnels, formulated in this section, is a more comprehensive examination of the effect of tunnel longitudinal differential settlement on the circumferential behavior of segmental lining. The resulting internal forces and convergence of the tunnel cross section of concern are readily applicable for assessing the circumferential behavior of tunnel segmental lining, including both the structure safety and serviceability. For simplicity, the authors did not consider the bearing capacity of segmental joints (Teachavorasinskun and Chub-uppakarn 2010) and the contact deficiency of the segmental lining (Cavalaro et al. 2011) in this assessment of the circumferential behavior of the segmental lining.

Assessment of the circumferential behavior of segmental linings

Structure safety of the segmental lining

To account for the plastic behavior of the reinforced segmental lining, the limit state design method is used to assess the structure safety of the segmental lining (ITA 2000; Gong et al. 2014b). Here, the structural failure of the segmental lining is hypothesized to occur only when the combined internal forces of the bending moment and the axial force, in terms of (M, N), exceeds the corresponding limit state, in terms of (M_{ult}, N_{ult}), on the ultimate bearing capacity envelope of the reinforced segmental lining, as demonstrated in Figure 3.5. Note that the ultimate bearing capacity envelope of the reinforced segmental lining can be derived using the plasticity theory of reinforced

concrete. For simplicity, an assumption is made here that the eccentricity of tunnel internal forces, in terms of (M/N), is a constant. As such, in a deterministic approach, the factor of safety with respect to the structure safety of the segmental lining, denoted as Fs_1, can be computed as:

$$Fs_1 = \frac{\sqrt{N_{ult}{}^2 + M_{ult}{}^2}}{\sqrt{N^2 + M^2}} \tag{3.17}$$

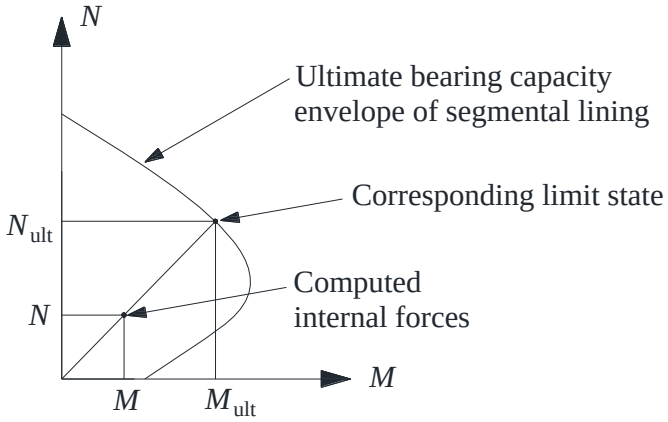

Figure 3.5: Structure safety assessment of the segmental lining using limit state design method

As the value of Fs_1 can vary with the circumferential position within the segmental ring of concern, the structure safety of the segmental lining would only be governed by the position with the minimum value of Fs_1, rather than the section of either the maximum bending moment or the maximum axial force that is adopted in ITA (2000). However, such a critical position might change with the input parameters; in such a circumstance, the minimum value of Fs_1 is sought along the circumferential direction each time as the input parameters vary in the subsequent analysis.

Even though the structure safety of the segmental lining is also affected by the computed shear force (Q), the effect of that force on the structure safety is relatively small and thus its effect is negligible (ITA 2000; Gong et al. 2014b). If desired, the structure safety of the segmental lining can be analyzed using the stress theory, in which all the internal forces resulting from the circumferential behavior analysis (i.e., axial force N, shear force Q, bending moment M) and that obtained from the longitudinal behavior analysis (i.e., longitudinal axial forces N_L, longitudinal shear force Q_L, and longitudinal bending moment M_L) are considered simultaneously. Such a study, however, is beyond the scope of this paper.

Serviceability of the segmental lining

The computed tunnel convergence deformation is used to evaluate the serviceability of the segmental lining, since the tunnel performance problems such as leakage and concrete cracking are always associated with the excessive convergence deformation. As specified in the Chinese metro code (MCPRC 2003), the maximum convergence deformation of shield tunnels must be controlled below 0.4%D to 0.6%D (D denotes the outer diameter of segmental lining). For ease of illustration, in a deterministic approach, the factor of safety against the serviceability problem of the segmental lining, denoted as Fs_2, is formulated as:

$$Fs_2 = \frac{0.6\%D}{\max(\Delta_v, 2\Delta_h)} \tag{3.18}$$

Illustrative Example

The performance of an existing tunnel is often significantly affected by the nearby tunneling; field data in Shanghai show that such disturbances may result in a Gaussian longitudinal settlement curve of the existing tunnel (Liao 2002; Liao et al. 2008; Huang 2012). Indeed, the Gaussian settlement curve is often used to model the ground deformation caused by the nearby tunneling (Verruijt and Booker 1996; Loganathan and Poulos 1998; Gonzalez and Sagaseta 2001; Park 2005; Toraño et al. 2006). In general, because the tunnel and the surrounding ground would deform consistently, the settlement of the exiting tunnel is also represented with a Gaussian settlement curve. The main objective of the present study is to analyze the longitudinal variation of the circumferential behavior of segmental lining given a tunnel settlement curve. Here, the authors investigate how the circumferential behavior of the segmental lining, including both the structure safety and serviceability, varies along the longitudinal direction, given a Gaussian longitudinal settlement curve.

Parameters settings

Basic design parameters of this illustrative example are listed in Table 3.1. From these data, the circumferential loads plotted in Figure 3.2 can readily be evaluated, which are then used to compute the internal forces (i.e., *M*, *N*, and *Q*) and the convergence deformation (i.e., Δ_v and $2\Delta_h$) of the segmental lining using the existing tunnel analysis methods such as that proposed by Lee at al. (2001). Further, the ultimate bearing capacity envelope of the reinforced concrete lining shown in Figure 3.5 is obtained with the material parameters that are listed in Table 3.2.

Table 3.1: Design parameters of the illustrative example

Parameter	Value
Tunnel outer radius R_o (m)	5.5
Segment thickness t (m)	0.55
Segment width b (m)	1.0
Embedded depth H (m)	18.7
Ground water table H_{GWT} (m)	0.0
Unit weight of soil γ (kN/m^3)	18.0
Unit weight of water γ_w (kN/m^3)	9.8
Soil cohesion c (kPa)	17.0
Soil friction angle ϕ (°)	18.5
Soil resistance coefficient Ks (kN/m^3)	15,000
Joint number of each tunnel ring	8
Joint position of half structure φ_i (°)	22.5, 67.5, 112.5, 157.5
Circumferential joint stiffness ratio k_θ[a]	0.14
Surcharge load p_0 (kPa)	0.0
Elastic modulus of concrete E (kN/m^2)	34.5×10^6
Unit weight of concrete γ_c (kN/m^3)	25.0

[a]The Circumferential joint stiffness ratio is defined as $k_\theta = \frac{K_\theta}{EI}$, where K_θ is the flexural stiffness of the circumferential joint and EI is the flexural stiffness of the tunnel segment in tunnel circumferential analysis.

Table 3.2: Parameters for assessing the ultimate bearing capacity envelope of reinforced concrete lining

Parameter	Value
Compression strength of concrete f_c (kN/m^2)	39.0×10^3
Tension strength of concrete f_t (kN/m^2)	3.87×10^3
Elastic modulus of steel bar E_s (kN/m^2)	210×10^6
Yielding strength of steel bar f_y (kN/m^2)	345×10^3
Thickness of concrete cover for steel bar a (m)	0.05
Steel reinforcement ratio at one side of segment lining ρ_s (%)	1.0

In this example, the following Gaussian curve is employed to represent the tunnel longitudinal settlement:

$$w(x) = S_{max} e^{-\frac{x^2}{2i^2}} \tag{3.19}$$

where S_{max} is the maximum settlement of the tunnel; i is the distance measured from the inflection point to the point with maximum settlement; and, x is the longitudinal coordinate measured from the position with the maximum settlement. For the given Gaussian settlement curve in Eq. (3.19), the curvature (κ) and fourth derivative ($w^{(4)}$) of the tunnel longitudinal settlement are readily derived as follows:

$$\kappa = \left| \left[(-\frac{S_{max}}{i^2} + \frac{x^2 S_{max}}{i^4}) e^{-\frac{x^2}{2i^2}} \right] \Big/ \left(1 + \frac{x^2 S_{max}^2}{i^4} e^{-\frac{x^2}{i^2}} \right)^{3/2} \right| \tag{3.20a}$$

$$w^{(4)} = \frac{S_{max} e^{-\frac{x^2}{2i^2}}}{i^4} (3 - \frac{6x^2}{i^2} + \frac{x^4}{i^4}) \tag{3.20b}$$

For the purpose of illustration, the maximum settlement (S_{max}) and the distance measured from the inflection point to the point with maximum settlement (i) in this example are taken as 300 mm and 50 m, respectively. Note that the reduction factor of tunnel longitudinal flexural stiffness (ζ) is taken here as 1/7 to consider the reduction effect of the longitudinal joints on the tunnel longitudinal flexural stiffness (Liao et al. 2008).

While it is acknowledged that both the stress field and stain field of the ground can be changed due to any nearby tunneling, for simplicity, such potential changes in the circumferential loads are not considered in our analysis. Further, the potential longitudinal variation of these circumferential loads is not considered in the subsequent

analysis of the longitudinal variation of the circumferential behavior of the segmental lining using the proposed tunnel analytical model presented herein.

Internal forces and convergence deformation of segmental lining

For the given tunnel longitudinal settlement shown in Figure 3.6(a), the longitudinal moment (M_L) and the longitudinal shear force increment per unit length (ΔQ_L) can readily be computed using the aforementioned formulations, and the results of which are plotted in Figure 3.6(b) and 3.6(c), respectively. As expected, both the longitudinal moment and the longitudinal shear force increment (per unit length) vary along the longitudinal direction; the longitudinal position with the maximum settlement (i.e., x = 0 m) exhibits the largest longitudinal moment and the lowest longitudinal shear force increment. Consequently, the effect of tunnel longitudinal settlement on the circumferential behavior of the segmental lining, primarily through the flattening effect and shearing effect, varies longitudinally.

According to the computed longitudinal moment (M_L) and the longitudinal shear force increment per unit length (ΔQ_L) shown in Figure 3.6(b) and 3.6(c), respectively, the additional loads caused by tunnel longitudinal differential settlement (see Figure 3.3) can be evaluated. These additional loads together with the circumferential loads plotted in Figure 3.2 are readily used to analyze the internal forces (i.e., M, N, and Q) and the convergence deformation (i.e., Δ_v and $2\Delta_h$) of the segmental lining using the proposed tunnel analytical model. Figure 3.7 shows the computed internal forces of segment lining

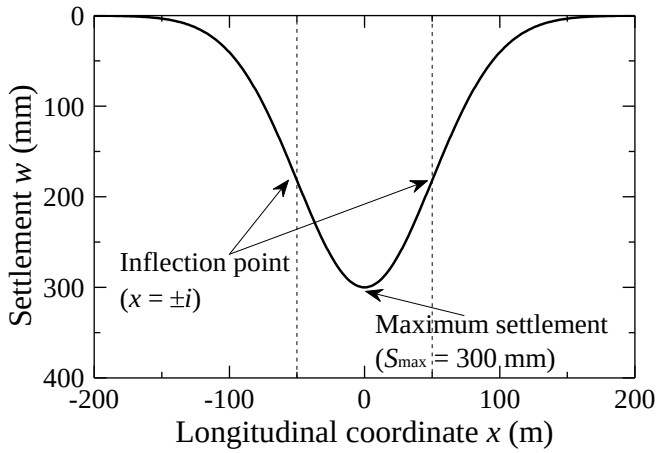
Settlement w (mm)
0
100
200
300
400
Inflection point
($x = \pm i$)
Maximum settlement
(S_{max} = 300 mm)
-200
-100
0
100
200
Longitudinal coordinate x (m)

(a)

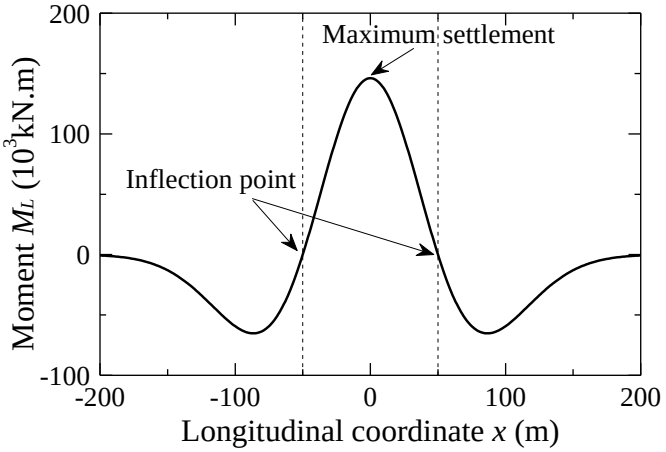
Moment M_L (10^3kN.m)
200
100
0
-100
Maximum settlement
Inflection point
-200
-100
0
100
200
Longitudinal coordinate x (m)

(b)

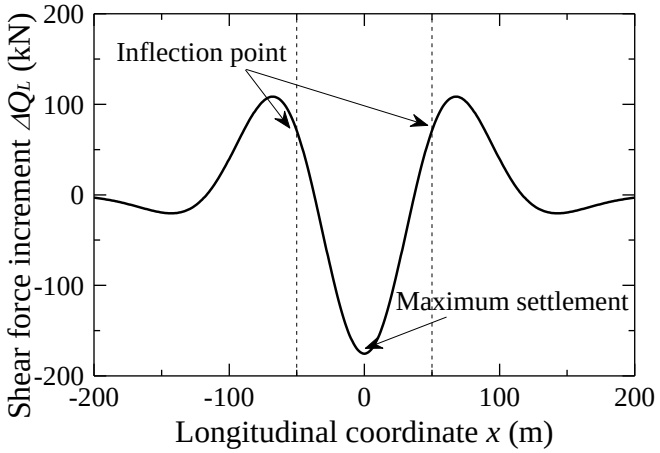
Shear force increment ΔQ_L (kN)
200
100
0
-100
-200
Inflection point
Maximum settlement
-200
-100
0
100
200
Longitudinal coordinate x (m)

(c)

Figure 3.6: Tunnel longitudinal behavior with Gaussian longitudinal settlement: (a) Tunnel settlement; (b) Tunnel longitudinal moment; (c) Tunnel longitudinal shear force increment (per unit length)

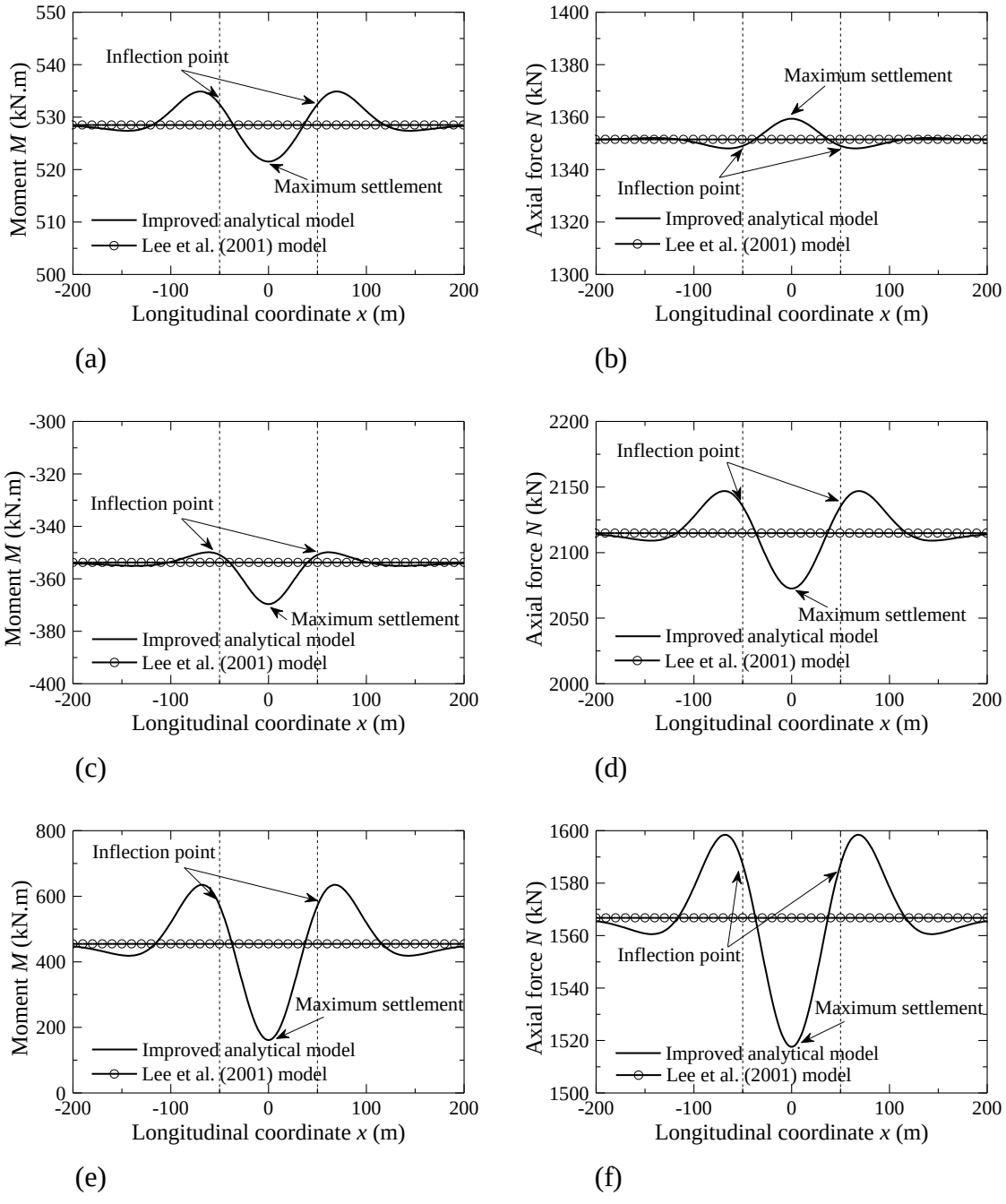

Figure 3.7: The longitudinal variation of the internal forces of segmental lining with Gaussian longitudinal settlement: (a) Bending moment at the tunnel crown; (b) Axial

force at the tunnel crown; (c) Bending moment at the tunnel spring; (d) Axial force at the tunnel spring; (e) Bending moment at the tunnel invert; (f) Axial force at the tunnel invert

at the tunnel crown, tunnel spring, and tunnel invert along the longitudinal direction. Also plotted in Figure 3.7 are the internal forces of segmental lining without considering the additional loads caused by the tunnel longitudinal differential settlement. The value of the shear force (Q) at the tunnel crown, tunnel spring, and tunnel invert of the segmental lining is relatively small however, and is not considered.

As can be seen in Figure 3.7, the internal forces of the segmental lining vary significantly with the longitudinal domain. The longitudinal position with the maximum settlement (i.e., x = 0 m) exhibits the lowest bending moment of the segmental lining at both tunnel crown (see Figure 3.7a) and tunnel invert (see Figure 3.7e). However, such a position with the maximum settlement exhibits the largest bending moment of the segmental lining at the tunnel spring (see Figure 3.7c). Similarly, the largest axial force at the tunnel crown is observed at the position with the maximum settlement (i.e., x = 0 m) (see Figure 3.7b), while the lowest axial forces at both the tunnel spring and the tunnel invert are detected with a position of the maximum settlement (see Figure 3.7d and 3.7f). However, this vital feature, referred to herein as the longitudinal variation of the internal forces of the segmental lining, cannot be reflected with the exiting tunnel analysis models that do not consider the effect of the tunnel longitudinal settlement. For example, the bending moment (M) at the tunnel invert varies from the lowest value of 161.3 kN.m to the largest value of 634.9 kN.m (along the longitudinal direction) with an explicit consideration of the tunnel longitudinal settlement. On the contrary, the value is kept as a

constant value of 452.7 kN.m when the effect of the tunnel longitudinal settlement is not considered.

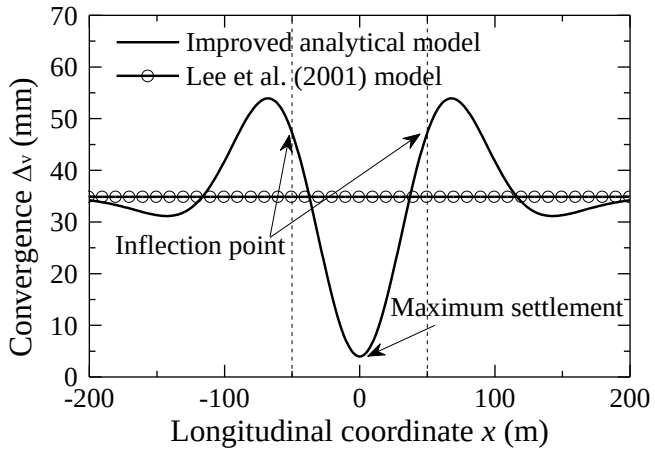

(a)

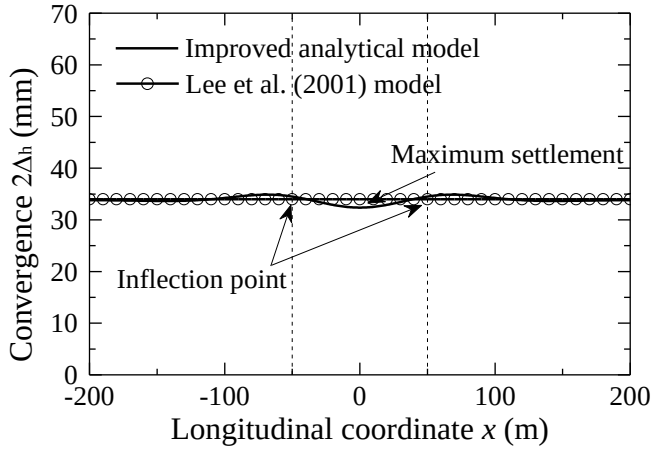

(b)

Figure 3.8: The longitudinal variation of the convergence deformation of the segmental lining with Gaussian longitudinal settlement: (a) Convergence deformation in the vertical direction; (b) Convergence deformation in the horizontal direction

The obtained longitudinal variation of the convergence deformation of segmental lining is plotted in Figure 3.8. As noted, the convergence deformation of the segmental lining in the vertical direction (Δ_v) varies from the lowest value of 4.0 mm to the largest

value of 53.9 mm (along the longitudinal direction) when the tunnel longitudinal settlement is considered; the convergence deformation is a constant (34.8 mm) when the tunnel longitudinal settlement is not considered. This longitudinal variation of the convergence deformation of the segmental lining in the horizontal direction ($2\Delta_h$) is, however, not distinct, as shown in Figure 3.8(b). The inconsistency in the longitudinal variation of the convergence deformation of segmental lining may be attributed to the fact that the convergence deformation of the lining in the horizontal direction is restricted by the surrounding ground, while in the vertical direction, it is not restricted and can deform freely.

Structure safety and serviceability of segmental lining

Furthermore, the longitudinal variation of both the structure safety and serviceability of the segmental lining is assessed with the proposed tunnel analytical model. Plotted in Figure 3.9(a) and 3.9(b) are the resulted longitudinal variations of the factor of safety with respect to the structure safety (Fs_1, see Eq. 3.17) and serviceability (Fs_2, see Eq. 3.18) of the segmental lining, respectively. The structure safety and serviceability of the segmental lining obtained with the existing tunnel analysis methods, in which the effect of the tunnel longitudinal settlement is not considered, are also plotted in Figure 3.9(a) and 3.9(b), respectively. As expected, no longitudinal variation of either the structure safety or serviceability are obtained with the existing analysis methods.

When the tunnel longitudinal settlement is considered, the structure safety of the segmental lining is slightly enhanced within the region between $x = -0.7i$ (or -35 m) and $x = 0.7i$ (or 35 m), for example, Fs_1 is increased from 3.56 to 3.65; however, the structure

safety is significantly reduced in the regions that range from x = -1.8i (or -90 m) to x = -0.7i (or -35 m) and from x = 0.7i (or 35 m) to x = 1.8i (or 90 m) (see Figure 3.9a). Also, the serviceability of the segmental lining is slightly enhanced in the region between x = -0.7i (or -35 m) and x = 0.7i (or 35 m), for example, Fs_2 is increased from 1.90 to 2.04; whereas, the serviceability is significantly reduced in the regions that range from x = -2.2i (or -110 m) to x = -0.7i (or -35 m) and from x = 0.7i (or 35 m) to x = 2.2i (or 110 m)) (see Figure 3.9b).

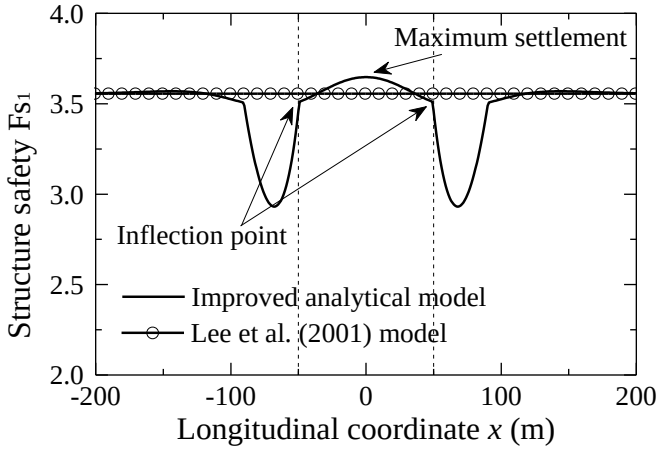

(a)

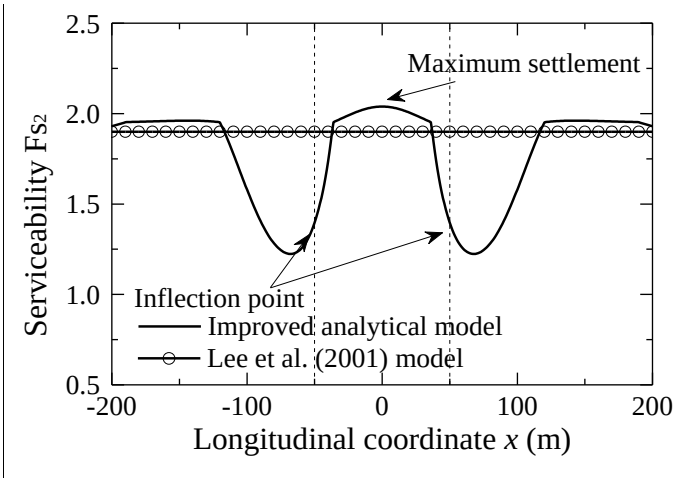

(b)

Figure 3.9: The longitudinal variation of the circumferential behavior of the segmental lining with Gaussian longitudinal settlement: (a) Structure safety of the segmental lining; (b) Serviceability of the segmental lining

Therefore, for a given shield tunnel with a Gaussian settlement curve, the most dangerous section of the circumferential behavior of the segmental lining is not located at the position with the maximum settlement, but rather in the regions that range from $x = -2.2i$ to $x = -0.7i$ and from $x = 0.7i$ to $x = 2.2i$. Therefore, the dangerous sections of a shield tunnel can readily be identified with the monitored tunnel longitudinal settlement curve using the proposed tunnel analytical model. This finding is significant, as more monitoring efforts could be assigned to these sections.

Validation of the proposed model

In this section, the proposed analytical model of jointed shield tunnels is validated using the 3-D FEM analysis by Liao et al. (2008). As depicted in Figure 3.10(a), the 3-D FEM analysis results of a shield tunnel with a Gaussian settlement curve showed that the convergence deformation of the segmental lining reached the maximum, indicated by the maximum vertical convergence deformation, near the inflection point (i.e., $x = \pm i$); the convergence deformation of the segmental lining reached the minimum, indicated by the minimum vertical convergence deformation, near the point with the maximum settlement (i.e., $x = 0$). For convenience of comparison, the longitudinal variation of the convergence deformation of this illustrative tunnel is analyzed with the proposed tunnel analytical model and plotted in Figure 3.10(b). While the magnitude of the convergence deformation in Figure 3.10(a) differs with that in Figure 3.10(b), the longitudinal

variations of the convergence deformation shown in Figure 3.10(a) and 3.10(b) are identical. The comparison between Figure 3.10(a) and 3.10(b) demonstrates that the proposed tunnel analytical model achieves comparable results of the convergence deformation of the segmental lining with the more complex 3-D FEM analysis, thus validating this proposed tunnel analytical model.

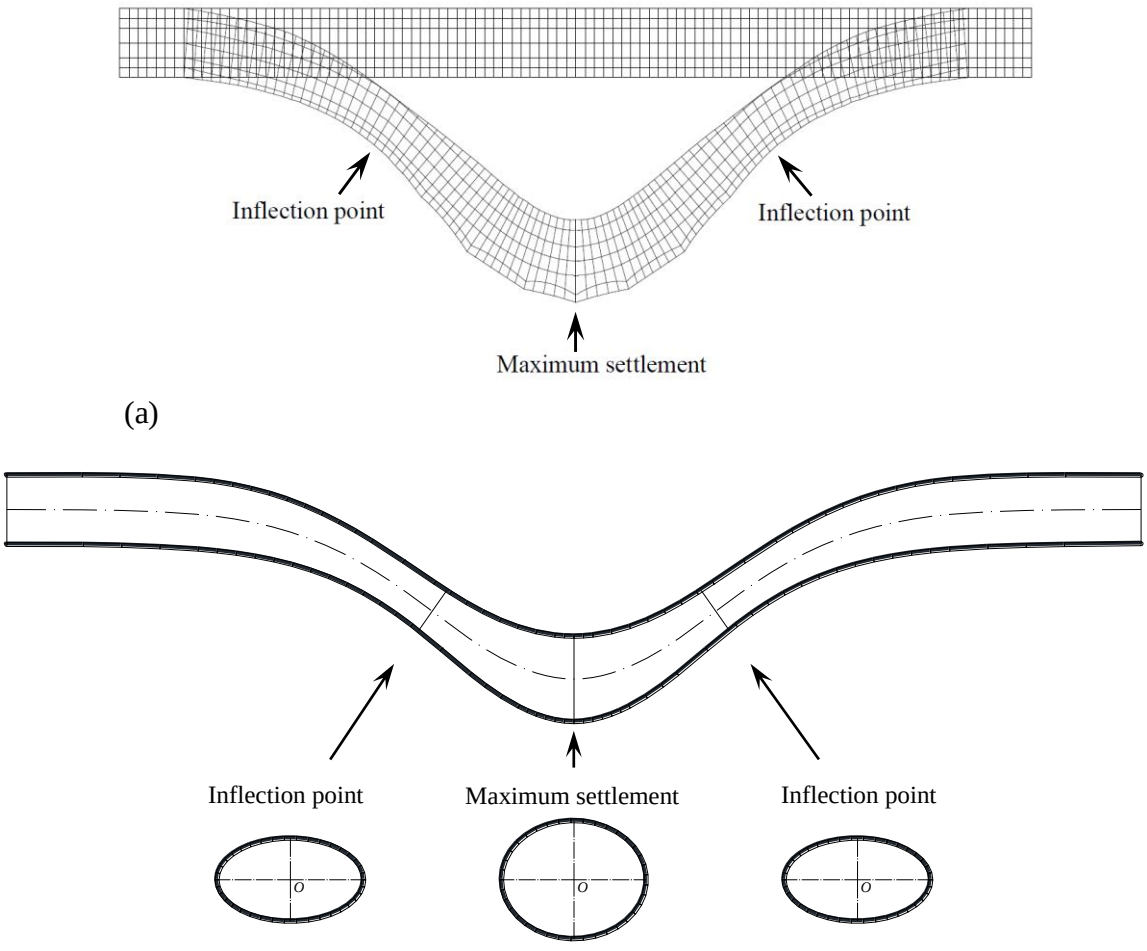

Figure 3.10: Validation of the proposed tunnel analytical model: (a) 3-D deformation of a shield tunnel with Gaussian settlement curve (Liao et al. 2008); (b). Convergence deformation along the longitudinal direction (obtained with the proposed tunnel analytical model)

Parametric Study

The circumferential behavior of the segmental lining, including both the structure safety and serviceability, is affected by factors such as the tunnel longitudinal settlement (e.g., curvature κ and fourth derivative $w^{(4)}$), the property of the surrounding ground (e.g., soil resistance coefficient *K*s), and the design parameters of the segmental lining (e.g., segment thickness *t*, flexural stiffness of the circumferential joints K_θ, and the flexural stiffness of the longitudinal joints). Here, six series of parametric studies (S-1 through S-6) are conducted to investigate how the circumferential behavior of the segmental lining is affected by these factors. For these parametric analyses, the parameter settings are listed in Table 3.3.

Table 3.3: Parameters settings in the parametric studies

Parameter	Parameters setting for different parametric study series					
	S-1	S-2	S-3	S-4	S-5	S-6
Curvature of tunnel settlement κ	–	2×10^{-4}	2×10^{-4}	2×10^{-4}	2×10^{-4}	2×10^{-4}
Fourth derivative of tunnel settlement $w^{(4)}$	8×10^{-8}	–	8×10^{-8}	8×10^{-8}	8×10^{-8}	8×10^{-8}
Soil resistance coefficient *K*s (kN/m^3)	15×10^{3}	15×10^{3}	–	15×10^{3}	15×10^{3}	15×10^{3}
Segment thickness *t* (m)	0.55	0.55	0.55	–	0.55	0.55
Circumferential joint stiffness ratio k_θ	0.14	0.14	0.14	0.14	–	0.14
Reduction factor of tunnel longitudinal flexural stiffness ζ	1/7	1/7	1/7	1/7	1/7	–

Effect of the longitudinal settlement

As seen in Eq. (3.1) & (3.3), the tunnel longitudinal differential settlement is the causative factor of both the shearing effect and flattening effect. Therefore, the additional

loads on the tunnel cross section from the shearing effect and flattening effect can be determined with the curvature (κ) and fourth derivative ($w^{(4)}$) of the tunnel settlement curve, respectively. Hence, parametric studies S-1 and S-2 are conducted to determine how the circumferential behavior of the segmental lining could be affected by the tunnel longitudinal settlement, and the results of which are plotted in Figure 3.11(a) and 3.11(b), respectively.

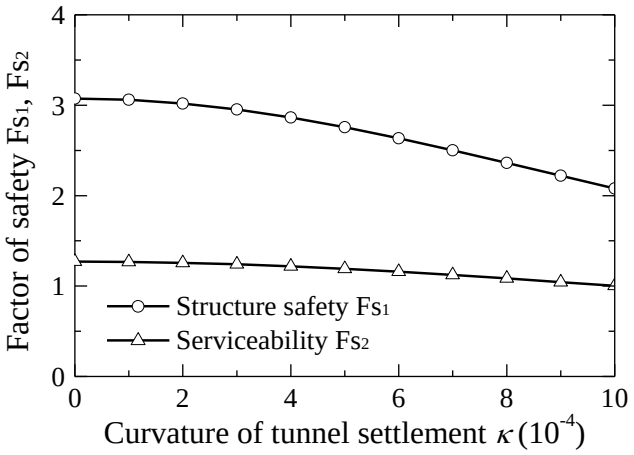

(a)

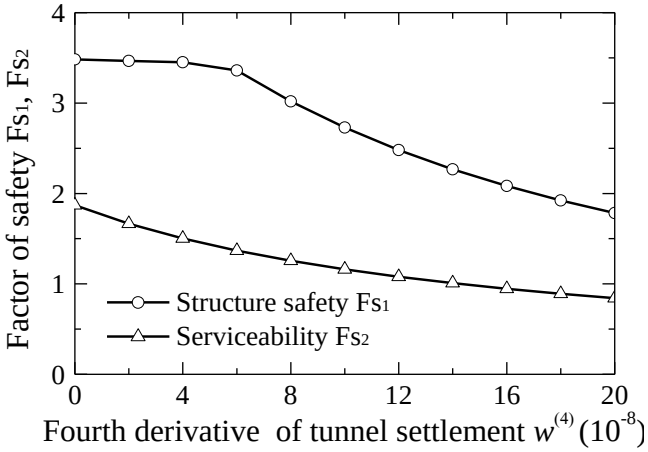

(b)

Figure 3.11: The circumferential behavior of the segmental lining versus tunnel settlement: (a) Curvature of the tunnel settlement; (b) Fourth derivative of the tunnel settlement

The plots in Figure 3.11(a) illustrate that both the structure safety and serviceability of the segmental lining tend to degrade with the increase of the curvature of tunnel longitudinal settlement. Similarly, the plots in Figure 3.11(b) show that both the structure safety and serviceability of segmental lining degrade with the fourth derivative of tunnel longitudinal settlement. The mechanisms of these observations in Figure 3.11 are easily interpreted: the additional loads on the tunnel cross section from both the shearing effect and the flattening effect increase with the curvature and the fourth derivative of the tunnel settlement, respectively, which further results in an increase of both the internal forces and convergence deformation of segmental lining. Thus the structure safety and the serviceability are degraded. As such, the tunnel sections with larger curvature and fourth derivative of tunnel settlement generally exhibit poorer circumferential behaviors.

Effect of the property of surrounding soil

The convergence deformation of the segmental lining in the horizontal direction is restricted by the surrounding ground, and the key soil parameter capturing this effect is the soil resistance coefficient (Ks). Thus, the parametric study S-3 is conducted to analyze how the circumferential behavior of the segmental lining is affected by the variation of the property of the surrounding ground, in which the ground condition varies from very soft (i.e., Ks = 3,000 kN/m^3) to very hard (i.e., Ks = 30,000 kN/m^3). Although the soil cohesion (c) and soil friction angle (ϕ) may also exhibit an influence on the

circumferential behavior of the segmental lining, such an analysis is reserved for future study.

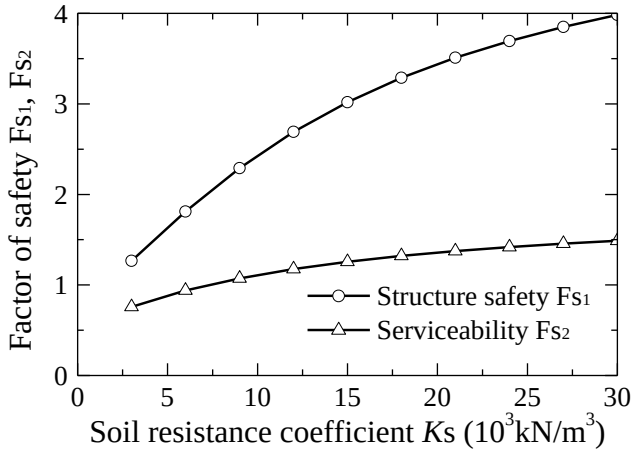

Figure 3.12: The circumferential behavior of the segmental lining versus the soil resistance coefficient

The parametric analysis results of S-3 are presented in Figure 3.12. As expected, both the structure safety and serviceability of the segmental lining enhance with the soil resistance coefficient. Such an improvement of the circumferential behavior of the segmental lining may be interpreted as follows: the soil resistance, induced by the horizontal convergence deformation of the segmental lining, increases with the ground conditions, and the increase of the soil resistance in turn leads to the decrease of both the tunnel internal forces and the convergence deformations, which results in an increase in both the structure safety and serviceability.

Effect of design parameters of the segmental lining

Since the inner radius of a given shield tunnel is often designed to meet the space that is determined by the tunnel functions, the tunnel inner radius (R_i) cannot be adjusted

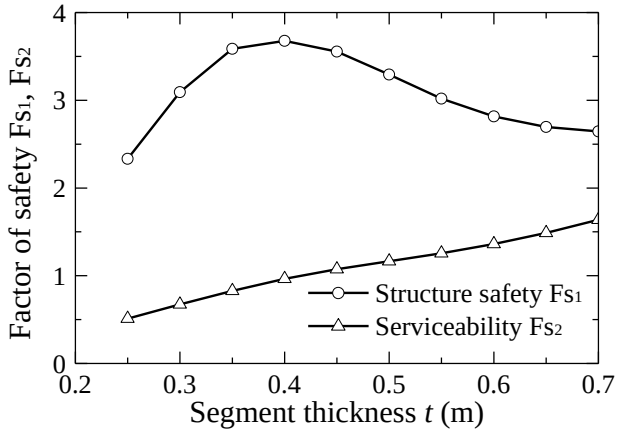
Factor of safety Fs1, Fs2
Structure safety Fs1
Serviceability Fs2
Segment thickness t (m)

(a)

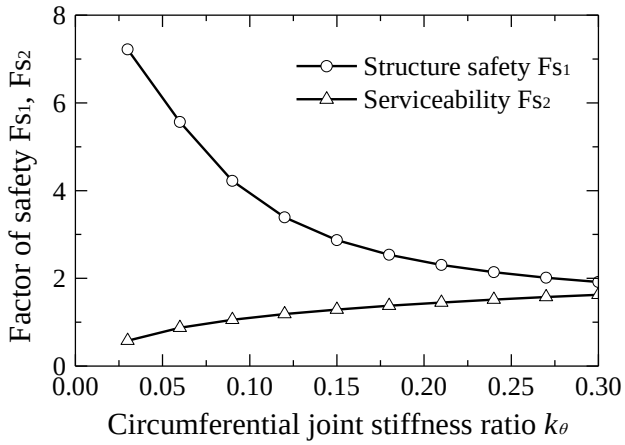
Factor of safety Fs1, Fs2
Structure safety Fs1
Serviceability Fs2
Circumferential joint stiffness ratio kθ

(b)

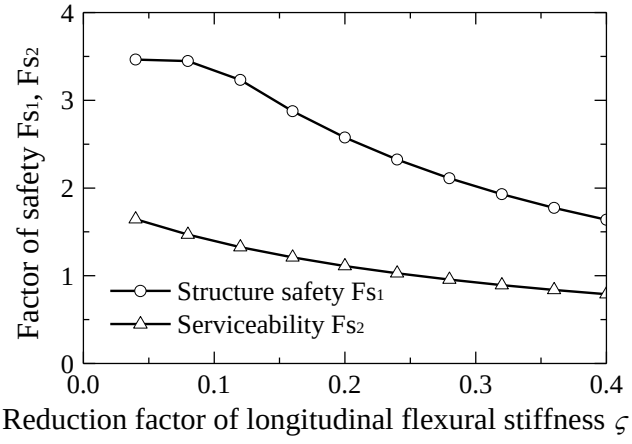
Factor of safety Fs1, Fs2
Structure safety Fs1
Serviceability Fs2
Reduction factor of longitudinal flexural stiffness ς

(c)

Figure 3.13: The circumferential behavior of the segmental lining versus the design parameters of the segmental lining: (a) Segment thickness; (b) Flexural stiffness of the circumferential joints; (c) Flexural stiffness of the longitudinal joints

arbitrarily by the designer. The parameters of the segment thickness (t), the flexural stiffness of the circumferential joints (K_θ), and the flexural stiffness of the longitudinal joints (which is represented with the reduction factor of the tunnel longitudinal flexural stiffness ζ) however, can be easily adjusted in this manner. The authors conduct parametric studies S-4, S-5, and S-6 to analyze how the circumferential behavior of the segmental lining could be affected by these easy-to-control design parameters, the results of which are illustrated in Figure 3.13(a), 3.13(b), and 3.13(c), respectively.

Figure 3.13(a) depicts the relationship between the circumferential behavior of the segmental lining and the segment thickness. As noted, the serviceability of the segmental lining always increases with the segment thickness; however, the structure safety tends to increase with the segment thickness when the segment thickness is small (for example, less than 0.4 m in this parametric study). When the segment thickness is already large enough, a further increase in the segment thickness may not enhance the structure safety of the segmental lining.

In general, the flexural stiffness of the segmental lining increases as the segment thickness is increased, which causes an increase of the internal forces and a decrease of the convergence deformation of the segmental lining. Therefore, the serviceability always increases with the segment thickness because of the decrease of the convergence deformation. On the other hand, even though the increase of the segment thickness can lead to an increase of the ultimate bearing capacity of the segmental lining, the structure

safety of the lining may not be enhanced. For example, the structure safety of the lining could be degraded *if* the effect of the increase of the internal forces due to the increased flexural stiffness is greater than that of the increase of the ultimate bearing capacity of the segmental lining.

Figure 3.13(b) illustrates that the increase of the flexural stiffness of the circumferential joints (indicated by the increase of the circumferential joint stiffness ratio k_θ) can effectively enhance the serviceability of the segmental lining, but not the structure safety (indeed, the effect is negative). These inconsistencies in the flexural stiffness of the circumferential joints on the circumferential behavior of the segmental lining shown in Figure 3.13(b) may be due to the fact that the increase in the flexural stiffness of the circumferential joints can lead to an increase of the internal forces and a decrease of the convergence deformation of the segmental lining, which enhances the serviceability while degrading the structure safety.

Figure 3.13(c) indicates that the increase of the flexural stiffness of the longitudinal joins (indicated by the increase of the reduction factor of the tunnel longitudinal flexural stiffness ζ) degrades both the structure safety and serviceability of the segmental lining. This negative effect of the flexural stiffness of the longitudinal joints on the circumferential behavior of the segmental lining can be easily understood with Eq. (3.1) & (3.3). For a given tunnel longitudinal settlement, the additional loads on the tunnel cross section from both the shearing effect and flattening effect increase with the flexural stiffness of the longitudinal structure of the segmental lining, which in turn causes an increase of both the internal forces and the convergence deformation of the

segmental lining. Thus both the structure safety and the serviceability of the segmental lining are degraded as a result.

Summary

This chapter presents an improved analytical model of jointed shield tunnels that explicitly considers the effect of the tunnel longitudinal differential settlement on the circumferential behavior of the segmental lining. In the proposed analytical model, the force method is used to incorporate both the shearing effect and the flattening effect into the existing tunnel analytical model of Lee et al. (2001). The derived analytical solution of jointed shield tunnels is verified by the published 3-D FEM analysis results. Further, an illustrative example is carried out to demonstrate the effectiveness of the derived analytical solution. Finally, parametric study is conducted to investigate how the structure safety and serviceability of tunnel segment ring is affected by different factors.

CHAPTER FOUR

ROBUST GEOTECHNICAL DESIGN OF SHIELD-DRIVEN TUNNELS[*]

Introduction

Benefiting from the advances of shield-driven machines and tunneling technologies, shield-driven tunneling has gained a world-wide popularity in the construction of tunnels in urban areas (Mair 2008; Beard 2010). Because of the inherent variability, testing error and transformation error, geotechnical parameters for design of shield tunnels are often hard to characterize with certainty (Phoon and Kulhawy 1999). To compensate for such uncertainties, a conservative estimate of geotechnical parameters is generally taken in the design. To further ensure safety, the computed factor of safety (Fs) for a feasible design is required to be greater than the *allowable* Fs, a value derived from past experience. Thus, the "true" safety level of a design is generally unknown, as the uncertainties are only implicitly considered.

To overcome the shortcoming of the above deterministic design method, probabilistic approaches that consider uncertainties *explicitly* have also been sought (Mollon 2009; Li and Low 2010; Lü and Low 2011; Špačková 2013). The uncertain geotechnical parameters are generally treated as random variables, and the outcome of the analysis of a design, referred to herein as the system response, is generally expressed

---

[*] A similar form of this chapter has been published at the time of writing: Gong, W., Wang, L., Juang, C. H., Zhang, J., and Huang, H. (2014). "Robust geotechnical design of shield-driven tunnels." Computers and Geotechnics, 56, 191-201.

as a reliability index or a probability of failure. In the practice of geotechnical engineering, the site-specific data is often limited, thus an accurate statistical characterization of the uncertain variables is indeed a challenging prerequisite for adopting probabilistic approaches. The value of a probabilistic analysis could be greatly undermined if the adopted joint distribution of input geotechnical parameters cannot be reliably determined.

Recently, the robust geotechnical design (RGD) methodology has been developed for analysis and design of geotechnical systems with uncertain input parameters (Juang et al. 2013 & 2014; Wang et al. 2013). In the context of robust design, a design is considered *robust* if the performance of the system is insensitive to the variation of uncertain geotechnical parameters. Within the RGD framework, the design robustness is sought along with safety and cost efficiency. The cost is primarily a function of *design parameters*, those that are "easy-to-control" by the designer, such as the geometry and dimensions of the system. Safety and robustness are, however, a function of the design parameters as well as the "hard-to-control" parameters, such as uncertain geotechnical parameters. In the context of the RGD, these hard-to-control parameters are termed "*noise factors*." The primary goal of RGD is to derive an optimal design (represented by a set of design parameters), in which the system response is robust against, or insensitive to, the variation of noise factors, while the requirements of safety and cost efficiency are also satisfied. The RGD provides a new perspective for designing geotechnical systems under an uncertain environment. Although applications of the RGD methodology in various geotechnical problems have been explored (Juang and Wang 2013; Juang et al.

2013 & 2014; Wang et al. 2013), it is based on probability theory which requires the probability density function of the uncertain variables. Moreover, it is based on repetitive reliability analysis and could be computationally intensive within the RGD framework.

When a fully statistical characterization of geotechnical parameter is difficult, the uncertain parameter can be alternatively modeled using the fuzzy set theory (Zadeh 1965). In the fuzzy set theory, an uncertain variable can be modeled with only knowledge of its highest conceivable value (HCV) and lowest conceivable value (LCV), which are generally easy to determine even with limited data (Duncan 2000). The application of fuzzy sets theory indeed has a track record in geotechnical engineering particularly when the site-specific data is limited (Juang et al. 1992; Juang et al. 1998; Sonmez et al. 2003; Luo et al. 2011). As will be seen later in this paper, the response of a system with fuzzy input data can be evaluated accurately and efficiently through the vertex method. Thus, the fuzzy set theory appears to be an effective and efficient means for representing and processing uncertain information in geotechnical engineering, and suitable for inclusion in the intended RGD framework for design of geotechnical systems.

The objective of this paper is thus to create and demonstrate a fuzzy set-based RGD methodology for design of complex geotechnical systems such as shield-driven tunnels. This paper is organized as follows. First, a deterministic model for design of shield-driven tunnels is introduced. Then, the vertex method to process fuzzy input data in this deterministic model for tunnel performance analysis is presented, followed by a probabilistic procedure to interpret the results of fuzzy set-based analysis. Thereafter, the fuzzy set-based RGD methodology is introduced and explained. Finally, a shield-driven

tunnel design example is studied to illustrate the effectiveness and significance of the proposed design methodology.

Deterministic Model for Shield-Driven Tunnel Performance Analysis

As a slender structure embedded underground, the performance of tunnel cross section with respect to the limit states of segment strength (ULS) and serviceability (SLS) is the major concern in the design of a shield-driven tunnel (ITA 2000; BTS 2004; MTPRC 2004; JSCE 2007), although the effect of tunnel longitudinal differential settlement should also be considered in cases (Liao et al. 2008; Huang et al. 2012). The focus of this paper is on the performance of non-staggering shield-driven tunnels. Before presenting the fuzzy set-based RGD, the adopted deterministic model for assessing the performance of shield-driven tunnels is first introduced.

Analytical solution of jointed tunnel internal forces and deformation

Among various existing approaches to analyze the internal forces and convergence deformation of jointed shield-driven tunnels (Wood 1975; Lee et al. 2001; Koyama 2003), the model by Lee et al. (2001) is adopted herein for its simplicity and wide acceptance. Figure 4.1 depicts the possible loads acting on a shield tunnel, including the earth pressure, water pressure, dead load, ground surface surcharge, and subgrade reaction.

As will be shown later, the segment thickness (t), segment steel reinforcement ratio (ρ) and diameter of joint bolt (D_j) are the key design parameters that affect the tunnel performance. The stiffness of segment is determined by the segment thickness and

reinforcement ratio, while the stiffness of the joint is dependent on the diameter of joint bolt and segment thickness. The stiffness of tunnel segment, E_cI_e, is calculated as:

$$E_cI_e = E_c\left[\frac{1}{12}bt^3 + 2(bt\rho)\frac{E_s}{E_c}\left(\frac{t}{2}-a\right)^2\right] \tag{4.1}$$

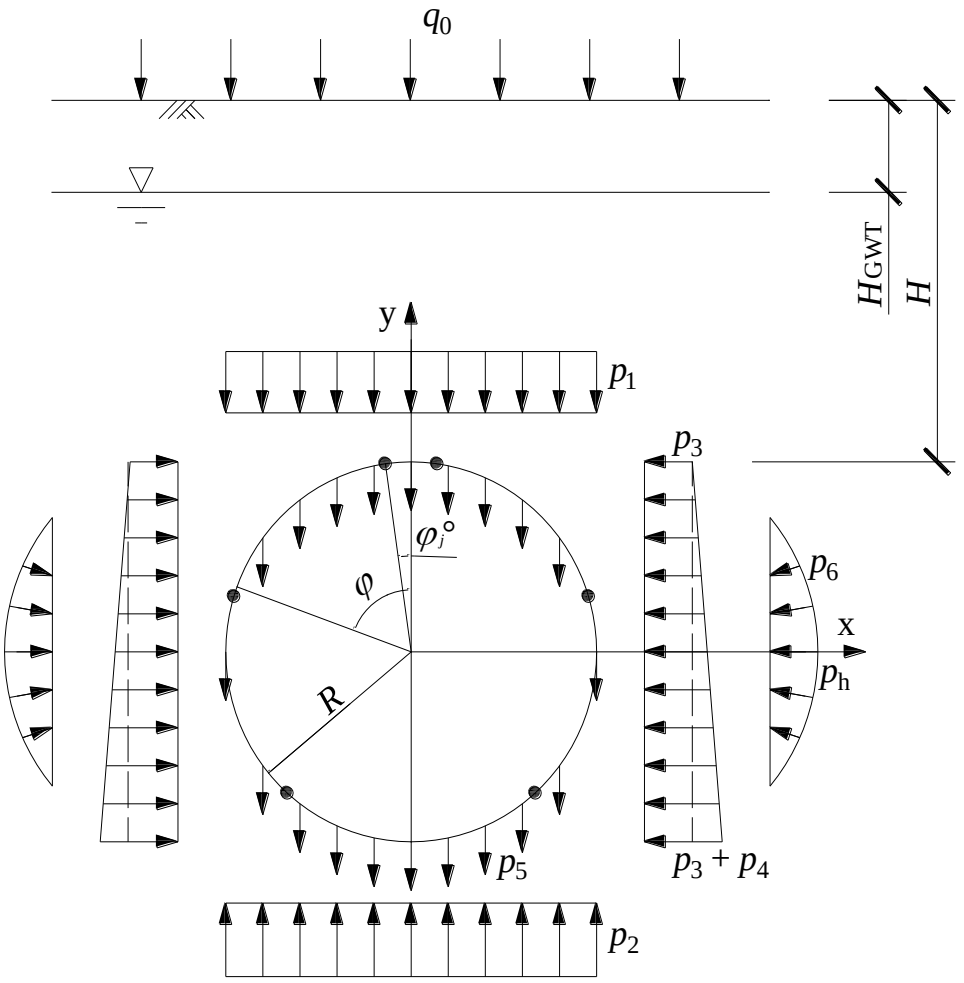

Figure 4.1: Schematic diagram of loads on a shield-driven tunnel cross-section

where E_c = the elastic modulus of concrete, E_s = the elastic modulus of steel bar, b = the width of tunnel ring, t = the thickness of tunnel segment, and, a = the concrete thickness

of protective cover for steel bar. With the assumptions that a) all the tension is beard by the bolts at joints; b) no pre-stress is applied to the bolts; and c) the adjacent tunnel segments are initially contacted, the joint stiffness, K_j, when subjected to the positive bending moment (i.e., the inside surface of tunnel segment is subjected to tension), can be estimated as:

$$K_j = \frac{E_c b x^2 \left(t - h - x/3\right)}{2 l_b} \tag{4.2}$$

where l_b = the length of joint bolt, B_s = the cross sectional area of the bolts at concerned joint, h = the position of the bolts center measured from the inside surface of the tunnel segment, and, x is defined as:

$$x = \sqrt{\frac{2E_s B_s}{E_c b}\left(t - h\right) + \left(\frac{E_s B_s}{E_c b}\right)^2} - \frac{E_s B_s}{E_c b} \tag{4.3}$$

For simplicity, the joint stiffness that subjected to negative bending moment is assumed to be equal to that subjected to positive bending moment.

With the computed load and stiffness of the tunnel lining, the internal forces and convergence deformation of tunnel cross section are readily calculated through the existing model (Lee et al. 2001). The resulting internal forces and deformation can be used to assess the segment structure safety (based on ULS) and serviceability (based on SLS) of tunnel cross section.

Assessment of the performance of tunnel cross section

Plasticity theory is adopted here to assess tunnel segment structure safety based on the ultimate limit state (ULS) that utilizes the strength of both steel reinforcement and concrete (ITA 2000). In reference to Figure 4.2, the structure failure of tunnel segment is only said to occur when the internal forces combination (M, N) exceeds the corresponding limit state (M_{Lm}, N_{Lm}) on the ultimate bearing envelope of tunnel segment, derived from the plasticity theory. As depicted in Figure 4.2, the factor of safety, Fs_1, for the tunnel segment safety (ULS) in a deterministic approach is calculated as:

$$Fs_1 = \frac{\sqrt{N_{Lm}{}^2 + M_{Lm}{}^2}}{\sqrt{N^2 + M^2}} \tag{4.4}$$

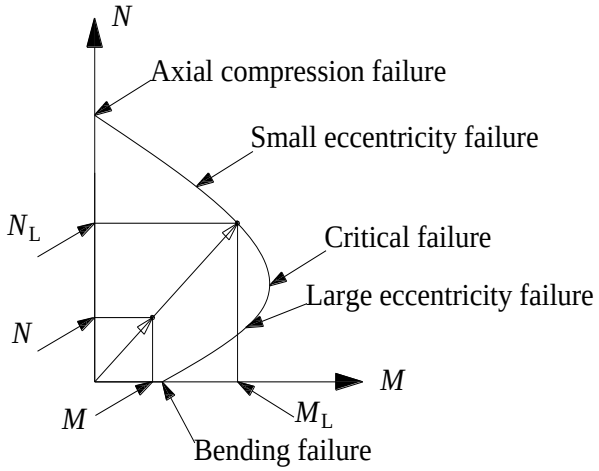

Figure 4.2: Structure safety assessment of tunnel segment using plasticity theory

Note that the value of Fs_1 varies with the circumferential position within the tunnel ring of concern. Thus, the ULS is governed by the cross section with minimum value of F_{S1}. As the critical position may change with the input parameters, the minimum

value of F_{S1} is searched along the circumferential direction each time as the input parameters vary during the subsequent fuzzy set analysis.

Meanwhile, the maximum tunnel convergence deformation is adopted herein to assess the tunnel serviceability (SLS). As specified in the Chinese metro code (MCPRC 2003), the maximum convergence deformation of a shield-driven tunnel must be controlled under 0.4%*D* to 0.6%*D* (*D* denotes the outer diameter of the tunnel) to prevent the operational distress. Thus, in a deterministic approach, the factor of safety against the tunnel serviceability distress, Fs_2, can be conservatively defined as:

$$Fs_2 = \frac{0.4\%D}{\max(\Delta_v, 2\Delta_h)} \tag{4.5}$$

where Δ_v and $2\Delta_h$ are the calculated tunnel convergence deformation in the vertical direction and horizontal direction, respectively.

Analysis of Tunnel Performance with Fuzzy Input Data

Modeling soil parameters with fuzzy sets (or fuzzy numbers)

A fuzzy set is a set of ordered pairs, [x, $\mu(x)$], where a member x belongs to the set with a certain level of confidence, called membership grade, $\mu(x)$. This set of ordered pairs collectively defines a membership function that specifies a membership grade for each member (Zadeh 1965). A fuzzy set with a membership function that is convex in shape, and with its highest membership grade equal to 1, is a special fuzzy set called fuzzy number. As an example, the drained friction angle (φ) of a sand described as "about 32°" based on a very limited test data indicates an uncertainty about the statement

of $\varphi = 32°$. Though this friction angle may be characterized as a random variable with an assumed probability distribution, the available limited data do not allow for such precise statistical characterization. Alternatively, the assertion of "about 32°" can be intuitively represented as a fuzzy number of $\overline{32°}$, where the highest membership grade (support) is equal to 1.0 for $\varphi = 32°$. If the highest conceivable value (HCV) and lowest conceivable value (LCV) of φ can be estimated based on engineering judgment, say HCV = 36° and LCV = 28°, then a fuzzy number $\overline{32°}$ will be completely defined. The implication is that the membership grade for HCV and LCV are both equal to 0, as shown in Figure 4.3.

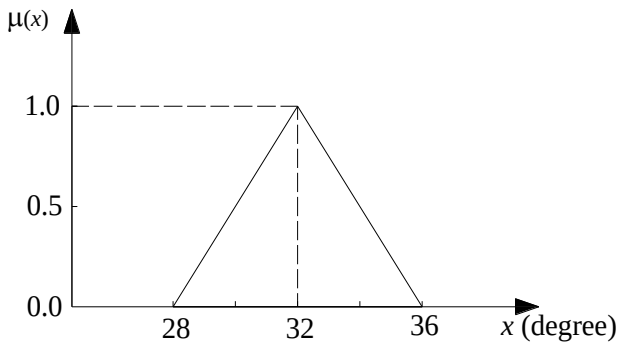

Figure 4.3: An example of a fuzzy number $\overline{32°}$

In this study, the uncertain geotechnical parameters are all modeled with triangular fuzzy numbers (i.e., fuzzy numbers with a triangular shape membership function, as shown in Figure 4.3). Of course, other membership function, such as trapezoidal shape, can be used. The triangular fuzzy number is used in this paper for its simplicity and efficiency within the RGD framework. Interested readers are referred to the literature of the modeling and application of fuzzy data in geotechnical engineering (Juang et al. 1992; Juang et al. 1998; Sonmez et al. 2003; Luo et al. 2011).

Vertex method for the uncertainty propagation

With the uncertain input geotechnical parameters represented with triangular fuzzy numbers, the system responses (i.e., Fs_1 based on ULS and Fs_2 based on SLS, as per Eq. 4.4 & 4.5, respectively) for a given shield-driven tunnel can be analyzed using the vertex method (Dong and Wong 1987). This method is based on α-cut concept. In reference to Figure 4.4(a), an interval with a lower bound of $x_{a_i}^-$ and an upper bound of $x_{a_i}^+$ can be formed at a given membership grade of α_i. Theoretically, a fuzzy number can be fully represented by a set of α-cut intervals with α ranging from 0.0 to 1.0.

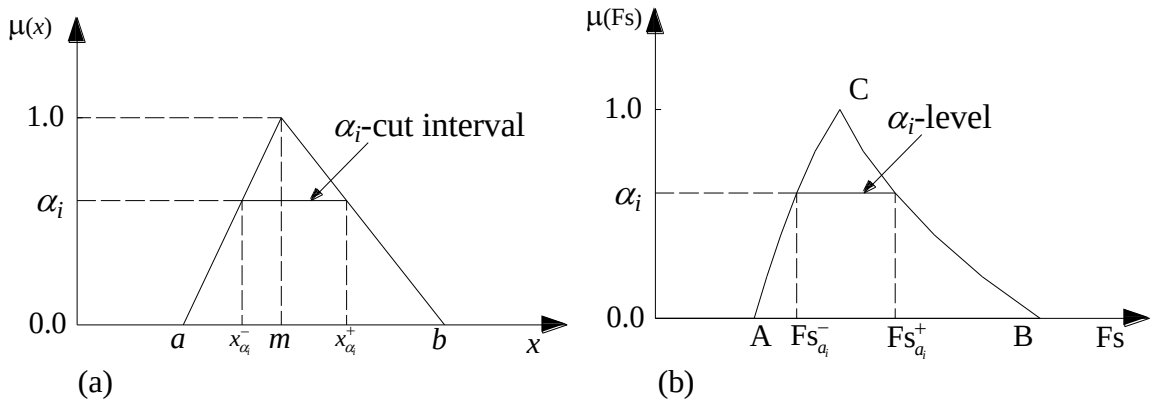

Figure 4.4: α-cut (α-level) intervals for uncertainty propagation analysis using vertex method: (a) α_i-cut interval of an input fuzzy number; (b) Fuzzy output (fuzzy safety factor) at α_i-cut level

Through the vertex method, the system response can be analyzed with the following steps (Dong and Wong 1987; Juang et al. 1998; Luo et al. 2011):

1) The input fuzzy data are first discretized into a set of α-cut intervals. For example, taking $\Delta\alpha = 0.2$ yields 6 different α-cut levels (i.e., $\alpha = 0$, 0.2, 0.4, 0.6, 0.8, and

1.0). The step size of $\Delta\alpha$ = 0.2 is found adequate in this paper to achieve a converged result.

2) At each α-cut level, the intervals of all input fuzzy numbers are obtained and the combinations of vertexes can be formed. The number of vertex combinations is 2^n for a system with *n* input fuzzy numbers.

3) At each α-cut level, different vertex combination represents different set of input data to the solution model, and with which, the system response (Fs) is computed. This process is repeated for all 2^n vertex combinations, yielding 2^n Fs values. Taking only the minimum and maximum values of which, an interval (i.e., $Fs_{a_i}^-$ and $Fs_{a_i}^+$) of Fs can be formed, which represents the system response at this specified α-level, as shown in Figure 4.4(b).

4) Once the intervals of Fs for all α-cut levels are obtained, the final fuzzy factor of safety that represents the system response with fuzzy input data is established.

In the design of shield-driven tunnels, the system response of concern is the state of safety in the tunnel cross section, consisting of factors of safety Fs_1 (Eq. 4.4) and Fs_2 (Eq. 4.5). With fuzzy input data, the resulting factors of safety are fuzzy numbers. Although a fuzzy factor of safety such as the one shown in Figure 4.4(b) provides much information about the state of safety, including lower bound, upper bound, and mode of factor of safety, and the likelihood (or support) of these values and any other value in the range defined by the lower bound and upper bound, it is desirable to have a single value representation of the state of safety so that it can be readily incorporated into the RGD framework for the design of the shield-driven tunnel. To this end, an index of the safety

state, such as a reliability index or failure probability, is desirable. Such index is interpreted from the resulting fuzzy factor of safety.

Probabilistic interpretation of the resulting fuzzy factor of safety

Various methods have been suggested to estimate the failure probability (P_f) of a geotechnical system with fuzzy system response (Shrestha and Duckstein 1998; Giasi et al. 2003; Park et al. 2012). Most of such methods are based on normalization of the membership function of the fuzzy factor of safety into a probability density function, assuming that the probability density function is proportional to the membership function. As will be seen in the following, while convenient, such a procedure may not be rigorous from a probabilistic point of view. For each point [Fs, μ(Fs)] on the membership function as shown in Figure 4.4(b), the term μ(Fs) measures the membership grade or the degrees of belief for this Fs value; it is not a probability. From the probabilistic point of view, the chance of occurrence of a possible outcome of Fs, for example, $\mathrm{Fs}_{a_i}^{-}$ (or $\mathrm{Fs}_{a_i}^{+}$), as shown in Figure 4.4(b), depends on the membership grades of the *n* input fuzzy numbers. Since each of the *n* input fuzzy numbers has the same membership grade of α_i, the chance of occurrence of $\mathrm{Fs}_{a_i}^{-}$ (or $\mathrm{Fs}_{a_i}^{+}$) can be approximated as $(\alpha_i)^n$, which is inspired by an analogy of finding the joint probability of occurrence of a series of *n* independent events each with a chance of α_i.

To satisfy the axiom of probability, the chance of occurrence for Fs = $\mathrm{Fs}_{\alpha_i}^{-}$ (or $\mathrm{Fs}_{a_i}^{+}$), which is $(\alpha_i)^n$, must be transformed into a probability p_i so that the discrete fuzzy

membership function can be converted into a discrete probability mass function, as shown in Figure 4.5. To this end, the following equation for p_i at Fs = $\mathrm{Fs}_{\alpha_i}^{-}$ (or $\mathrm{Fs}_{\alpha_i}^{+}$) is proposed:

$$p_i = \frac{(\alpha_i)^n}{2\sum_{i=1}^{i=5}(\alpha_i)^n + (\alpha_6)^n} \tag{4.6}$$

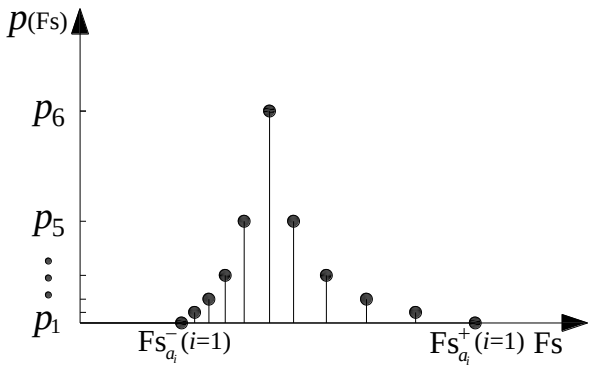

Figure 4.5: Resulting fuzzy factor of safety interpreted as a discrete distribution of probability

where α_i is a given membership grade, and n is the number of input fuzzy parameters. According to the axiom of probability, the following condition must be satisfied: 2 (p_1 + p_2 + p_3 + p_5 + p_5) + p_6 = 1.

To validate this suggested probabilistic interpretation of the resulting fuzzy factor of safety, Monte Carlo simulations (MCS) are employed here. A shield-driven tunnel subjected to loading as shown in Figure 4.1 and with input parameters described in the case study presented later in Section 5, is analyzed for its safety performance. The analysis of the tunnel performance is first carried out using the vertex method and the

probabilistic interpretation procedure with uncertain parameters represented as triangular fuzzy numbers (see Table 4.2 and Figure 4.4a). The results (in terms of Fs_1 and Fs_2) are presented in Figure 4.6 as discrete data points (i.e., discrete distribution of Fs). Then, MCS runs are carried out with uncertain parameters (see Table 4.2) represented as equivalent triangular distribution and truncated normal distribution (truncated at the mean plus and minus 3 standard deviations), respectively. These distribution functions have the same mean and the lower and upper bounds as their triangular fuzzy number counterparts. The outcome of the MCS runs is a continuous distribution of Fs, also shown in Figure 4.6.

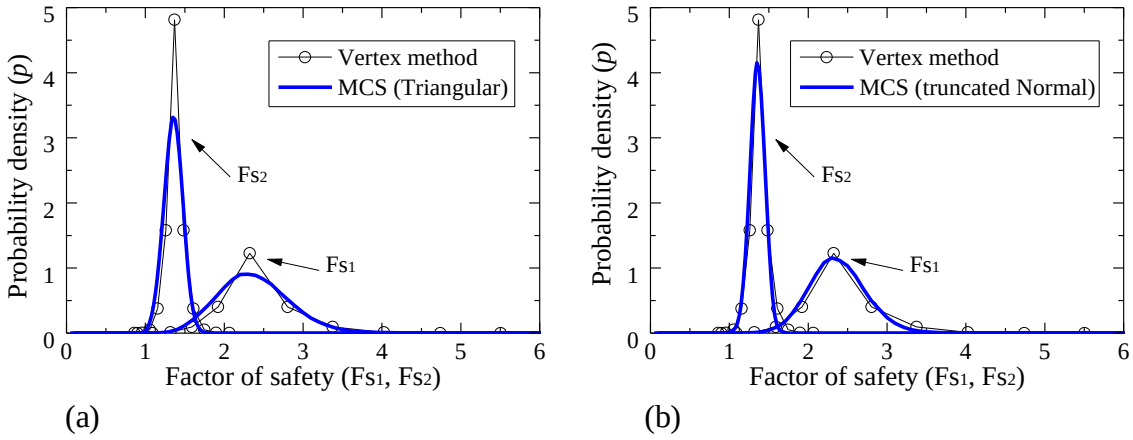

Figure 4.6: Validation of the proposed fuzzy set-based approach with triangular membership function versus MCS: (a) MCS with equivalent triangular distribution; (b) MCS with equivalent truncated normal distribution

Based on the comparisons made in Figure 4.6, the fuzzy set-based approach as described previously is shown to produce a close approximation to the MCS results. Because the fuzzy set-based approach is computationally more efficient than the MCS approach, and because it is easier and more efficient to be implemented within the RGD

framework, it is adopted in the modified RGD methodology in this study. The advantage of using the fuzzy set-based approach for uncertainty propagation analysis is amplified in the RGD that involves a multi-objective optimization process.

According to the discrete probability mass function defined in Eq. (4.6), the mean (E[Fs]) and standard deviation (σ[Fs]) of the resulting factor of safety can be readily calculated:

$$E[\mathrm{Fs}] = \sum_{i=1}^{i=5} p_i \left(\mathrm{Fs}_{\alpha_i}^{-} + \mathrm{Fs}_{\alpha_i}^{+} \right) + p_6 \mathrm{Fs}_{\alpha 6} \tag{4.7}$$

$$\sigma^2[\mathrm{Fs}] = \sum_{i=1}^{i=5} p_i \left[\left(\mathrm{Fs}_{\alpha_i}^{-} - E[\mathrm{Fs}] \right)^2 + \left(\mathrm{Fs}_{\alpha_i}^{+} - E[\mathrm{Fs}] \right)^2 \right] + p_6 \left(\mathrm{Fs}_{\alpha 6} - E[\mathrm{Fs}] \right)^2 \tag{4.8}$$

If the discrete random variable is approximated with a continuous lognormal variable (since Fs cannot assume a negative value), then the reliability index (β) of the performance of tunnel cross section with respect to ULS or SLS can be evaluated using the knowledge of E[Fs] and σ[Fs] as follows:

$$\beta = \ln\left(E[\mathrm{Fs}] \Big/ \sqrt{1 + \left(\frac{\sigma[\mathrm{Fs}]}{E[\mathrm{Fs}]} \right)^2} \right) \Bigg/ \sqrt{\ln\left(1 + \left(\frac{\sigma[\mathrm{Fs}]}{E[\mathrm{Fs}]} \right)^2 \right)} \tag{4.9}$$

Fuzzy Set-Based Robust Geotechnical Design (RGD) Methodology

In the previously developed reliability-based robust geotechnical design (RGD) methodology (Juang et al. 2013 & 2014; Wang et al. 2013), the failure probability (P_f) of

the geotechnical system was considered as the *system response*, while the variation of failure probability was used to measure the design robustness. Although this reliability-based RGD methodology is fundamentally sound and has been demonstrated as an effective design tool, there is room for improvement. First, it is computationally demanding especially for geotechnical problems that require complex solution models (e.g., finite element models). Second, it requires an evaluation of the mean and standard deviation of the coefficient of variation (COV) of key soil parameters, which can be challenging for the practicing engineers who are not well versed in the reliability theory. Therefore, the fuzzy set-based RGD methodology is proposed herein for design of shield-driven tunnels.

Optimization setting for fuzzy set-based robust geotechnical design

Unlike that in the reliability-based RGD methodology, the noise factors in the proposed fuzzy set-based RGD are the uncertain geotechnical parameters themselves, not the statistics of these parameters. Thus, there is no need to estimate the variation of COV of these parameters. In this paper, the noise factors (i.e., the uncertain geotechnical parameters) are represented as fuzzy numbers. The design parameters are the segment thickness (t), steel reinforcement ratio of segment (ρ) and diameter of joint bolt (D_j). The system responses of concern are the factors of safety (i.e., Fs_1 based on ULS and Fs_2 based on SLS). Within the context of RGD, the variation of the system response is minimized (i.e., the robustness is maximized) by adjusting design parameters while the traditional requirements of safety and cost efficiency are satisfied. After a preliminary assessment, the "signal-to-noise ratio" *SNR* (Phadke 1989; Schmidl and Cox 1997; Wu

and Wu 2000; Braslavsky et al. 2007) is adopted herein as a measure of design robustness, which is defined as:

$$SNR = 10 \log_{10}\left(\frac{E^2[\mathrm{Fs}]}{\sigma^2[\mathrm{Fs}]}\right) \tag{4.10}$$

where E[Fs] and σ[Fs] are directly computed from the output – fuzzy factor of safety (per Eq. 4.7 & 4.8). Accordingly, a higher *SNR* means less variation of the system response (in terms of Fs), and thus higher design robustness is acquired.

Find:	(t, ρ, D_j)
Subjected to:	$t_l \le t \le t_u$; $\rho_l \le \rho \le \rho_u$; $D_{jl} \le D_j \le D_{ju}$; $\beta_1 \ge \beta_{T1}$; $\beta_2 \ge \beta_{T2}$
Objective:	Minimizing the cost, $C(t, \rho, D_j)$

(a)

Find:	(t, ρ, D_j)
Subjected to:	$t_l \le t \le t_u$; $\rho_l \le \rho \le \rho_u$; $D_{jl} \le D_j \le D_{ju}$; $\beta_1 \ge \beta_{T1}$; $\beta_2 \ge \beta_{T2}$
Objective:	Maximizing the robustness index of ULS, SNR_1 Maximizing the robustness index of SLS, SNR_2 Minimizing the cost, $C(t, \rho, D_j)$

(b)

Figure 4.7: Optimization algorithms of shield-driven tunnel design: (a) Optimization algorithm for reliability-based design; (b) Optimization algorithm for RGD

Figure 4.7(a) shows a typical optimization setting of a traditional reliability-based design where the safety requirements are set as constraints, the design parameters are

searched in some ranges (also set as constraints), while those designs that satisfy the constraints are optimized for cost. Figure 4.7(b) shows the optimization setting for RGD, in which the safety requirements (i.e., reliability index β_1 based on ULS and β_2 based on SLS) are also set as constraints, while the design robustness (i.e., SNR_1 based on ULS and SNR_2 based on SLS) and the cost, $C(t, \rho, D_j)$, are optimized. The main difference between Figure 4.7(a) and Figure 4.7(b) is the addition of the design robustness as an additional objective. As in a reliability-based design, the safety requirement of a design in the RGD is guaranteed through following settings: $\beta_1 \geq \beta_{T1}$ and $\beta_2 \geq \beta_{T2}$, where β_{T1} and β_{T2} are the target reliability indexes based on ULS and SLS, respectively. This safety constraint assures that the resulting optimal designs are compulsorily brought to the specified target level while the robustness and cost efficiency are optimized.

Within the context of RGD of shield-driven tunnels, the design parameters (i.e., t, ρ, and D_j) are to be optimized in a continuous design space of $[t_l, t_u]$, $[\rho_l, \rho_u]$ and $[D_{jl}, D_{ju}]$, which is pre-assigned based on local experience and judgment. Obviously, the final optimal design parameters should be rounded to the nearest discrete values for construction convenience.

Multi-objective optimization of RGD

Generally speaking, in a multi-objective optimization problem (in reference to Figure 4.7b), a "utopia" solution that is optimal with respect to all objectives simultaneously is not attainable. Nevertheless, a set of non-dominated optimal solutions might exist that are superior to all others in the design space; but within this set, none of

them are superior or inferior to others. This set of non-dominated optimal solutions forms a Pareto front. In this study, the Non-dominated Sorting Genetic Algorithm version II (NSGA-II) (Deb et al. 2002), is employed to identify the Pareto front in the pre-assigned continuous design space. With an established Pareto front, which typically shows a trade-off relationship between the conflicting objectives, an informed decision might be made. For example, based on a desired level of cost, the design that yields the highest robustness is the most preferred design. Alternative, at a desired level of robustness, the least cost design can be selected as the most preferred design.

Case Study

Parameters setting

In reference to Figure 4.1, an illustrative example is adopted herein to demonstrate the proposed fuzzy set-based RGD methodology for the design of shield-driven tunnels. Basic parameters to assess the tunnel performance with respect to ULS and SLS are listed in Table 4.1. For this illustrative example, the unit weight of soil (γ) and water (γ_w) are both treated as fixed parameters due to their negligible variation comparing with other geotechnical parameters, such as soil resistance coefficient (Ks), soil cohesion strength (c), soil friction angle (φ) and ground water table (H_{GWT}). In addition to the geotechnical parameters (i.e., Ks, c, φ, and H_{GWT}), the surcharge (q_0) on the ground surface also involves significant variability, and its effect on the tunnel performance cannot be ignored. Collectively, these five parameters are dealt as noise factors in this example. The uncertainties in these noise factors are represented using

fuzzy numbers, and detailed parameters to characterize the membership functions of these fuzzy numbers are listed in Table 4.2 (Foundation Design Code 1999). The upper and lower bounds (HCV and LCV) of noise factors listed in Table 4.2 are determined based on local experience, literature reports, and engineering judgment. The design parameters in the RGD of a shield-driven tunnel, including the segment thickness (t), steel reinforcement ratio (ρ) and diameter of joint bolt (D_j), are to be optimized in a pre-assigned continuous design space. For example, based on local practice in Shanghai, China, the design space can be determined, as shown in Table 4.3. The optimization algorithm shown in Figure 4.7(b) is then adopted for RGD of the shield driven tunnel in this example.

Table 4.1: Deterministic parameters for assessing tunnel performance

Category	Parameter	Value
Tunnel	Embedded depth (H: m)	15.0
	Tunnel inner radius (R_{in}: m)	2.75
	With of tunnel ring (b: m)	1.0
	Joint position of half structure (φ_i: °)	8, 73, 138
Concrete segment	Unit weight of concrete (γ_c: kN/m^3)	25.0
	Elastic modulus of concrete (E_c: kN/m^2)	35×10^6
	Compression strength of concrete (f_c: kN/m^2)	39×10^3
	Ultimate plastic strain of concrete (ε_p)	0.0033
Steel reinforcement	Elastic modulus of steel (E_s: kN/m^2)	210×10^6
	Yielding strength of steel bar (f_y: kN/m^2)	345×10^3
	Thickness of protective cover (a: m)	0.05
Joint bolt	Bolt length (l_b: m)	0.4
	Number of bolts at each joint	2
	Distance from bolts center to tunnel inside surface (h)	t/3

Table 4.2: Parameters characterizing membership functions of noise factors

Noise factors	Lower	Mode	Upper

	bound (a)	[$m = (a + b)/2$]	bound (b)
Soil resistance coefficient (Ks: kN/m^3)[a]	3500	9250	15000
Soil cohesion strength (c: kN/m^2)[a]	0	7.5	15
Soil friction angle (φ: °)[a]	30	32.65	35.3
Ground water table (H_{GWT}: m)[b]	0.5	1.25	2
Ground surcharge (q_0: kN/m^2)[c]	0	10	20

[a] Data from Shanghai code DGJ08-11-1999 (Foundation Design Code 1999);
[b] Data from site investigation in Shanghai metro line 13;
[c] Data from engineering experience

Table 4.3: Design space of the RGD of shield-driven tunnel

Design parameter	Assigned ranges	Value
Segment thickness (t)	Lower limit (t_l: m)	0.200
	Upper limit (t_u: m)	0.500
Steel reinforcement ratio (ρ)	Lower limit (ρ_l: %)	0.50
	Upper limit (ρ_u: %)	4.00
Diameter of joint bolt (D_j)	Lower limit (D_{jl}: mm)	10.0
	Upper limit (D_{ju}: mm)	50.0

For illustration purpose, the target reliability indexes (i.e., β_{T1} and β_{T2}) with respect to ULS and SLS are set as 4.2 and 2.7, respectively, while the target failure probabilities (i.e., P_{fT1} and P_{fT2}) are 1.33×10^{-5} and 0.35×10^{-3} (MCPRC 2001), respectively. Also for illustration purpose, only the material cost of one tunnel ring (tunnel cross section) is investigated for simplicity, which consists of segment concrete cost, steel reinforcement cost and joint bolts cost. Based on the market survey in Shanghai, the unit prices of segment concrete, reinforcement steel, and joint bolts are c_c = 600 RMB/m^3 (97.77 USD/m^3), c_s = 4000 RMB/10^{3}kg (645.16 USD/10^{3}kg), and c_b = 10 RMB/kg (1.61 USD/kg), respectively. Thus, the cost function $C(t, \rho, D_j)$ in the RGD of a shield-driven tunnel is computed as:

$$C(t,\rho,D_j) = c_c Q_c + c_s Q_s + c_b Q_b \tag{4.11}$$

where Q_c, Q_s, and Q_b = the quantity of concrete (m^3), steel bar (10^3kg), and joint bolts (kg) of the shield-driven tunnel per ring, respectively.

Design parameters on the safety, robustness, and cost of shield-driven tunnel

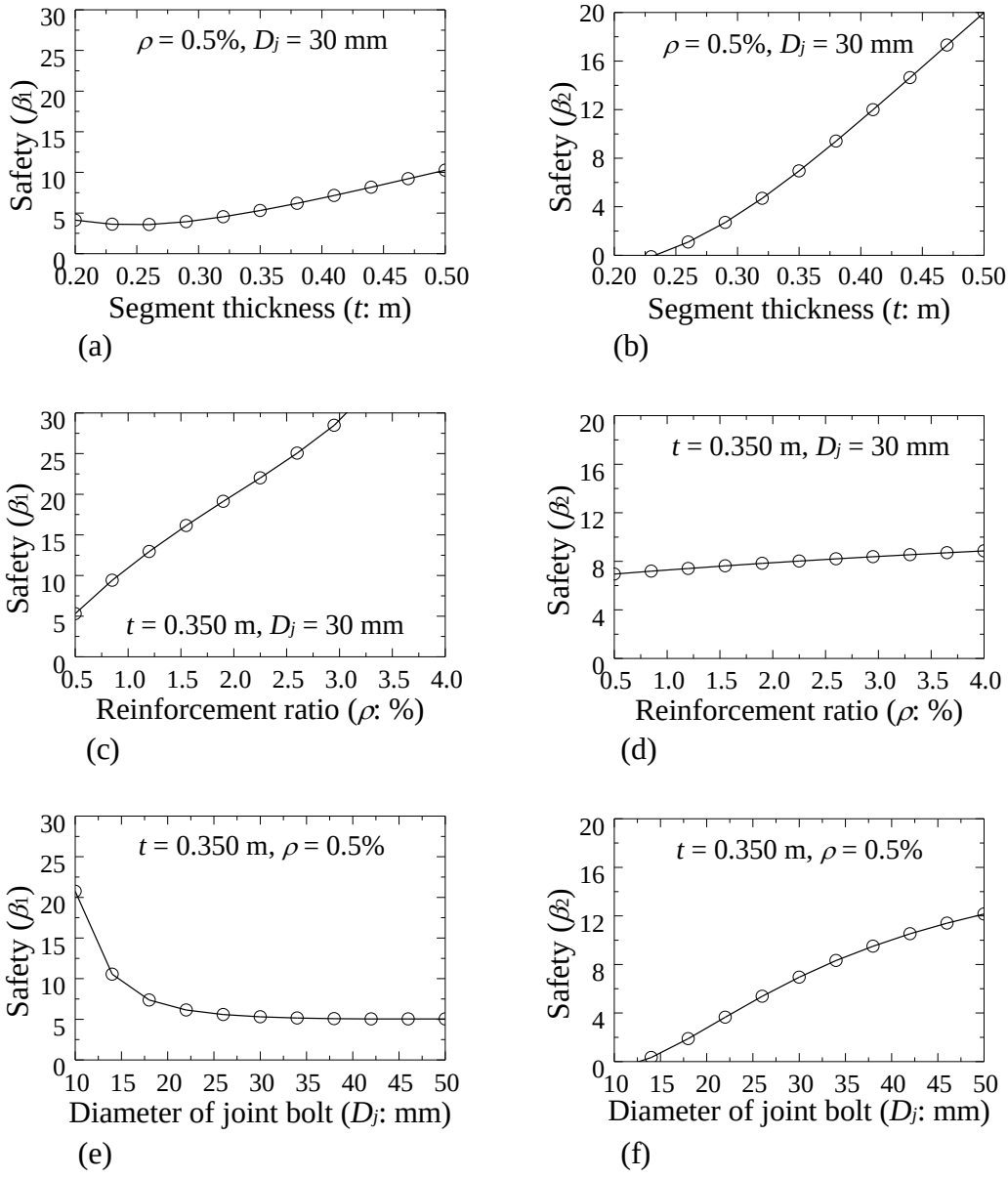

Figure 4.8: Tunnel performance: Safety versus design parameters: (a) β_1 versus t; (b) β_2 versus t; (c) β_1 versus ρ; (d) β_2 versus ρ; (e) β_1 versus D_j; (f) β_2 versus D_j

Before the implementation of the robust design of the shield-driven tunnel, a series of parametric analyses are carried out here to investigate how the design parameters (i.e., t, ρ, and D_j) affect the safety, robustness, and cost of the shied-driven tunnel, which provides a background and sensitivity study for the robust design of the shield-driven tunnel. Within the pre-defined design space of design parameters listed in Table 4.3, the effect of each design parameter on the safety performance of tunnel cross section, in terms of β_1 and β_2, is first studied, and the results are plotted in Figure 4.8. Figure 4.8(a) & 4.8(b) show the effect of segment thickness on the reliability of tunnel with respect to ULS and SLS, respectively. As the segment thickness increases, both the tunnel stiffness and bearing capacity of the tunnel segment increase. As the stiffness of the tunnel lining increases, tunnel structure tends to bear more internal forces but deforms less (Lee et al. 2001). In Figure 4.8(a), the reliability with respect to ULS decreases first with the segment thickness slightly, and then increases with the lining thickness, indicating that at the beginning the effect of increase in internal forces caused by the increase in stiffness is slightly more pronounced, but it was later overwhelmed by the effect of increase in bearing capacity. In Figure 4.8(b), the reliability with respect to SLS increases with the lining thickness as a thicker lining implies more stiffness and hence less deformation. Figure 4.8(c) & 4.8(d) show the effect of reinforcement ratio on the reliability with respect to ULS and SLS, respectively. The reinforcement ratio can enhance the bearing capacity, but has minor effect on the stiffness of the tunnel systems.

Thus, it is reasonable to observe an increase of reliability of ULS with the reinforcement ratio, but the reliability of SLS is relatively insensitive to the reinforcement ratio. Figure 4.8(e) & 4.8(f) show the effect of diameter of the joint bolt on the reliability with respect to ULS and SLS, respectively. The increase in the diameter of joint bolt improves the lining stiffness, which enlarges the internal forces and reduces the tunnel deformation. As such, the reliability of the tunnel with respect to ULS decreases with the diameter of the joint bolt, and the reliability of the tunnel with respect to SLS increases with the diameter of the joint bolt.

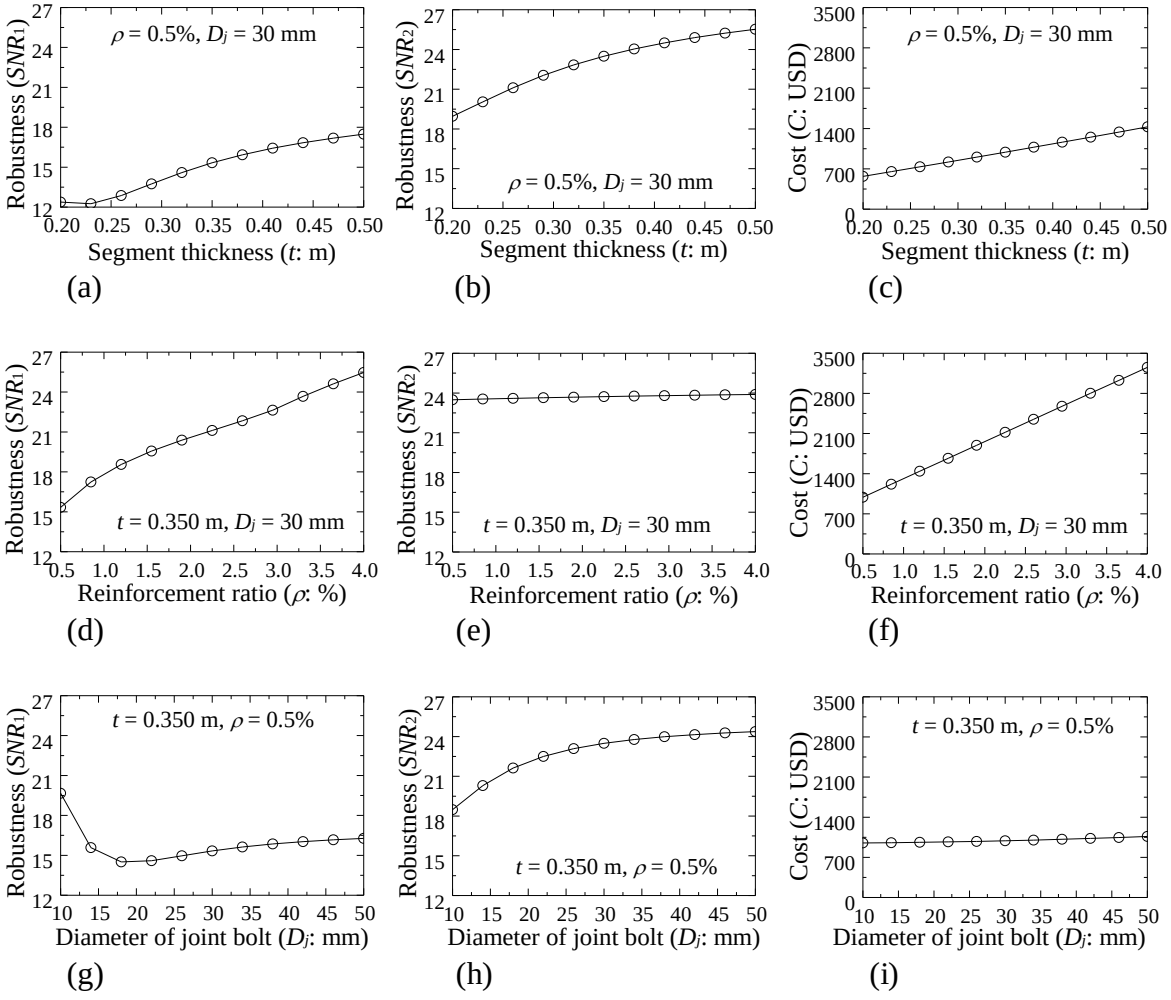

Figure 4.9: Tunnel performance: Robustness versus design parameters and material cost versus design parameters: (a) SNR_1 versus t; (b) SNR_2 versus t; (c) C versus t; (d) SNR_1 versus ρ; (e) SNR_2 versus ρ; (f) C versus ρ; (g) SNR_1 versus D_j; (h) SNR_2 versus D_j; (i) C versus D_j

Similarly, the effects of the design parameters on the robustness and cost of shield-driven tunnel are investigated, and the results are illustrated in Figure 4.9. As the design robustness is always positively correlated with the safety in this example, following findings are found, as expected: the increase of segment thickness can significantly improve the robustness in case of ULS (SNR_1 in Figure 4.9a) and the robustness in case of SLS (SNR_2 in Figure 4.9b); the increase of the reinforcement ratio can greatly enhance the robustness in case of ULS (SNR_1 in Figure 4.9d), while its effect on the robustness in case of SLS is not evident (SNR_2 in Figure 4.9e); the increase of the diameter of joint bolt can raise the robustness in case of SLS (SNR_2 in Figure 4.9h), while its effect on the robustness in case of ULS is negative when $D_j < 20$ mm and slightly positive when $D_j > 20$ mm (SNR_1 in Figure 4.9g). The effects of the design parameters on the cost of shield-driven tunnel design are depicted in Figure 4.9(c), 4.9(f), and 4.9(i), respectively. It is observed that the material cost increases with the increase in each of the three design parameters, although the effect of the diameter of joint bolt is not as significant as the other two parameters.

The results of these sensitivity analyses offer an insight on the design parameters and their effects on the safety, robustness, and cost of a shield-driven tunnel. This forms the basis for the RGD of shield-driven tunnels.

Robust geotechnical design (RGD) of shield-driven tunnel

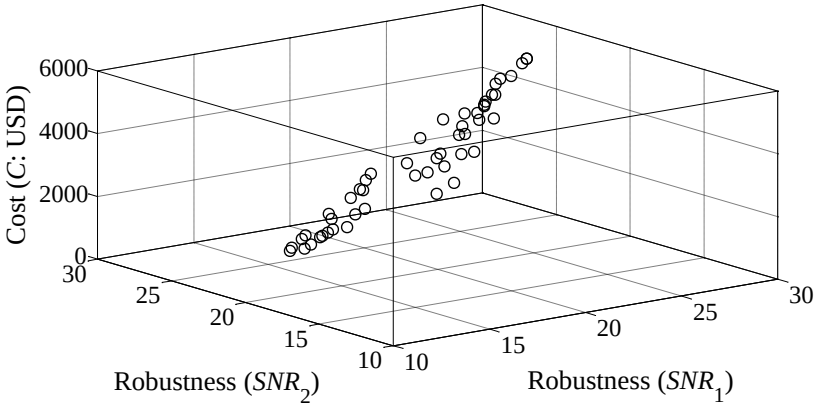

(a)

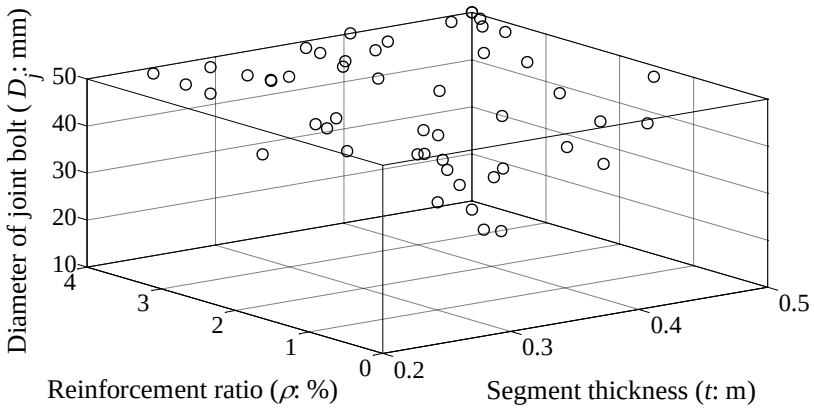

(b)

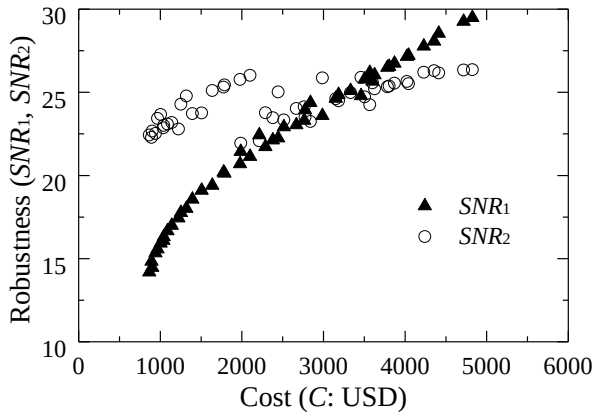

(c)

Figure 4.10: Pareto front obtained using NSGA-II: (a) All non-dominated solutions (Pareto front) shown in 3-D graph of objectives; (b) Design parameters of all non-

dominated optimal solutions; (c) Robustness versus cost of all non-dominated optimal solutions (2-D Pareto front)

As discussed previously, the RGD of a shield-driven tunnel may be set up as a multi-objective optimization problem. With the aid of the Non-dominated Sorting Genetic Algorithm version II (NSGA-II) (Deb et al. 2002), the RGD of a shield-driven tunnel can be carried out using the algorithm shown in Figure 4.7(b). In NSGA-II, the population size is set at 50 and the generation number is set at 100, which yields a converged Pareto front.

Figure 4.10(a) shows the obtained Pareto front (a set of non-dominated optimal designs) with the three objectives, robustness SNR_1, robustness SNR_2 and material cost (C). The design parameters, segment thickness (t), steel reinforcement ratio (ρ) and diameter of joint bolt (D_j) of these non-dominated optimal designs on the Pareto front are shown in Figure 4.10(b). Furthermore, Figure 4.10(c) depicts the 2-D Pareto fronts that are the projections of the 3-D Pareto front, showing the trade-off relationships between robustness (both SNR_1 and SNR_2) and cost (C) in 2-D graphs. Both SNR_1 and SNR_2 tend to increase as the cost increases, indicating the robustness of the design can be enhanced through more investment. The trade-off relationship (trend line) between SNR_1 and C appears more pronounced than the trade-off relationship between SNR_2 and C. In Figure 4.10(c), the values of SNR_1 and SNR_2 are in the range of 13-30 and 22-27, respectively, which are consistent with those observed in Figure 4.9. Such range values represent the possible values of SNR_1 and SNR_2 within the design space. Thus, the observed more obvious trade-off effect between SNR_1 and cost is most likely due to the fact that there is larger variation of SNR_1 in the design space. While the less pronounced trade-off

relationship between SNR_2 and cost suggests that the SNR_2 involves less variability in the design space, this does not necessarily imply that the SNR_2 does not affect the optimal design. Indeed, the Pareto front is a surface which is a function of SNR_1, SNR_2, and cost simultaneously, as shown in Figure 4.10(a). However, the phenomenon observed in Figure 4.10 could be problem specific. In other problems, the SNR_2 may play a more important role in the design optimization.

As all points on the Pareto front are non-dominated optimal designs, the most preferred design can be selected by the designer based on the desired level of cost or robustness. For example, if the desired level of robustness is set at SNR = 15, then the least cost design is taken as the most preferred design, which is defined in this case by the following set of design parameters: t = 274.0 mm, ρ = 0.72 %, and D_j = 45.7 mm.

Summary

This chapter presents a fuzzy set-based robust geotechnical design (RGD) of tunnel segment rings (or tunnel cross sections). Unlike the traditional geotechnical design methodologies, robustness is explicitly considered in the design, in addition to safety and cost efficiency. Within the RGD framework, multi-objective optimization is carried out, in which the level of safety is compulsorily brought to the target level serving as constraints, while the design robustness is maximized and the cost is minimized.

CHAPTER FIVE

IMPROVED SHIELD TUNNEL DESIGN METHODOLOGY INCORPORATING DESIGN ROBUSTNESS*

Introduction

Benefiting from the advances of shield-driven machines and tunneling technologies, shield tunneling has gained world-wide popularity in the construction of tunnels in urban areas (Gong et al. 2014b); however, the methodologies for the design of the lining of shield tunnels have not been improved much during the past decades. The current practice in the design of the lining of shield tunnels is still based upon the analysis of critical cross sections adopting a plane strain assumption, although the analysis methods have evolved from empirical models to mechanics-based models (Wood 1975; ITA 2000; Bobet 2001; Lee et al. 2001; Lee and Ge 2001; Koyama 2003). The longitudinal length of a shield tunnel is generally in the hundreds (or thousands) of meters while the diameter is usually less than 10 m; as such, the analysis and design of the shield tunnel should be a three-dimensional (3-D) problem instead of a 2-D plane strain problem. Furthermore, the effect of the longitudinal variation of input parameters (e.g., soil parameters, ground water table and overburden) may not be inconsequential. The longitudinal variation of input parameters may be attributed to many factors such as

---

*A similar form of this chapter has been submitted to a journal at the time of writing: Gong, W., Huang, H., Juang, C., Atamturktur, S., and Brownlow, A. (2014). "Improved shield tunnel design methodology incorporating design robustness". Canadian Geotechnical Journal (under review).

the longitudinal variation of tunnel alignment, spatial variation of soil parameters, and nearby tunneling activities.

Because of the effect of the longitudinal variation, the *performance* of a shield tunnel, referred to herein as the structure safety and serviceability of each and every segment ring, may not be correctly reflected in the results of the analysis of a few "representative" segment rings (or cross sections). Moreover, the selection of these representative tunnel cross sections can be quite subjective; different designers may have different selections. Therefore, a more rational model for analysis and design of shield tunnels that can consider the longitudinal variation of input parameters is needed.

For a shield tunnel with input parameters that are subjected to longitudinal variation, its performance cannot be evaluated with certainty. Even if the longitudinal variation of input parameters can be accurately characterized, which is rarely the case, different segment rings may exhibit different factors of safety, with respect to either structure safety or serviceability. Thus, an improved design methodology for shield tunnels is proposed in this paper to account for the longitudinal variation of input parameters.

In the proposed design methodology, the longitudinal variation of input parameters is simulated with random field theory, in which the input parameters for tunnel design are generated with Monte Carlo simulation (MCS). The generated input parameters are then used to analyze the tunnel longitudinal behavior, including tunnel settlement, longitudinal rotation, longitudinal bending moment, and longitudinal shear force. In this paper, such analysis is performed using finite element method (FEM) based

upon the Winkler elastic foundation theory (Huang et al. 2014). The obtained tunnel longitudinal responses, as well as the simulated input parameters for tunnel design, are then used to investigate the structure safety and serviceability of each and every segment ring. For the analysis of the structure safety and serviceability, the simplified method developed in Gong et al. (2014d) is adopted, which explicitly considers both shearing effect (Liao et al. 2005) and flattening effect (Huang et al. 2012).

Furthermore, to reduce the effect of input parameters uncertainty in the tunnel design, a recently developed robust geotechnical design methodology (Juang et al. 2013 & 2014; Wang et al. 2013; Gong et al. 2014b & 2014c) is adapted herein for the design of shield tunnels. Although the robust design of shield tunnels was reported previously (Gong et al. 2014b), it was limited to the design of one segment ring. In the present study, the focus is on the design of the tunnel longitudinal structure that consists of a number of segment rings, and the variation of the input parameters in the longitudinal direction is explicitly considered.

In the context of robust design, the input parameters are classified into two categories: the input parameters that can be easily adjusted or controlled by the designer, and the input parameters that are associated with the longitudinal variation and are hard-to-control. The former is termed design parameters while the latter is termed noise factors herein. The robust design of a shield tunnel is usually implemented as a multi-objective optimization problem, as the objectives of the design are to satisfy the tunnel performance requirements (i.e., structure safety and serviceability), and to increases the cost efficiency and design robustness of the design simultaneously. Note that the design

robustness is herein referred to the insensitivity of the design against the unforeseen longitudinal variation of noise factors. As an improvement to the previously reported robust geotechnical design methodology (Gong et al. 2014b), a new design robustness measure is developed, which enables an efficient treatment of the longitudinal variation of noise factors within the robust design framework.

In the rest of this paper, a new framework for the shield tunnel performance analysis that considers the longitudinal variation of input parameters is presented, followed by the formulation of the new design robustness measure and robust design methodology for shield tunnels. Thereafter, a hypothetical example of the improved robust design of a shield tunnel is presented to demonstrate its effectiveness.

New Framework for Shield Tunnel Performance Analysis

While it has long been acknowledged that the longitudinal variation of input parameters must be explicitly considered in the analysis and design of shield tunnels (ITA 2000; ATRB 2000; Koyama 2003), a convincing solution model for shield tunnel performance analysis that considers the longitudinal variation of input parameters is not available. In this paper, we develop a simple framework for such shield tunnel performance analysis. In reference to Figure 5.1, this framework can be outlined in the following steps:

Step 1: Generating input parameters with Monte Carlo simulation

Random field theory is employed herein to model the longitudinal variation, or the spatial variation in the longitudinal domain, of input parameters for tunnel design

(e.g., soil parameters, ground water table, and overburden). The use of random field theory to simulate the spatial variation (in the longitudinal domain) of tunnel input parameters is inspired by the fact that the spatial variation of soil parameters is often simulated with random field in geotechnical engineering (Baker 1984; Phoon and Kulhawy 1999; Fenton and Griffiths 2002; Fenton and Griffiths 2003; Cho 2007; Luo et al. 2012). In this paper, the design parameters of a shield tunnel along the longitudinal direction are generated using Monte Carlo simulation (MCS).

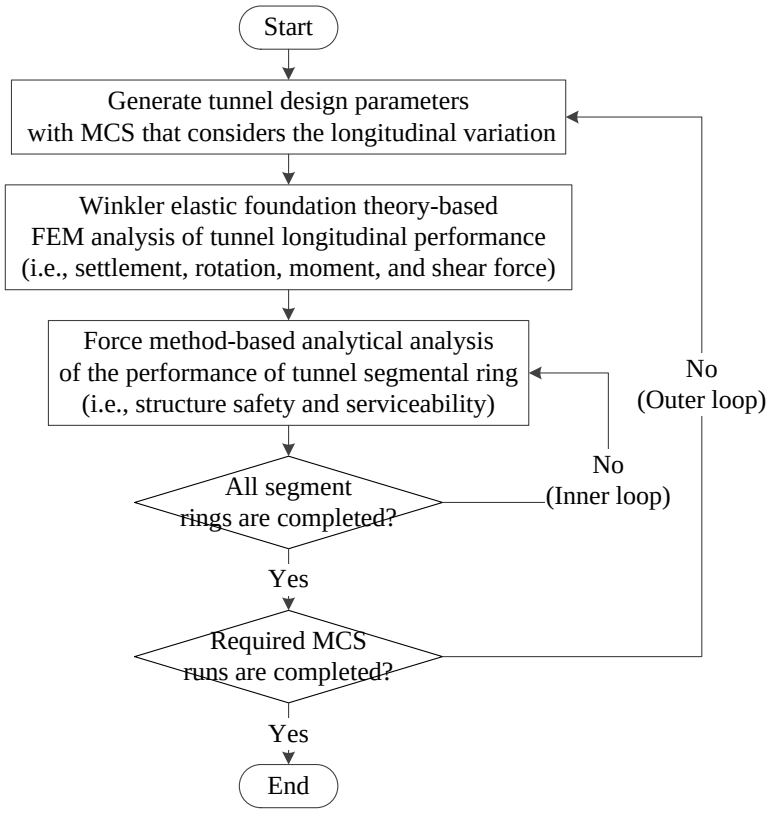

Figure 5.1: Framework for shield tunnel performance analysis

Note that a prerequisite for the generation of tunnel input parameters with MCS is the availability of the statistical information (i.e., mean μ, coefficient of variation δ, scale

of fluctuation r, and distribution type) of these input parameters. The statistical information of the input parameters should be carefully characterized using data from site exploration, published literature, and local experience. For illustration purpose, only the longitudinal variation of the following input parameters are studied in this paper: vertical ground stiffness (k_v), horizontal ground stiffness (k_h), effective cohesion (c), effective friction angle (ϕ), ground water table (H_W) and ground surcharge (q_0).

Step 2: Analyzing tunnel longitudinal response with Winkler elastic foundation theory

Based upon the input parameters, including the vertical ground stiffness of the ground under the tunnel (k_v), ground water table (H_W) and ground surcharge (q_0), along the tunnel longitudinal direction that are generated in Step 1, the longitudinal response of the shield tunnel, including settlement (w), longitudinal rotation (θ_L), longitudinal bending moment (M_L) and longitudinal shear force (Q_L), is readily analyzed in this step using the simplified finite element method (FEM) that is based upon Winkler elastic foundation theory (Huang et al. 2014). Here, the longitudinal structure of the shield tunnel is modeled as an elastic and continuous beam, and the effect of the longitudinal joints, which are the joints between segment rings, is simulated by a reduction factor of tunnel longitudinal flexural stiffness, denoted as ζ (Liao et al. 2008). The soil-structure interaction between the tunnel beam and the ground under the tunnel is modeled with the Winkler elastic foundation model, in which the vertical ground stiffness (k_v) of the ground under the tunnel is depicted with the coefficient of the vertical subgrade reaction (Winkler 1867; Horvath 1983; Lin et al. 1998; Sadrekarimi and Akbarzad 2009).

Step 3: Analyzing the performance of segment ring with force method

Based upon the tunnel input parameters, including the horizontal ground stiffness (k_h), effective cohesion (c), effective friction angle (ϕ), ground water table (H_W) and ground surcharge (q_0) along the longitudinal direction that are generated in Step 1 and the tunnel longitudinal response that is analyzed in Step 2, the performance (i.e., structure safety and serviceability) of a tunnel segment ring of concern is evaluated in this step using the force method (Lee et al. 2001; Gong et al. 2014d). Here, the effect of tunnel longitudinal behavior on the performance of tunnel segment ring is studied considering the shearing effect (Liao et al. 2005) and the flattening effect (Huang et al. 2012). The effective earth pressure concept is used in this paper to compute the earth pressure and the pore water pressure on the shield tunnel.

The results of the force method are the internal forces (i.e., axial force N, bending moment M, and shear force Q) and the convergence deformations (i.e., vertical convergence deformation Δ_v and horizontal convergence deformation Δ_h) of the tunnel lining, which are then used to assess the performance of the tunnel segment ring. Here, the internal forces are used to calculate the factor of safety with respect to the structure safety, denoted as Fs_1, using the limit state design method (ITA 2000; Gong et al. 2014b); and the convergence deformations are used to compute the factor of safety with respect to the serviceability, denoted as Fs_2, using the procedure proposed by Gong et al. (2014b) based on a limiting convergence deformation of the tunnel lining of 0.6%D (D denotes the outer diameter of the tunnel lining).

Step 4: Repeating the performance analysis in Step 3 for all tunnel segment rings

In this step, the performance analysis of the tunnel segment ring presented in Step 3 is repeated for each and every segment ring of the shield tunnel, as shown with the inner loop in Figure 5.1. This will yield a series of factors of safety (with respect to either structure safety or serviceability), as different segment rings can exhibit different factors of safety due to the existence of the longitudinal variation of input parameters. Thus, the mean values of the factors of safety, denoted as μ_{Fs1} and μ_{Fs2}, are obtained to represent the overall performance of the shield tunnel with respect to the structure safety and serviceability, respectively; whereas, the standard deviations of the factors of safety, denoted as σ_{Fs1} and σ_{Fs2}, are computed to reflect the variation (or degree of uncertainty) of the tunnel performance with respect to the structure safety and serviceability, respectively.

Step 5: Repeating MCS runs to yield a converged solution of tunnel performance

In this step, the performance analysis procedures of the shield tunnel presented in Step 1, Step 2, Step 3, and Step 4 are repeated for a specified number of MCS runs such that a converged solution of tunnel performance can be achieved, as shown with the outer loop in Figure 5.1. Note that different overall factors of safety (i.e., μ_{Fs1} and μ_{Fs2}) and variations of factors of safety (i.e., σ_{Fs1} and σ_{Fs2}) can be obtained with different MCS runs. Therefore, a certain number of MCS runs, which is determined through a trial-and-error analysis, should be carried out to derive a converged solution of tunnel performance.

Robust Design Methodology of Shield Tunnels

A new design robustness measure is proposed in this paper for the robust design of shield tunnels that considers the longitudinal variation of input parameters. The formulation of the new design robustness measure and the complete multi-objective optimization-based robust design methodology are presented in the following.

New design robustness measure for shield tunnels

One key element in the robust design of shield tunnels is the measure of design robustness. Although the exiting design robustness measures, such as the variation of the failure probability of the designed system (Juang et al. 2013; Wang et al. 2013), the standard deviation of the system performance (Juang et al. 2014), the signal-to-noise ratio (*SNR*) of the system performance (Gong et al. 2014b) and the gradient-based sensitivity index of the system performance (Gong et al. 2014c), were shown effective in many geotechnical problems, they are not suitable for the robust design of shield tunnels that involve the longitudinal variation of input parameters. In this paper, the signal-to-noise ratio (*SNR*) of the factor of safety (Fs), defined below (Gong et al. 2014b), is adapted for the robust design of shield tunnels such that it can consider the longitudinal variation of input parameters.

$$SNR = 10\log_{10}\left(\frac{\mu_{\mathrm{Fs}}{}^{2}}{\sigma_{\mathrm{Fs}}{}^{2}}\right) \tag{5.1}$$

where μ_{Fs} and σ_{Fs} are the mean and standard deviation of the factor of safety (with respect to the tunnel performance), respectively, which are readily computed using the procedure described in Step 4 in the previous section. Intuitively, a higher *SNR* signals a lower variability of the tunnel performance (in terms of the factor of safety) and, thusly, a higher design robustness.

As mentioned previously, different MCS runs can result in different values of μ_{Fs} and σ_{Fs}. The variation in μ_{Fs} and σ_{Fs} further leads to the uncertainty in the computed *SNR*. In such a circumstance, a new design robustness measure (*R*), which is based upon the statistics of the *SNR*, is defined as follows and used to measure the design robustness of shield tunnels:

$$R = \mu_{SNR} - 2\sigma_{SNR} \tag{5.2}$$

where μ_{SNR} and σ_{SNR} are the mean and standard deviation of the *SNR* with respect to the tunnel performance, respectively, which are readily computed using the procedure described in Step 5 in the previous section.

It is noted that the robustness measure *R* defined here is basically the same as *SNR*; thus, higher *R* value indicate higher design robustness. The rationale to adopt the mean minus two standard deviations is to be able to consider the variation of *SNR* among those obtained with different MCS runs. Approximately, the robustness measure *R* may be thought of as the lower end of the *SNR* in face of the longitudinal variation of input parameters (noise factors).

Multi-objective optimization: design robustness versus cost efficiency

The goal of the robust design is to find an *optimal* design from the design space (***DS***), which is represented by a set of easy-to-control design parameters (***d***), such that the system response (or performance) is robust against the longitudinal variation of hard-to-control noise factors ($\boldsymbol{\theta}$). The desire to maximize the design robustness (R), however, must be balanced with the desire to minimize the cost (C), while satisfying the performance requirements, in terms of $g(\boldsymbol{d}, \boldsymbol{\theta}) > 0$ (Juang et al. 2013 & 2014; Wang et al. 2013; Gong et al. 2014b & 2014c). In other words, the robust design of shield tunnels can be effectively formulated as a multi-objective optimization problem, as shown in Figure 5.2.

Find:	$\boldsymbol{d}$ ($\boldsymbol{d}$ denotes a set of easy-to-control design parameters)
Subject to:	$\boldsymbol{d} \in \boldsymbol{DS}$ ($\boldsymbol{DS}$ denotes the design pool)
	$g(\boldsymbol{d}, \boldsymbol{\theta}) > 0$ ($g > 0$ denotes the performance requirement)
Objectives:	minimize $C(\boldsymbol{d})$ (C denotes the cost)
	maximize $R(\boldsymbol{d}, \boldsymbol{\theta})$ (R denotes the design robustness)

Figure 5.2: Multi-objective optimization setting of robust design

The optimization setting illustrated in Figure 5.2 indicates that the performance requirement (g) and design robustness (R) can be expressed as a function of the easy-to-control design parameters (***d***) and hard-to-control noise factors ($\boldsymbol{\theta}$), while the cost (C) is determined with only the design parameters (***d***). Thus, the multi-objective optimization-based robust design can be effectively realized by adjusting the design parameters (***d***).

In general, the desire to maximize the design robustness and the desire to minimize the cost are two conflicting objectives. As such, the multi-objective optimization, as illustrated in Figure 5.2, in unlikely to yield a single best design; rather, it usually yields a set of non-dominated optimal designs. These non-dominated optimal designs collectively form a Pareto front that shows a tradeoff relationship between design robustness and cost efficiency. The Pareto front can usually be obtained through some optimization algorithms, such as the non-dominated sorting genetic algorithm version II (NSGA-II) (Deb et al. 2002).

As a tradeoff relationship between design robustness and cost efficiency, the Pareto front can aid in making an informed design decision. For example, either the least cost design that is above a pre-specified level of design robustness (R_T) or the most robust design that falls within a pre-specified cost level (C_T) could be identified as the most preferred design in the given design space. The selection of an optimal level of design robustness or cost, however, may be problem specific and involves many factors. Alternatively, when no design preference is specified by the owner, the knee point on the Pareto front, which represents the best compromise between design robustness and cost efficiency, may be taken as the most preferred design (Juang et al. 2014; Gong et al. 2014c).

Case Study

To demonstrate the new framework for shield tunnel performance analysis and the proposed robust design methodology for shield tunnels, a hypothetical illustrative

example of the robust design of a shield tunnel with a longitudinal length of 300 m is presented herein.

Parameters setting in the illustrative example

In the robust design of shield tunnels, the input parameters are first classified into two categories: easy-to-control design parameters ($\boldsymbol{d}$) and hard-to-control noise factors ($\boldsymbol{\theta}$). Note that the design parameters are the input parameters that can be easily adjusted by the designer, such as the segment thickness (t), diameter of steel bolts (i.e., D_c and D_l for the circumferential bolts and longitudinal bolts, respectively) and reinforcement ratio of tunnel segment (ρ); the noise factors ($\boldsymbol{\theta}$) are the input parameters that cannot be adjusted by the designer or characterized with certainty, such as the vertical ground stiffness (k_v), horizontal ground stiffness (k_h), effective cohesion (c), effective friction angle (ϕ), ground water table (H_W) and ground surcharge (q_0). For simplicity, the stationary random field theory is used herein to model the longitudinal variation of noise factors ($\boldsymbol{\theta}$). Detailed statistics of the noise factors are assumed and listed in Table 5.1. The statistics are assumed for illustration purpose; for real-world application, these statistics should be carefully characterized based on site exploration, published literature, and local experience.

For ease of illustration, the unit weight of soil (γ_s), material parameters of the precast tunnel segment and steel (i.e., reinforcement of tunnel segment and bolts), and the geometries of the precast tunnel segment are assumed as constants, since the variability of each of these parameters is relatively low and negligible. The embedded depth (H), a

vertical distance that is measured from the tunnel crown to the ground surface, is also assumed as a constant and not varying along the longitudinal direction. Detailed parameters settings of these deterministic parameters are listed in Table 5.2.

Table 5.1: Statistical characterization of noise factors

Noise factors	Mean (μ)	Coefficient of variation (δ)	Scale of fluctuation (r)	Distribution
Vertical ground stiffness of the ground under the tunnel (k_v, kN/m^3)	33000	0.500	50	Lognormal
Effective cohesion of soil (c, kN/m^2)	7.5	0.333	50	Lognormal
Effective friction angle of soil (ϕ, °)	32.65	0.027	50	Lognormal
Horizontal ground stiffness of soil (k_h, kN/m^3)	9250	0.207	50	Lognormal
Ground water table (H_W, m)	1.25	0.200	50	Lognormal
Ground surcharge (q_0, kN/m^2)	10	0.333	50	Lognormal

Table 5.2: Deterministic parameters of the example tunnel

Category	Parameter	Value
Soil	Unit weight (γ_s, kN/m^3)	18.0
Tunnel geometries	Longitudinal length (L, m)	300.0
	Embedded depth (H, m)	14.0
	Tunnel inner radius (R_{in}, m)	2.75
	With of segment ring (b, m)	1.0
	Position of circumferential joints of half structure (φ_i, °)	8, 73, 138
Tunnel segment	Unit weight of concrete (γ_c, kN/m^3)	25.0
	Elastic modulus of concrete (E_c, kN/m^2)	34.5×10^6
	Compression strength of concrete (f_c, kN/m^2)	39×10^3
	Ultimate plastic strain of concrete (ε_p)	0.0033
Steel reinforcement	Elastic modulus of steel (E_s, kN/m^2)	210×10^6
	Yielding strength of steel (f_y, kN/m^2)	345×10^3
	Thickness of protective concrete cover (a, m)	0.05
Steel bolt	Length of steel bolts (l_b, m)	0.4
	Number of bolts at each circumferential joint	2
	Distance from bolts center to tunnel inside surface (h)	t/3
	Number of steel bolts between adjacent segment rings (or of each longitudinal joint)	17

Effectiveness of the new framework for shield tunnel performance analysis

With the statistics of the noise factors listed in Table 5.1, the performance of the example shield tunnel can be readily analyzed using the new framework for shield tunnel performance analysis presented previously. Shown in Figure 5.3 are the input parameters (noise factors) along the longitudinal direction that are generated from one MCS run. It is noted that the noise factors vary distinctly in the longitudinal domain, and thus the determination of the critical tunnel cross sections of this shield tunnel can be a great challenge. In this paper, the longitudinal response of this shield tunnel is analyzed using a simplified FEM method that is founded on Winkler elastic foundation theory (Huang et al. 2014). The results of the analysis, including tunnel settlement (w), longitudinal rotation (θ_L), longitudinal bending moment (M_L) and longitudinal shear force (Q_L), are plotted in Figure 5.4.

Significant longitudinal variation of tunnel longitudinal responses is observed, as shown in Figure 5.4. Further, the longitudinal variation of the tunnel performance (in terms of the structure safety and serviceability of segment ring) could be resulted in. Shown in Figure 5.5 is the longitudinal variation of the tunnel performance, in terms of Fs_1 (with respect to the structure safety of segment ring) and Fs_2 (with respect to the serviceability of segment ring), given the longitudinal variation of noise factors in Figure 5.3. Figure 5.5 indicates that different segment rings of this shield tunnel exhibit different tunnel performances, which is reflected in the longitudinal variation of the factors of safety (i.e., Fs_1 and Fs_2). Thus, the performance of this shield tunnel cannot be assessed with the results of the analysis of a few segment rings. Note that the design parameters of

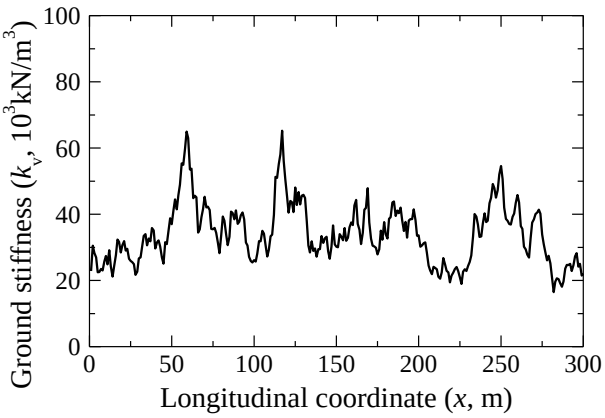
Ground stiffness (k_v, 10^3kN/m^3)
Longitudinal coordinate (x, m)

(a)

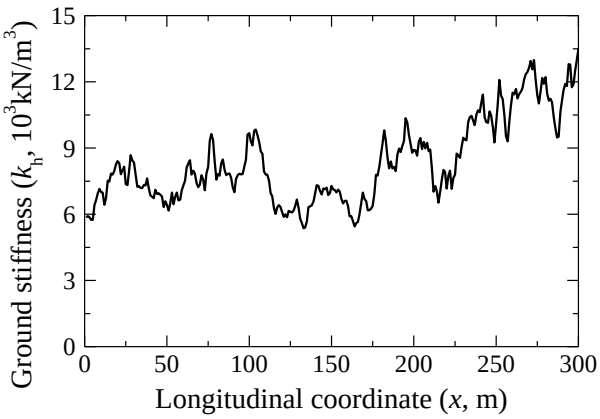
Ground stiffness (k_h, 10^3kN/m^3)
Longitudinal coordinate (x, m)

(b)

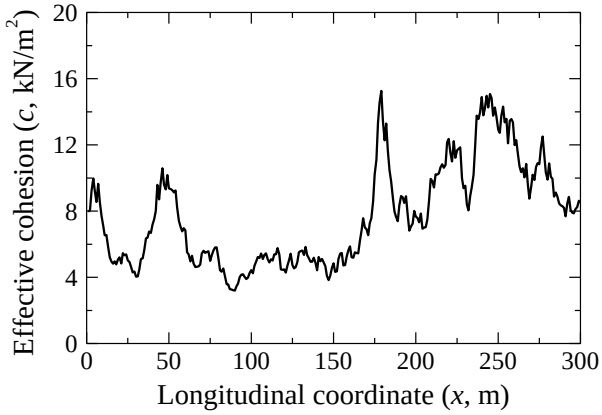
Effective cohesion (c, kN/m^2)
Longitudinal coordinate (x, m)

(c)

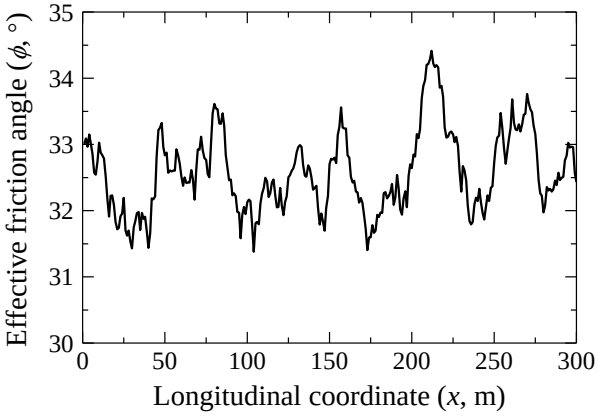
Effective friction angle (ϕ, °)
Longitudinal coordinate (x, m)

(d)

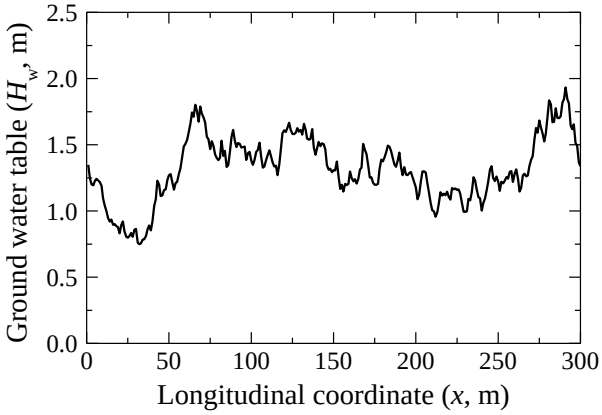
Ground water table (H_w, m)
Longitudinal coordinate (x, m)

(e)

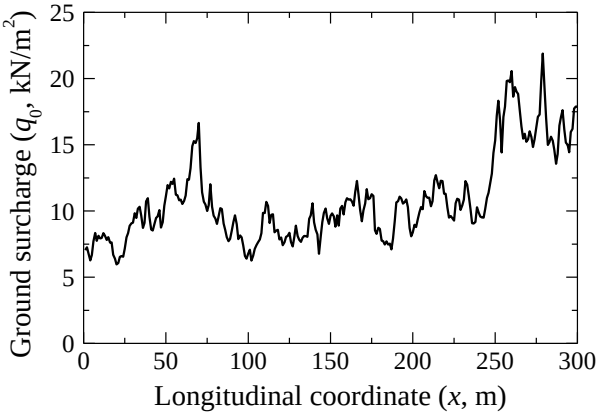
Ground surcharge (q_0, kN/m^2)
Longitudinal coordinate (x, m)

(f)

Figure 5.3: Illustrative longitudinal variation of noise factors: (a) Vertical ground stiffness; (b) Horizontal ground stiffness; (c) Effective cohesion; (d) Effective friction angle; (e) Ground water table; (f) Ground surcharge

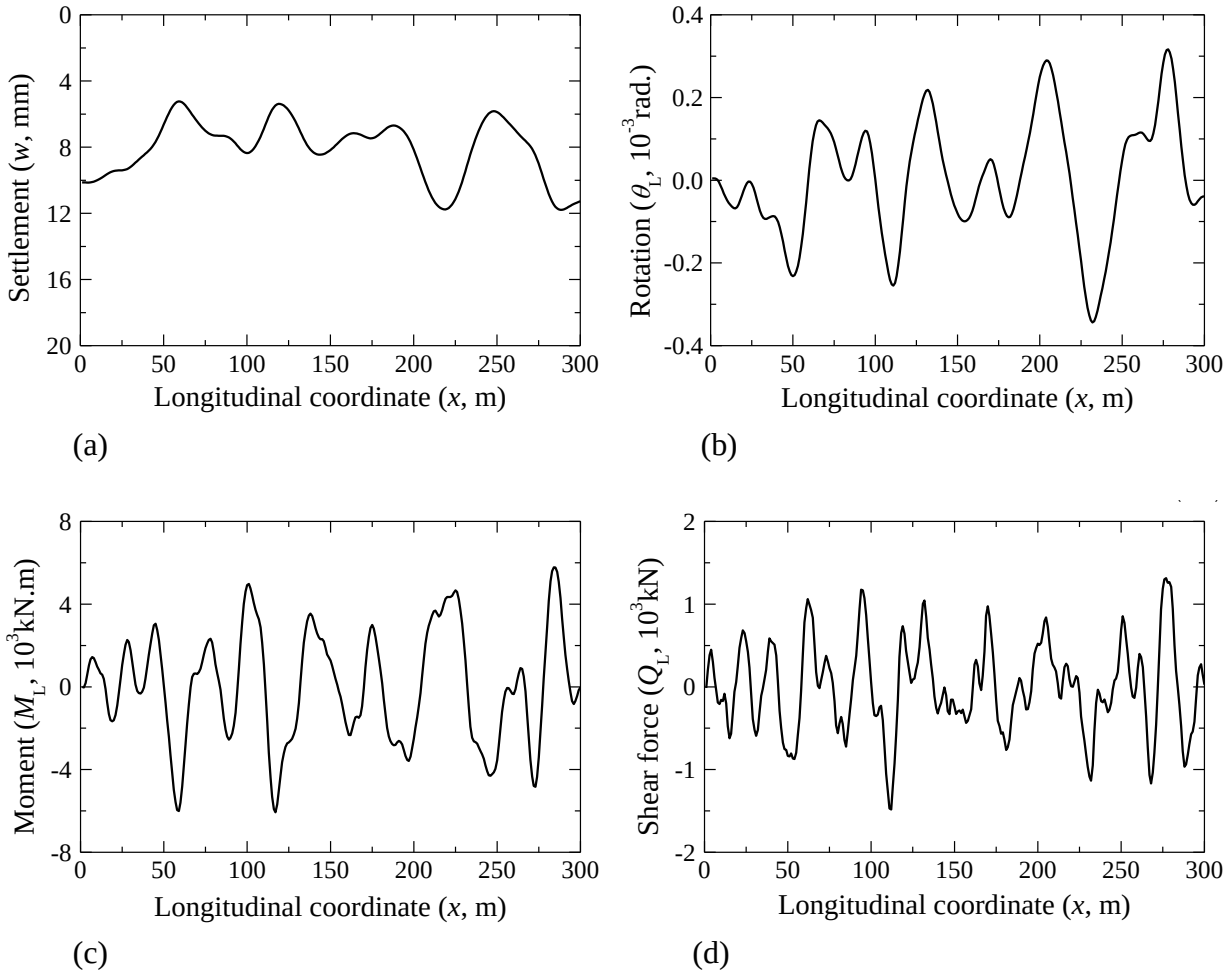

Figure 5.4: Computed tunnel longitudinal responses given the noise factors in Figure 5.3: (a) Settlement; (b) Longitudinal rotation; (c) Longitudinal bending moment; (d) Longitudinal shear force

the shield tunnel are t = 0.35 m, ρ = 0.5%, D_c = 30 mm, and D_l = 30 mm; indeed, this set of tunnel design parameters is used in the metro tunnels in Shanghai, China.

In general, different MCS runs can generate different longitudinal variations of noise factors, and as such, different longitudinal curves of tunnel performance are

expected. The longitudinal curve of tunnel performance in Figure 5.5 is obtained for the variation of noise factors shown in Figure 5.3. Therefore, a series of MCS runs should be carried out to derive a converged solution of tunnel performance, in terms of the overall factors of safety (i.e., μ_{Fs1} and μ_{Fs2}), as per Step 5 of the new analysis framework presented previously. Figure 5.6(a) & 5.6(b) show the computed values of the mean and standard deviation of the overall factors of safety with different MCS runs. It is noted that the converged solution of tunnel performance can be achieved with 500 MCS runs. Figure 5.6(c) & 5.6(d) further show the computed values of the mean and standard deviation of the signal-to-noise ratios (*SNR*) with different MCS runs. Similarly, the converged solution of the mean and standard deviation of the *SNR* can be achieved with 500 MCS runs. Therefore, the number of MCS runs is set at 500 for sampling the longitudinal variation of noise factors.

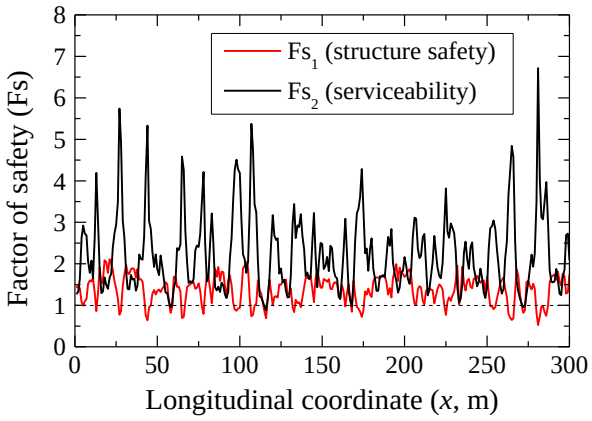

Figure 5.5: Computed tunnel performance given the noise factors in Figure 5.3

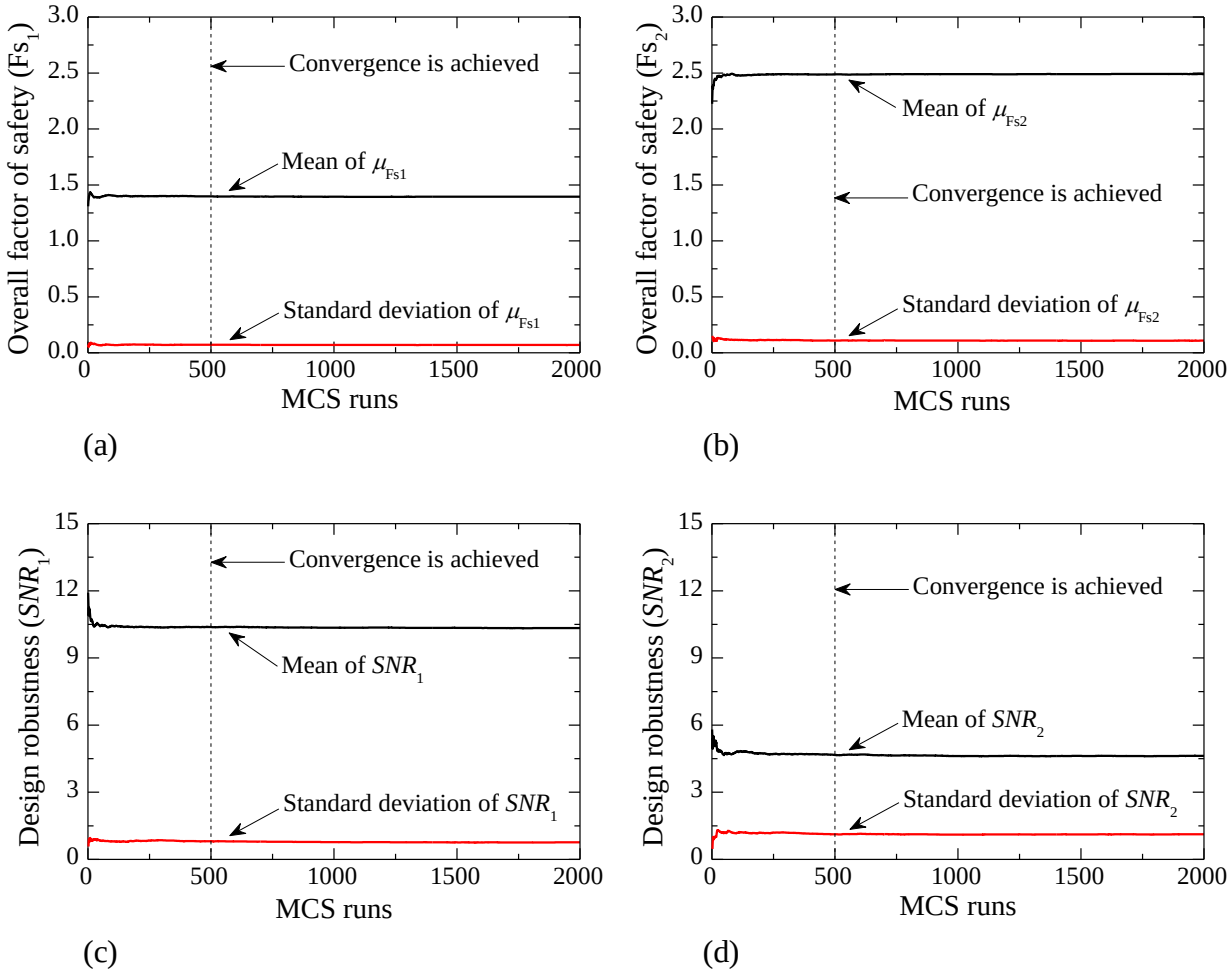

Figure 5.6: Convergence of the overall factors of safety and signal-to-noise ratio with MCS runs: (a) Overall factor of safety for structure safety; (b) Overall factor of safety for serviceability; (c) Signal-to-noise ratio for structure safety; (d) Signal-to-noise ratio for serviceability

As demonstrated in Figure 5.6(a) & 5.6(b), the variations of the overall factors of safety are relatively small and may be neglected. For example, the means of μ_{Fs1} and μ_{Fs2} are 1.39 and 2.49, respectively, while the standard variations of μ_{Fs1} and μ_{Fs2} are 0.07 and 0.11, respectively. Whereas, the variations of the computed *SNR*, as shown in Figure 5.6(c) and 5.6(d), are significantly high and cannot be ignored. For example, the means of SNR_1 and SNR_2 are 10.33 and 4.63, respectively, while the standard variations

of SNR_1 and SNR_2 are 0.77 and 1.12, respectively. As noted, the overall factors of safety (in terms μ_{Fs1} and μ_{Fs2}) and *SNR* (in terms of SNR_1 and SNR_2) of the shield tunnel can be fitted well with normal distributions, as shown in Figure 5.7. Therefore, the means of μ_{Fs1} and μ_{Fs2} are adopted herein to assess the performance requirements of the candidate design of the shield tunnel; and the design robustness of the candidate design is measured with Eq. (5.2). Figure 5.7(c) & 5.7(d) show the computed design robustness, in terms of R_1 and R_2, of the shield tunnel.

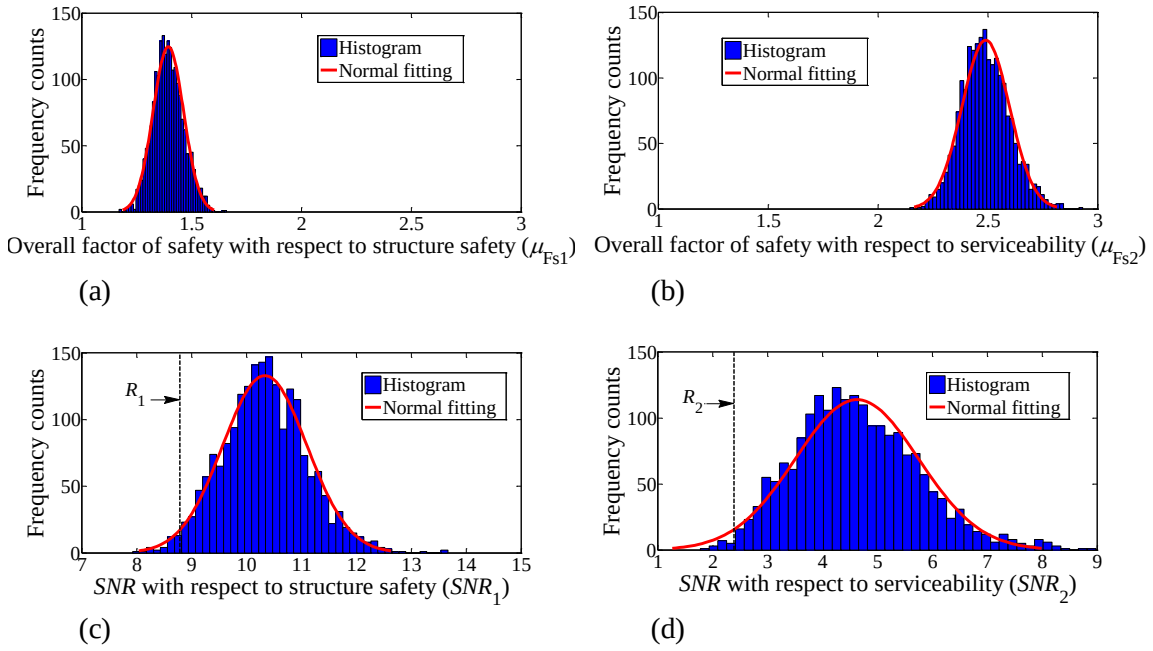

Figure 5.7: Distributions of the overall factors of safety and *SNR* in 2,000 MCS runs: (a) Distribution of μ_{Fs1}; (b) Distribution of μ_{Fs2}; (c) Distribution of SNR_1; (d) Distribution of SNR_2

Finally, the failure probabilities with respect to both structure safety and serviceability of the segment ring of this longitudinal shield tunnel are computed using the new analysis framework presented previously. For the example tunnel, the failure

probabilities for structure safety and serviceability are 2.14×10^{-1} and 2.98×10^{-2}, respectively, based on 2,000 MCS runs (see Figure 5.8a & 5.8b). The large failure probabilities indicate that the exiting shield tunnels in Shanghai may experience significant performance problems, which is quite consistent with the years of structure health monitoring data. However, the failure probabilities of the shield tunnel computed with the conventional tunnel analysis method (Lee et al. 2001) are 4.0×10^{-5} and 0, respectively (see Figure 5.9a & 5.9b). The latter results obtained with the conventional tunnel analysis method are not consistent with the long term observations. Thus, it may be concluded that by considering the longitudinal variation of input parameters, the new analysis framework yields a more accurate prediction of the tunnel performance.

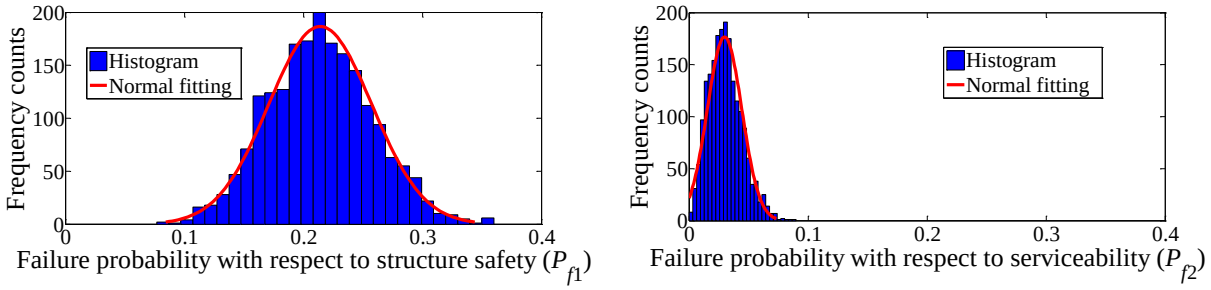

(a) (b)

Figure 5.8: Failure probabilities in 2,000 MCS runs using the advanced solution for shield tunnel performance analysis: (a) Failure probability for structure safety; (b) Failure probability for serviceability

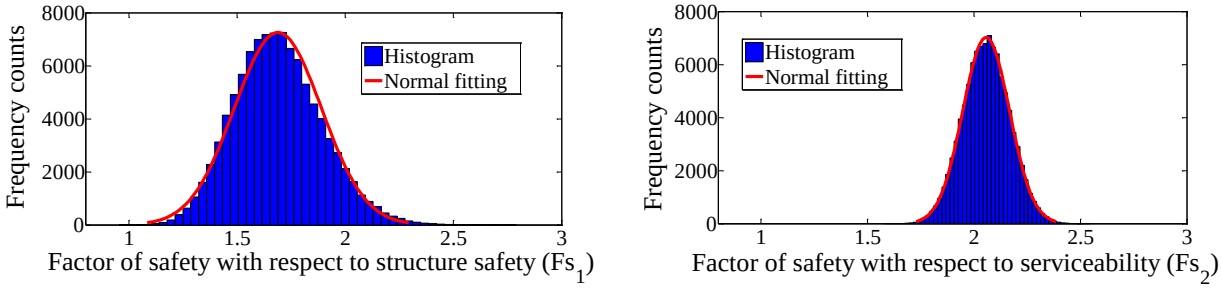

(a) (b)

Figure 5.9: Factors of safety in 100,000 MCS runs using the conventional methods for shield tunnel performance analysis: (a) Factor of safety for structure safety; (b) Factor of safety for serviceability

Easy-to-control design parameters on tunnel performance and design robustness

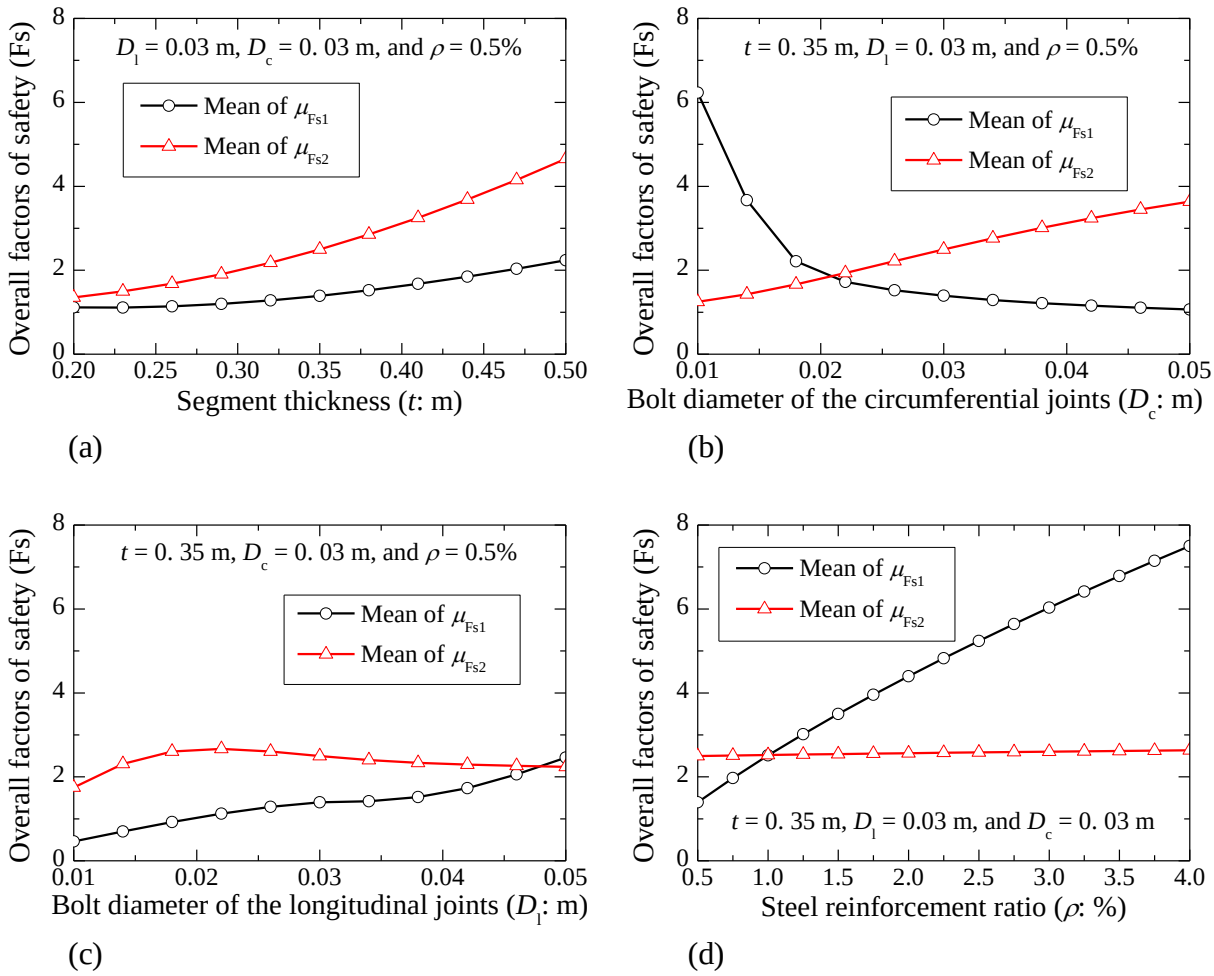

Figure 5.10: Easy-to-control design parameters on tunnel performance: (a) Segment thickness; (b) Bolt diameter of the circumferential joints; (c) Bolt diameter of the longitudinal joints; (d) Steel reinforcement ratio of tunnel segment

In reference to the robust design optimization setting shown in Figure 5.2, the tunnel performance and the design robustness can be expressed as a function of the easy-

to-control design parameters (***d***) and hard-to-control noise factors (***θ***). Thus, a series of parametric analyses are carried out herein to investigate how the tunnel performance, in terms of the mean of μ_{Fs1} and μ_{Fs2}, and the design robustness, in terms of R_1 and R_2, are affected by the adjustment of the design parameters (***d***). This series of parametric studies provides a basis for the robust design of the shield tunnel. The results of the parametric studies are shown in Figure 5.10 & 5.11.

As shown in Figure 5.10(a), the tunnel performance with respect to both structure safety and serviceability (in terms of the mean of μ_{Fs1} and μ_{Fs2}, respectively) increases with the increase of the segment thickness. The shield tunnel structure with a larger segment thickness can, naturally, bear more internal forces and yield less convergence deformation. In Figure 5.10(b), as the bolt diameter of the circumferential joints increases, the tunnel performance with respect to the structure safety decreases significantly, whereas the tunnel performance with respect to the serviceability increases linearly. The plots in Figure 5.10(b) also show that the shield tunnel structure with a larger bolt diameter of the circumferential joints yields a larger internal forces and less convergence deformation. In Figure 5.10(c), as the bolt diameter of the longitudinal joints increases, the tunnel performance with respect to the structure safety improves, while the tunnel performance with respect to the serviceability improves initially and then begins to degrade. However, the variation of tunnel performance due to the adjustment of the diameter of the longitudinal joints is not distinct. The steel reinforcement ratio of tunnel segment can enhance the bearing capacity of tunnel segment rings, but has a minor effect on the circumferential stiffness of tunnel segment rings. Thus, the tunnel performance

with respect to the structure safety improves significantly with the increase of the reinforcement ratio of tunnel segment, while the tunnel performance with respect to the serviceability is hardly affected by the adjustment of the reinforcement ratio of tunnel segment, as depicted in Figure 5.10(d).

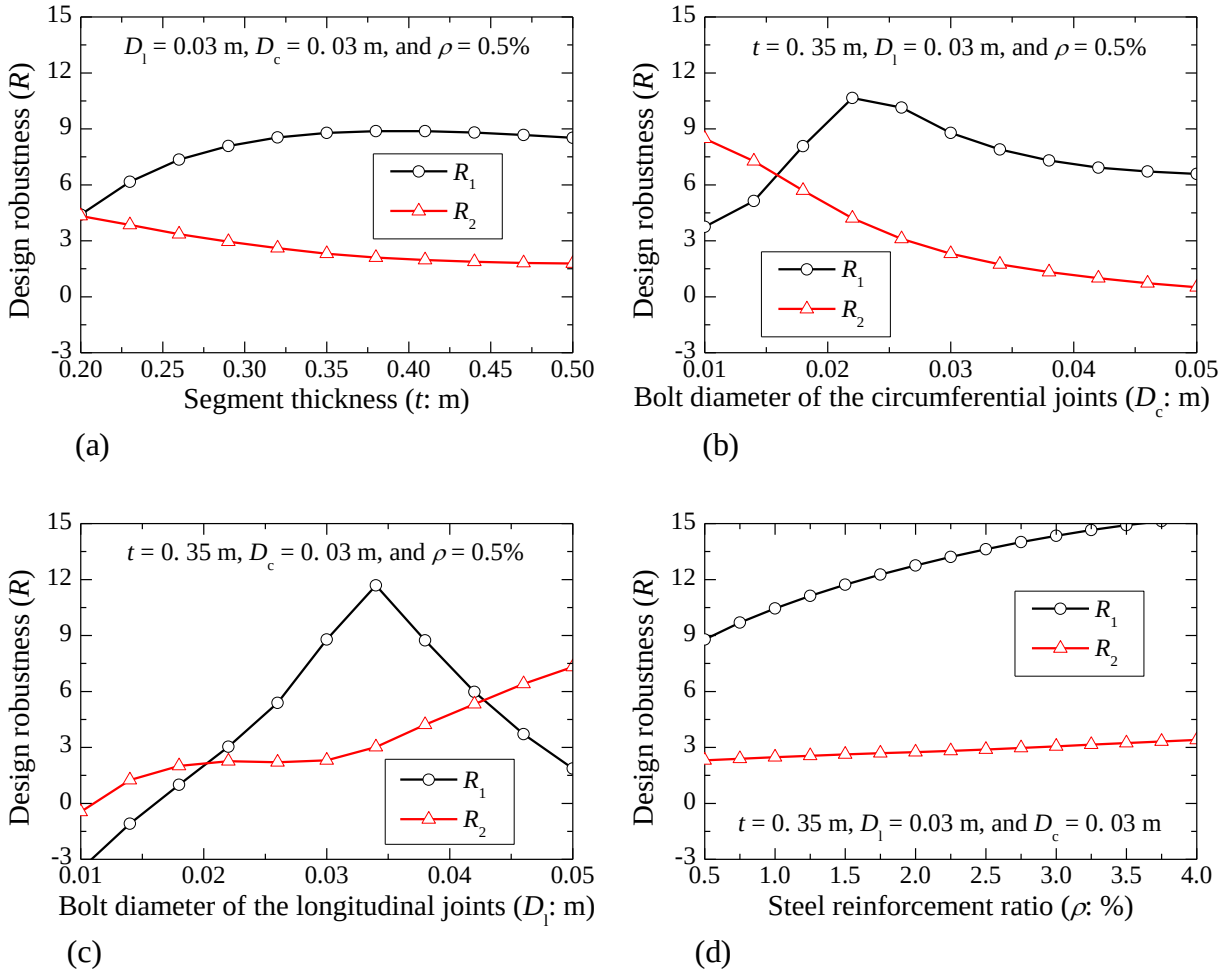

Figure 5.11: Easy-to-control design parameters on tunnel design robustness: (a) Segment thickness; (b) Bolt diameter of the circumferential joints; (c) Bolt diameter of the longitudinal joints; (d) Steel reinforcement ratio of tunnel segment

Figure 5.11 shows the effect of design parameters on the design robustness of the shield tunnel. Figure 5.11(a) illustrates that the increase of the segment thickness

enhances the design robustness of the shield tunnel with respect to the structure safety (indicated by the increase of R_1), but degrades the tunnel design robustness with respect to the serviceability (indicated by the decrease of R_2). The effect of the increase of the segment thickness on the tunnel design robustness becomes less significant as the segment thickness becomes large. As shown in Figure 5.11(b), the increase of the bolt diameter of the circumferential joints always leads to the decrease of tunnel design robustness with respect to the serviceability; whereas the tunnel design robustness with respect to the structure safety increases initially and then begins to decrease. Similarly, the increase of the bolt diameter of the longitudinal joints enhances the tunnel design robustness with respect to the serviceability; whereas the tunnel design robustness with respect to the structure safety increases first and then begins to decrease, as depicted in Figure 5.11(c). Finally, in Figure 5.11(d), the increase of the steel reinforcement ratio of tunnel segment enhances the tunnel design robustness with respect to the structure safety, but the tunnel design robustness with respect to serviceability is hardly affected.

The results of these parametric analyses, shown in Figure 5.10 & 5.11, offer an insight on the effects of the easy-to-control design parameters on the performance and design robustness of shield tunnels. They provide a basis for the robust design of shield tunnels: the robust design of shield tunnels is indeed achieved by a careful adjustment of the design parameters.

Robust design optimization

For illustration purpose, a discrete design space (***DS***) is adopted in this paper. With the ranges of design parameters shown in Table 5.3, this design space has 500

discrete candidate designs. Of course, a continuous design space may be adopted if so desired based on local experience in a real-world application. For the performance requirements (i.e., structure safety and serviceability) of the shield tunnel, the target factors of safety with respect to both structure safety and serviceability are set at 1.5. In other words, the tunnel performance requirements consist of two conditions: the mean of μ_{Fs1} > 1.5 and the mean of μ_{Fs2} > 1.5. As shown in Figure 5.2, the cost of the shield tunnel is also a design objective to be optimized in the robust design optimization. Also for illustration purpose, only the material cost of the shield tunnel is considered herein: the material cost consists of the segment concrete cost, steel reinforcement cost, and joint bolts cost. According to Gong et al. (2014b), the unit prices of the segment concrete, reinforcement steel, and joint bolts in a typical Shanghai metro tunnel are c_c = 600 RMB/m^3 (97.77 USD/m^3), c_s = 4000 RMB/10^{3}kg (645.16 USD/10^{3}kg), and c_b = 10 RMB/kg (1.61 USD/kg), respectively. Thus, the cost function in the robust design of the shield tunnel, denoted as $C(\boldsymbol{d})$ in Figure 5.2, is computed as follows:

$$C(\boldsymbol{d}) = c_c Q_c + c_s Q_s + c_b Q_b \tag{5.3}$$

Table 5.3: Design space of the robust design of the example tunnel

Easy-to-control design parameter	Possible value
Segment thickness (t: m)	{0.25, 0.30, 0.35, 0.40, 0.45}
Steel reinforcement ratio of tunnel segment (ρ: %)	{0.5, 1.0, 1.5, 2.0}
Bolt diameter of the circumferential joints (D_c: mm)	{20, 25, 30, 35, 40}
Bolt diameter of the longitudinal joints (D_l: mm)	{20, 25, 30, 35, 40}

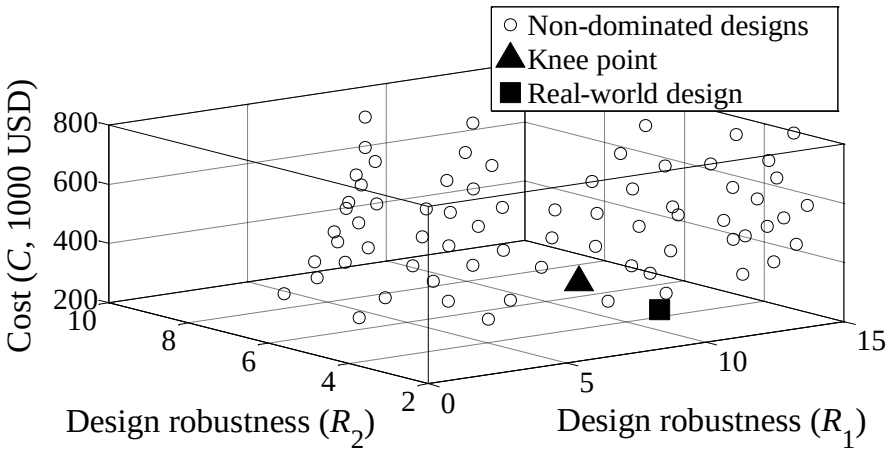

Figure 5.12: Robust design optimization results of the example tunnel

Once the performance (safety) requirements, the cost, and the design robustness of each candidate design in the design space are assessed, the robust design optimization of this shield tunnel is readily carried out according to the robust design optimization setting shown in Figure 5.2. As expected, the robust design optimization yields a series of non-dominated optimal designs, as shown in Figure 5.12, rather than a single best design. It is easily observed that the desire to maximize the design robustness and the desire to minimize the cost are two conflicting objectives. The non-dominated optimal designs collectively form a 3-D Pareto front, since there are three objectives involved in the optimization (i.e., design robustness with respect to the structure safety R_1, design robustness with respect to the serviceability R_2, and cost C.

Oftentimes, a decision can be made based on the Pareto front. Generally, either the least cost design that is above a pre-specified level of design robustness (R_T) or the most robust design that falls within a pre-specified cost level (C_T) may be selected as the most preferred design in the design space. Nevertheless, the determination of an

appropriate level of design robustness or cost could be problem specific. If no design preference is specified by the designer or owner, the knee point on the Pareto front may be taken as the most preferred design (Juang et al. 2014; Gong et al. 2014c). Here, the marginal utility function-based approach (Branke et al. 2004; Gong et al. 2014c) is employed to locate the knee point on the Pareto front, and the identified knee point is plotted in Figure 5.12. Note that on the upper side of the knee point, a slight improvement in the design robustness would significantly increase the cost; whereas, on the other side of the knee point, a slight reduction in cost would require a huge sacrifice in the design robustness.

Also plotted in Figure 5.12 is the actual design adopted by Shanghai metro. It is noted that higher design robustness (indicated by a larger R) and higher cost efficiency (indicated by a lower C) can be achieved with the knee point obtained from the robust design optimization, compared to the actual design in Shanghai. Detailed comparison of these two designs is listed in Table 5.4. In Table 5.4, the feasibility, denoted as f, represents the likelihood that the shield tunnel will not fail with respect to the tunnel performance (i.e., structure safety or serviceability), which is defined as follows:

$$f_1 = \Pr\left[\mathrm{Fs}_1 > 1.0\right] \tag{5.4a}$$

$$f_2 = \Pr\left[\mathrm{Fs}_2 > 1.0\right] \tag{5.4b}$$

where f_1 and f_2 are the feasibilities with respect to the structure safety and serviceability of the shield tunnel, respectively; and Pr[Fs > 1.0] represents the conditional probability

that the factor of safety (Fs) is greater than 1.0 in face of the unforeseen longitudinal variation of noise factors.

Compared to the actual design in Shanghai, the bolt diameter of the circumferential joints (D_c) of the knee point, obtained with the robust design optimization, is reduced from 30 mm to 20 mm. As a result, the design feasibility with respect to the structure safety (f_1), tunnel performance with respect to the structure safety (the mean of μ_{Fs1}), cost efficiency (C), and the design robustness with respect to both structure safety (R_1) and serviceability (R_2) are significantly improved. For example, the feasibility with respect to the structure safety is increased from 0.7846 to 0.9607 and the design robustness with respect to the serviceability is increased from 2.31 to 4.89. However, the design feasibility and tunnel performance with respect to the serviceability (i.e., f_2 and the mean of μ_{Fs2}) are degraded somewhat, although the tunnel performance requirements are still satisfied.

It should be noted that the most preferred design (i.e., knee point) may vary with the robust design optimization setting (e.g., design space and target factors of safety). Here, the robust design optimization of the example shield tunnel is reanalyzed and redesigned with different target factors of safety with respect to the tunnel performance, and the results are listed in Table 5.5. The results show that different robust design optimization settings can produce different final designs of the shield tunnel. As the target factors of safety (with respect to the tunnel performance) increase, the design feasibility (i.e., f_1 and f_2), tunnel performance (i.e., the mean of μ_{Fs1} and the mean of μ_{Fs2}), and cost (C) of the most preferred designs tend to increase.

Table 5.4: Comparison between the knee point in robust design and the real-world design

Designs	Easy-to-control design parameters (***d***)				Design feasibility		Tunnel performance		Design objectives		
	t (m)	ρ (%)	D_c (mm)	D_l (mm)	f_1	f_2	Mean of μ_{Fs1}	Mean of μ_{Fs2}	C (1000 USD)	R_1	R_2
Knee point	0.35	0.5	20	30	0.9607	0.9033	1.90	1.80	309.57	9.59	4.89
Real-world design	0.35	0.5	30	30	0.7846	0.9695	1.39	2.50	316.67	8.78	2.31

Table 5.5: Robust design optimization results of the example tunnel with different target factors of safety

Target factors of safety	Easy-to-control design parameters (***d***)				Design feasibility		Tunnel performance		Design objectives		
	t (m)	ρ (%)	D_c (mm)	D_l (mm)	f_1	f_2	Mean of μ_{Fs2}	Mean of μ_{Fs2}	C (1000 USD)	R_1	R_2
1.5	0.35	0.50	20	30	0.9607	0.9033	1.90	1.80	309.57	9.59	4.89
2	0.40	0.50	20	30	0.9931	0.9643	2.12	2.10	353.18	11.09	4.61
2.5	0.40	1.00	25	35	0.9999	0.9963	3.39	2.53	474.85	10.76	4.59
3	0.45	1.00	25	35	1.0000	0.9997	3.94	3.04	534.22	11.74	4.34

Summary

This chapter presents an improved design methodology for shield tunnels with robust design concept, which is indeed a combination of the robust design methodology and an advanced framework for shield tunnel performance analysis. In the context of the proposed design methodology, the input parameters that are associated with the longitudinal variation are classified as noise factors, while the input parameters that can be adjusted by the designer are classified as design parameters. The objective of the improved design methodology is to identify an optimal design in the design space, represented by a set of design parameters, such that the design robustness (against the longitudinal variation of noise factors) is maximized; naturally, the desire to maximize

the design robustness must be balanced with the desire to optimize the cost and to satisfy the conventional performance requirements of shield tunnels.

CHAPTER SIX

CONCLUSIONS AND RECOMMENDATIONS

Conclusions

The following conclusions are drawn from the results presented in Chapter II:

(1) A Winker elastic foundation theory-based FEM procedure is developed in this chapter to analyze the tunnel longitudinal behavior in light of the longitudinal variation of tunnel design parameters, the effectiveness and capability of which is verified by both analytical solutions and model tests.

(2) Within the context of the developed FEM procedure, the random field concept can be employed to model spatial variation (in the longitudinal domain) of design parameters. A random field concept is easily coupled with the proposed FEM procedure for tunnel longitudinal performance analysis considering spatial variability of tunnel design parameters. The coupling between the proposed FEM solution with random field modeling of the longitudinal variation of soil properties is demonstrated through an illustrative example

(3) Based on the results of the parametric study, the mean of tunnel settlement is found to be suitable to gauge the overall tunnel settlement while the coefficient of variation (COV) of tunnel settlement is suitable to gauge the extent of tunnel differential settlement. The results also show the overall tunnel settlement is mainly affected by the mean of soil properties, while the

extent of tunnel differential settlement is mainly affected by the COV and the scale of fluctuation of soil properties.

The following conclusions are drawn from the results presented in Chapter III:

(1) Compared to existing tunnel analysis methods, the proposed tunnel analytical model can effectively consider the tunnel longitudinal differential settlement in the analysis of the circumferential behavior of tunnel segment lining, primarily through the consideration of the shearing effect and the flattening effect.

(2) The proposed tunnel analytical model is meaningful in analyzing the variation of the circumferential behavior of the segment lining along the longitudinal direction. As demonstrated in the example, for a given tunnel with a collected tunnel longitudinal settlement curve, the longitudinal variation of the circumferential behavior is readily obtained.

(3) Parametric studies reveal the circumferential behavior of the segment lining, including both the structure safety and the serviceability, always degrades with the curvature and fourth derivative of the tunnel settlement; the increase in the flexural stiffness of the longitudinal joints might degrade the circumferential behavior of the segmental lining. Though the increase in the flexural stiffness of the circumferential joints can degrade the structural safety, it can enhance the serviceability of the segmental lining. While the increase in the segment thickness always enhances the serviceability, there might be no such enhancement to the structure safety.

The following conclusions are drawn from the results presented in in Chapter IV:

(1) The proposed fuzzy set-based robust geotechnical design (RGD) methodology is demonstrated to be effective and capable of producing a final design of the shield tunnel (segment ring) that is robust against the variation in noise factors (i.e., uncertain geotechnical parameters and surcharge load).

(2) The Pareto front obtained through multi-objective optimization reveals the trade-off relationships between robustness and cost. All the points on the Pareto front are non-dominated optimal designs. The most preferred design can be directly selected based on the desired level of cost or robustness.

(3) The proposed procedure (Eq. 4.6) to interpret the results of fuzzy set-based uncertainty propagation analysis is shown to achieve comparable results with those obtained with Monte Carlo simulations (MCSs) with various distribution assumptions. The fuzzy set-based approach is computationally advantageous over the MCS approach, especially within a robust design framework; as such, the new fuzzy set-based RGD methodology is computationally more attractive than the reliability-based RGD methodology.

(4) Parametric analyses show that the segment thickness and diameter of joint bolt are the key parameters that control the safety and robustness with respect to SLS in the design of a shield tunnel, while the safety and robustness with respect to ULS are mainly dominated by the segment steel reinforcement ratio. Although an increase in any of the three design parameters (i.e., segment thickness, reinforcement ratio, and diameter of joint bolt) can lead to an

increase in cost, the effect of the reinforcement ratio on the cost is the most profound.

The following conclusions are drawn from the results presented in in Chapter V:

(1) The advanced framework for shield tunnel performance analysis is shown to be capable of analyzing the longitudinal variation of input parameters (e.g., soil parameters). The new solution framework yields results (in terms of probabilities of unsatisfactory performance of the shield tunnel) that are more consistent with data from the structure health monitoring in Shanghai metro, compared to the conventional method that is not equipped to consider the longitudinal variation of input parameters.

(2) The modified robust design methodology for shield tunnels is demonstrated to be capable of producing a final design of the shield tunnel that is robust against longitudinal variation of noise factors and is simultaneously cost efficient, in addition to meeting the conventional tunnel performance requirement (i.e., structure safety and serviceability). Compared to the actual design, the most preferred design (i.e., knee point) obtained with the robust design optimization yielded higher design robustness, higher cost efficiency and higher feasibility of tunnel performance.

(3) Unlike current design practices, the proposed robust design methodology considers design robustness, cost efficiency, and tunnel performance requirements explicitly and simultaneously. Utilizing multi-objective optimization, the proposed robust design methodology yields a Pareto front

that shows a trade-off relationship between design robustness and cost efficiency. The Pareto front with or without the identified knee point can aid in selecting the most preferred design.

(4) Apart from multi-objective optimization, a new design robustness measure, which is based upon the signal-to-noise ratio, is proposed for the shield tunnel performance analysis. The new robustness measure is adapted specifically for considering the longitudinal variation of input parameters and is demonstrated effective for use with the proposed robust design of shield tunnels.

(5) Parametric analyses show that the segment thickness, bolt diameter of the circumferential joints, and bolt diameter of the longitudinal joints are key design parameters that affect tunnel performance and design robustness with respect to both structure safety and serviceability. While tunnel performance and design robustness with respect to the structure safety are significantly affected by the steel reinforcement ratio of tunnel segment, the tunnel performance and design robustness with respect to the serviceability are barely affected by the steel reinforcement ratio of tunnel segment.

Recommendations

To further expand the work presented in this dissertation, a number of research topics may be undertaken, which include the following:

(1) Further investigation of a more complex solution model for shield tunnel performance analysis is suggested, such that the joints of shield tunnels and

the soil-structure interaction between the ground and the tunnel structure can be more accurately included. It should be noted that the proposed solution model for shield tunnel performance has not been validated with field data, further examination that is based upon field data is recommended for future work.

(2) The design robustness in this dissertation study is measured with the signal-to-noise ratio of shield tunnel performance. Other measures such as feasibility-based robustness, gradient-based robustness and variation-based robustness may be investigated for their suitability for use in the developed geotechnical robust design framework.

(3) MCS is a built-in element of the developed solution model for shield tunnel performance analysis, as the random field concept is used to simulate the longitudinal variation of input parameters. Further development of a simpler solution model for shield tunnel performance analysis, in which the computational demanding MCS might not be required, is of interest.

(4) A further development of the robust design framework of shield tunnels into a robust maintenance framework for shield tunnels is of importance. The integration of life-cycle performance assessment within the robust maintenance optimization framework may also be explored.

REFERENCES

American Transportation Research Board (ATRB). (2000). Design and Construction of Transportation Facilities.

Baker, R. (1984). "Modeling soil variability as a random field." Journal of the International Association for Mathematical Geology, 16(5), 435-448.

Beard, A.N. (2010). "Tunnel safety, risk assessment and decision-making." Tunnelling and Underground Space Technology, 25(1), 91-94.

Bobet, A. (2001). "Analytical solutions for shallow tunnels in saturated ground." Journal of Engineering Mechanics, 127(12), 1258-1266.

Branke, J., Deb, K., Dierolf, H., and Osswald, M. (2004). "Finding knees in multiobjective optimization." In Parallel problem solving from nature - PPSN VIII. pp. 722-731.

Braslavsky, J.H., Middleton, R.H., and Freudenberg, J.S. (2007). "Feedback stabilization over signal-to-noise ratio constrained channels." Automatic Control, IEEE Transactions on, 52(8), 1391-1403.

British Tunneling Society (BTS). (2004). Tunnel Lining Design Guide, Thomas Telford.

Cavalaro, S.H.P., Blom, C.B.M., Walraven J.C., and Aguado, A. (2011). "Structural analysis of contact deficiencies in segmented lining." Tunnelling and Underground Space Technology, 26, 734-749.

Cho, S.E. (2007). "Effects of spatial variability of soil properties on slope stability." Engineering Geology, 92(3), 97-109.

Daloglu, A.T., and Vallabhan, C.G. (2000). "Values of k for Slab on Winkler Foundation." Journal of Geotechnical and Geoenvironmental Engineering, 126(5), 463-471.

Deb, K., Pratap, A., Agarwal, S., and Meyarivan, T. (2002). "A fast and elitist multi-objective genetic algorithm: NSGA-II." IEEE Transactions on Evolutionary Computation, 6(2), 182-197.

Dhatt, G., Lefrançois, E., and Touzot, G. (2012). Finite Element Method. John Wiley & Sons.

Dong, W.M., and Wong, F.S. (1987). "Fuzzy weighted averages and implementation of the extension principle." Fuzzy Sets and Systems, 21(2), 183-199.

Duncan, J.M. (2000). “Factors of safety and reliability in geotechnical engineering.” Journal of Geotechnical and Geoenvironmental Engineering, 126(4), 307-316.

El-Ramly, H., Morgenstern, N.R., and Cruden, D.M. (2002). “Probabilistic slope stability analysis for practice.” Canadian Geotechnical Journal, 39(3), 665-683.

Fenton, G.A. (1999). “Estimation for stochastic soil models.” Journal of Geotechnical and Geoenvironmental Engineering 1999, 125(6), 470-485.

Fenton, G.A., and Griffiths, D.V. (2002). “Probabilistic foundation settlement on spatially random soil.” Journal of Geotechnical and Geoenvironmental Engineering, 128(5), 381-390.

Fenton, G.A., and Griffiths, D.V. (2003). “Bearing-capacity prediction of spatially random c φ soils.” Canadian Geotechnical Journal, 40(1), 54-65.

Fenton, G.A., and Griffiths, D.V. (2005). “Three-dimensional probabilistic foundation settlement.” Journal of Geotechnical and Geoenvironmental Engineering, 131(2), 232-239.

Giasi, C.I., Masi, P., and Cherubini, C. (2003). “Probabilistic and fuzzy reliability analysis of a sample slope near Aliano.” Engineering Geology, 67(3), 391-402.

Gong, W., Luo, Z., Juang, C.H., Huang, H., Zhang, J., and Wang, L. (2014a). “Optimization of site exploration program for improved prediction of tunneling-induced ground settlement in clays.” Computers and Geotechnics, 56, 69-79.

Gong, W., Wang, L., Juang, C.H., Zhang, J., and Huang, H. (2014b). “Robust geotechnical design of shield-driven tunnels.” Computers and Geotechnics, 56, 191-201.

Gong, W., Khoshnevisan, S., and Juang, C.H. (2014c). “Gradient-Based Design Robustness Measure for Robust Geotechnical Design.” Canadian Geotechnical Journal (online).

Gong, W., Juang, C.H., Huang, H., Zhang, J., and Luo, Z. (2014d). “Effect of the longitudinal differential settlement on the circumferential behavior of shield tunnels.” Tunnelling and Underground Space Technology (accepted).

Gonzalez, C., Sagaseta, C. (2001). “Paterns of soil deformations around tunnels. Application to the extension of Madrid Metro.” Computers and Geotechnics, 28, 445-468.

Hiroshi, M., and Takeshi, S. (1987). “Analysis of beams on non-homogeneous elastic foundation.” Computers and Structures, 25(6), 941-946.

Horvath, J.S. (1983). "Modulus of subgrade reaction: new perspective." Journal of Geotechnical Engineering, 109(12), 1591-1596.

Huang, H., Gong, W., Khoshnevisan, S., Juang, C.H, Zhang, D., and Wang, L. (2014). "Simplified procedure for finite element analysis of the longitudinal performance of shield tunnels considering spatial soil variability in longitudinal direction." Computers and Geotechnics (under review).

Huang, X. (2012). Study on influence of deep excavation on underlying existing shield tunnel in soft ground [Dissertation]. Tongji University, Shanghai (in Chinese).

Huang, X., Huang, H.W., and Zhang, J. (2012). "Flattening of jointed shield-driven tunnel induced by longitudinal differential settlements." Tunnelling and Underground Space Technology. 31, 20-32.

International Tunnelling Association (ITA). (2000). "Guidelines for the design of shield tunnel lining." Tunnelling and Underground Space Technology, 15(3), 303-331.

Japan Society of Civil Engineers (JSCE). (2007). "The Design and Construction of Underground Structures." Japan Society of Civil Engineers, Tokyo, Japan.

Juang, C.H., Lee, D.H., and Sheu, C. (1992). "Mapping slope failure potential using fuzzy sets." Journal of Geotechnical Engineering, 118(3), 475-494.

Juang, C.H., Jhi, Y.Y., and Lee, D.H. (1998). "Stability analysis of existing slopes considering uncertainty." Engineering Geology, 49(2), 111-122.

Juang, C.H., and Wang, L. (2013). "Reliability-based robust geotechnical design of spread foundations using multi-objective genetic algorithm." Computers and Geotechnics, 48, 96-106.

Juang, C.H., Wang, L., Liu, Z., Ravichandran, N., Huang, H., and Zhang, J. (2013). "Robust geotechnical design of drilled shafts in sand: New design perspective." Journal of Geotechnical and Geoenvironmental Engineering, 139(12), 2007-2019.

Juang, C. H., Wang, L., Hsieh, H. S., and Atamturktur, S. (2014). "Robust geotechnical design of braced excavations in clays." Structural Safety, 49, 37-44.

Kerr, A.D. (1965). "A study of a new foundation model." Acta Mechanica, 1(2), 135-147.

Klar, A., Vorster, T.E., Soga, K., and Mair, R.J. (2007). "Elastoplastic solution for soil-pipe-tunnel interaction." Journal of Geotechnical and Geoenvironmental Engineering, 133(7), 782-792.

Koyama, Y. (2003). "Present status and technology of shield tunneling method in Japan." Tunneling and Underground Space Technology, 18(2-3), 145-159.

Lee, K.M., and Ge, X.W. (2001). "The equivalence of a jointed shield-driven tunnel lining to a continuous ring structure." Canadian Geotechnical Journal, 38(3), 461-483.

Lee, K.M., Hou, X.Y., Ge, X.W., and Tang, Y. (2001). "Analytical solution for jointed shield-driven tunnel lining." International Journal for Numerical and Analytical Methods in Geomechanics, 25(4), 365-390.

Li, H.Z., and Low, B.K. (2010). "Reliability analysis of circular tunnel under hydrostatic stress field." Computers and Geotechnics, 37(1), 50-58.

Li, K.S., and Lumb, P. (1987). "Probabilistic design of slopes." Canadian Geotechnical Journal, 24(4), 520-535.

Liao, S.M. (2002). Research on the mechanism of longitudinal shear transfer of circular tunnel [Dissertation]. Tongji University, Shanghai (in Chinese).

Liao, S.M., Hou, X.Y., and Peng, F.L. (2005). "Longitudinal shear transfer of tunnel and its 1D analytical solution." Chinese Journal of Rock Mechanics and Engineering, 24(7), 1110-1116 (in Chinese).

Liao, S.M., Peng, F.L., and Shen, S.L. (2008). "Analysis of shearing effect on tunnel induced by load transfer along longitudinal direction." Tunnelling and Underground Space Technology, 23(4), 421-430.

Lin, P.S., Yang, L.W., and Juang, C.H. (1998). "Subgrade reaction and load-settlement characteristics of gravelly cobble deposits by plate-load tests." Canadian Geotechnical Journal, 35(5), 801-810.

Loganathan, N., and Poulos, H.G. (1998). "Analytical prediction for tunneling-induced ground movements in clays." Journal of Geotechnical and Geoenvironmental Engineering, 124(9), 846-856.

Lu, H., Li, S., Simkins Jr, D.C., Kam Liu, W., Cao, J. (2004). "Reproducing kernel element method Part III: Generalized enrichment and applications." Computer Methods in Applied Mechanics and Engineering, 193(12), 989-1011.

Lü, Q., and Low, B.K. (2011). "Probabilistic analysis of underground rock excavations using response surface method and SORM." Computers and Geotechnics, 38(8), 1008-1021.

Luo, Z., Atamturktur, S., Juang, C.H., Huang, H., and Lin, P.S. (2011). "Probability of serviceability failure in a braced excavation in a spatially random field: Fuzzy finite element approach" Computers and Geotechnics, 38(8), 1031-1040.

Luo, Z., Atamturktur, S., Cai, Y., and Juang, C.H. (2012). "Reliability analysis of basal-heave in a braced excavation in a 2-D random field." Computers and Geotechnics, 39, 27-37.

Mair, R.J. (2008). "Tunnelling and geotechnics: New horizons." Géotechnique, 58(9), 695-736.

Ministry of Construction of the People's Republic of China (MCPRC). (2001). Unified Standard for Reliability Design of Building Structures (GB50068-2001). China Building Industry Press, Beijing (in Chinese).

Ministry of Construction of the People's Republic of China (MCPRC). (2003). Code for Design of Metro (GB50157-2003). China Building Industry Press, Beijing (in Chinese).

Ministry of Transport of the People's Republic of China (MTPRC). (2004). Code for Design of Road Tunnel. China Communication Press, Beijing (in Chinese).

Mollon, G., Dias, D., and Soubra, A.H. (2009). "Probabilistic analysis of circular tunnels in homogeneous soil using response surface methodology." Journal of Geotechnical and Geoenvironmental Engineering, 135(9), 1314-1325.

Park, K.H. (2005). "Analytical solution for tunneling-induced ground movement in clays." Tunnelling and Underground Space Technology, 20(3), 249-261.

Park, H.J., Um, J.G., Woo, I., and Kim, J.W. (2012). "Application of fuzzy set theory to evaluate the probability of failure in rock slopes." Engineering Geology, 125, 92-101.

Pasternak, P.L. (1954). On a new method of analysis of an elastic foundation by means of two-constants [Dissertation]. Moscow, USSR: Gosudarstvennoe Izdatelstvo Literaturi po Stroitelstvu I Arkhitecture; 1954 [in Russian].

Phadke, M.S. (1989). Quality Engineering Using Robust Design. Prentice Hall. Englewood Cliffs, NJ.

Phoon, K.K., and Kulhawy, F.H. (1999). "Characterization of geotechnical variability." Canadian Geotechnical Journal, 36(4), 612-624.

Sadrekarimi, J., and Akbarzad, M. (2009). "Comparative study of methods of determination of coefficient of subgrade reaction." Electronic Journal of Geotechnical Engineering, 14, 1-14.

Schmidl, T.M., and Cox, D.C. (1997). "Robust frequency and timing synchronization for OFDM." Communications, IEEE Transactions on, 45(12), 1613-1621.

Shangahi Municipal Construction Commite. (1999). Foundation Design Code (DGJ08-11-1999). Shanghai (in Chinese).

Shiwa, Y., Kkawa Shima, K., Shang. (1986). "Evaluation procedure for seismic stress developed in shield tunnel seismic deformation method." Journal of Structure Mechanics and Earthquake Engineering, 28(5), 45-50 [in Japanese].

Shrestha, B., and Duckstein, L. (1998). "A fuzzy reliability measure for engineering applications." Uncertainty Modeling and Analysis in Civil Engineering, 121-135.

Sonmez, H., Gokceoglu, C., and Ulusay, R. (2003). "An application of fuzzy sets to the geological strength index (GSI) system used in rock engineering." Engineering Applications of Artificial Intelligence, 16(3), 251-269.

Špačková, O., Šejnoha, J., and Straub, D. (2013). "Probabilistic assessment of tunnel construction performance based on data." Tunnelling and Underground Space Technology, 37, 62-78.

Talmon, A.M., and Bezuijen, A. (2013). "Calculation of longitudinal bending moment and shear force for Shanghai Yangtze River Tunnel: Application of lessons from Dutch research." Tunnelling and Underground Space Technology, 35, 161-171.

Teachavorasinskun, S., and Chub-Uppakarn, T. (2010). "Influence of segmental joints on tunnel lining." Tunnelling and Underground Space Technology, 25, 490-494.

Terzaghi, K, (1955). "Evaluation of coefficients of subgrade reaction." Geotechnique, 5(4), 297-326.

Toraño, J., Rodríguez, R., Diego, I., and Rivas, J.M. (2006). "Estimation of Settlements due to shallow tunnels and their effects." Tunnelling and Underground Space Technology, 21, 288-294.

Verruijt, A., and Booker, J.R. (1996). "Surface settlements due to deformation of a tunnel in an elastic half plane." Geotechnique, 46(4), 753-756.

Wang, L., Hwang, J. H., Juang, C. H., and Atamturktur, S. (2013). "Reliability-based design of rock slopes – A new perspective on design robustness." Engineering Geology, 154, 56-63.

Winkler, E. (1867). Die lehre von der elastizitat und fesigkeit [Dissertation]. Prague.

Wood, A.M.M. (1975). "The circular tunnel in elastic ground." Géotechnique, 25(1), 115-127.

Wu, S.H., Ou, C.Y., Ching, J., and Juang, C.H. (2012). "Reliability-based design for basal heave stability of deep excavations in spatially varying soils." Journal of Geotechnical and Geoenvironmental Engineering, 138(5), 594-603.

Wu, Y., and Wu, A. (2000). Taguchi Methods for Robust Design. ASME press, New York.

Yankelevsky, D.Z., Adin, M.A., and Eisenberger, M. (1988). "Beams on nonlinear winkler foundation with gaps." Computers and Geotechnics, 6(1), 1-11.

Zadeh, L.A. (1965). "Fuzzy sets." Information and Control, 8(3), 338-353.

Zhang, Z., and Huang, M. (2014). "Geotechnical influence on existing subway tunnels induced by multiline tunneling in Shanghai soft soil." Computers and Geotechnics, 56, 121-132.